Self-Gravitating Warped Disks Around Supermassive Black Holes in Galactic Nuclei

Ayşe ULUBAY SIDDIKİ

München 2009

Self-Gravitating Warped Disks
Around Supermassive Black Holes
in Galactic Nuclei

Ayşe ULUBAY SIDDIKİ

Dissertation

an der Fakultät für Physik

der Ludwig–Maximilians–Universität

München

vorgelegt von

Ayşe ULUBAY SIDDIKİ

aus İstanbul, Türkei

München, den 10 Juni 2009

Contents

ABSTRACT

Many galaxies, including our own, harbor supermassive black holes with masses of order $10^6 - 10^9 M_\odot$ in their centers. Some of these galaxies fall into the category of active galaxies with high outputs of energy from their centers, while some galactic nuclei appear quiet. It is believed today that the activity in a galactic nucleus results from infalling gas onto the black hole via a sub-parsec scale accretion disk. Under certain circumstances accretion disks feeding the central black holes might deviate from planar geometry and become warped. This modification to the shape of the disk has consequences on how the accretion process takes place and might also effect other phenomena related to nuclear activity in galaxies. Quiet galaxies also harbor warped disks in their centers albeit at somewhat larger distances to the black hole, and might be populated by stars as observed from the center of our Galaxy. Therefore the study of warped nuclear disks not only gives information on the accretion process but also poses constraints on the physical conditions that lead to the formation of stars in the close vicinity of black holes, which is a highly debated topic in astrophysics.

In this thesis we investigated self-gravitating warped disks around supermassive black holes. We showed that there exist equilibrium solutions for such disks where the disk precesses as a single unit. We derived a scaling relation relating the normalized precession frequency of the disk to the disk-to-black hole mass fraction. This relation makes the warp model applicable to various systems where the disk's self-gravity is non-negligible. We analyzed the stability of the obtained equilibrium solutions and found that highly inclined, steadily precessing stable disk configurations are possible.

In a related but separate study, we applied our self-gravitating warped disk model to the clockwise rotating warped stellar disk at the Galactic Center. We argued that a past accretion disk at the Galactic Center might have been warped due to radiation pressure or due to the spin of the central black hole, and that star formation might have taken place after disk warping. We simulated the time evolution of the warped stellar disk for various parameters, and showed

that disks for which the disk-to-black hole mass ratio exceeds 0.001 break into two separately precessing pieces, while the ones with less mass precess without breaking up. We also made a comparison of our models with the observations, and saw that a non-breaking light disk model agrees well with the observations of the clockwise stellar disk.

Zusammenfassung

Viele Galaxien, einschließlich unserer eigenen, beherbergen supermassereiche Schwarze Löcher mit Massen $10^6 - 10^9 M_\odot$ in ihren Zentren. Manche dieser Galaxien bezeichnet man als aktive Galaxien, weil sie viel Energie aus ihrem Zentrum ausstossen, andere Kerne bleiben inaktiv. Man ist heute der Ansicht, dass einströmende Materie, über die Bildung einer Akkretionsscheibe auf sub-pc Skalen, für die Aktivität verantwortlich ist. Unter bestimmten Bedingungen können sich die Akkretionsscheiben, die die Schwarzen Löcher füttern, krümmen (engl. warp). Diese Änderung in der Geometrie der Akkretionsscheibe hat Folgen für den Akkretionsprozess und möglicherweise auch Auswirkungen auf andere Phänomene, die mit der nuklearen Aktivität von Galaxien in Zusammenhang stehen. Inaktive Galaxien beherbergen auch gekrümmte Scheiben in ihren Zentren, obgleich in etwas größeren Abständen vom schwarzen Loch, die auf ähnliche Weise von Sternen bevölkert werden, wie im Zentrum der Milchstraße. Deshalb liefert das Studium von gekrümmten Scheiben nicht nur Informationen über die Akkretionprozesse, sondern es erlaubt auch die physikalischen Bedingungen einzugrenzen unter denen sich Sterne in der Nähe von Schwarzen Löchern bilden – ein gegenwärtig stark diskutiertes Thema in der Astrophysik.

In dieser Arbeit haben wir selbst-gravitierende gekrümmte Scheiben um supermassereiche Schwarze Löcher studiert. Wir haben gezeigt, dass es Gleichgewichtslösungen für solche Scheiben gibt, bei denen die Scheibe als Ganzes präzediert. Wir haben eine Skalenrelation zwischen der normierten Präzessionsfrequenz der Scheibe und dem Massenanteil der Scheibe am schwarzen Loch abgeleitet. Diese Relation erlaubt es, das Warp-Modell auf verschiedene Systeme anzuwenden, in denen die Eigengravitation der Scheibe nicht vernachlässigt werden kann. Ferner haben wir die Stabilität der Gleichgewichtslösungen analysiert und festgestellt, dass stark geneigte, stetig präzedierende, stabile Scheibenkonfigurationen möglich sind.

In einer ähnlichen, aber separaten Studie, haben wir unser Modell von selbst-gravitierenden, gekrümmten Scheiben auf die im Uhrzeigersinn rotierende stellare Scheibe im galaktischen

Zentrum angewendet. Wir haben dargelegt, dass Strahlungsdruck oder der Drehimpuls des zentralen schwarzen Lochs eine frühere Akkretionscheibe im galaktischen Zentrum hätte krümmen können und dass sich Sterne nach diesem Prozess bilden konnten. Simulationen zur zeitlichen Entwicklung von gekrümmten stellaren Scheiben für verschiedene Parameter haben gezeigt, dass Scheiben, die mehr als 0.1% der Masse des Schwarzen Lochs besitzen, in zwei separat präzedierende Teile aufbrechen, während Scheiben mit weniger Masse als Einheit präzedieren, ohne aufzubrechen. Wir haben unser Modell mit Beobachtungen verglichen und gesehen, dass eine massearme Scheibe, die nicht aufbricht, gut mit den Beobachtungen der im Uhrzeigersinn rotierenden stellaren Scheibe übereinstimmt.

ÖZET

Kendi gökadamız da dahil olmak üzere pek çok gökadanın merkezinde $10^6 - 10^9 M_\odot$ kütleli karadelikler bulunmaktadır. Bu gökadalardan bir kısmı merkezlerinden salınan yüksek enerji nedeniyle aktif gökadalar grubuna girerken bazıları ise bu şekilde bir aktivite göstermemektedir. Bugünkü bilgilerimiz gökada merkezlerindeki aktivitenin, parsek altı ölçekli kütle aktarım disklerinden karadeliğin üzerine düşen gazdan kaynaklığını göstermektedir. Bahsi geçen kütle aktarım diskleri bazı koşullar altında düzlemsel geometriden saparak eğrilik kazanabilmektedir. Diskin yapısında oluşan bu değişiklik maddenin karadelik üzerine nasıl aktarılacağını etkilerken, galaksi merkezindeki nükleer aktivite ile ilişkilendirilebilecek diğer süreçleri de etkilemesi beklenmektedir. Aktif olmayan gökada merkezlerinde de benzer eğrilikli disklerin varlığı gözlemlerle tespit edilmiştir. Bu diskler merkezi karadeliklere kütle aktarım disklerine göre göreceli olarak daha uzakta bulunup, kendi gökadamızın merkezinde olduğu gibi üzerlerinde yıldızlar grupları bulundurabilmektedirler. Bu nedenlerle, eğrilikli diskler hakkında yapılan çalışmalar sadece süper kütleli karadeliklerin ne şekilde beslendiği hakkında bilgi vermekle kalmayıp, karadeliklerin çok yakın komşuluğunda yıldız oluşumu gibi ilginç astrofizik problemlerin çözümünde de rol oynamaktadır.

Bu tez çalışmasında süper kütleli karadelikler etrafındaki öz çekimsel eğrilikli diskleri inceledik. Bu disklerin tek bir frekansta presesyon hareketi yapacağı denge durumlarının bulunduğunu gösterdik. Böyle bir denge durumu için, bir referans frekansa normalize edilmiş presesyon frekansının disk kütlesinin karadeliğe kütlesine oranına bağlılığını gösteren bir ölçekleme ilişkisi çıkardık. Bu ölçekleme ilişkisi Keplersel olmayan kuvvetin öz çekimden kaynaklandığı çoğu sisteme uygulanabilmektedir. Bulunan denge durumlarının kararlığını da inceleyerek, çok yüksek eğrilik derecelerine sahip kararlı disklerin var olabileceğini gösterdik.

Ana hatlarıyla yukarıda bahsedilen çalışmaya benzeyen diğer bir çalışmamızda eğrilikli disk modelini gökada merkezinde gözlenen eğrilikli yıldız diskine uyguladık. Sözü geçen

diskin gökada merkezinde eskiden bulunan ve ışınım basıncı ya da karadeliğin dönmesi sayesinde eğrilik kazanmış bir kütle aktarım diskiden evrimleşmiş olabileceğini iddia ettik. Bugün gözlenen yıldızların, disk eğriliğini kazandıktan sonra olutşuğunu savunarak, diskin zaman evrimini inceledik. Pek çok disk parametresi için tekrar ettiğimiz sayısal benzetimlerde kütlesi karadeliğin kütlesinin 0.001 katından fazla olan disklerin ikiye bölündüğünü, kütlesi bu değerden az olan disklerin ise bölünmeden evrimlerine devam ettiklerini gördük. Modellerimizi gözlemlerle karsılaştırarak, gözlemleri en iyi açıklayan modellerin düşük kütleli, ve bölünme göstermeyen disklere ait oldugunu saptadık.

CHAPTER 1

INTRODUCTION

1.1 Nuclei of Galaxies

The central few ten parsecs of a galaxy is usually termed as its nucleus. It is believed today that most galactic nuclei, including our own, host supermassive black holes (SMBHs) with masses of order $10^6 M_\odot$ to $10^9 M_\odot$ (Kormendy & Richstone, 1995; Magorrian et al., 1998; Genzel et al., 2000; Ghez et al., 2005; Gillessen et al., 2009).

From the point of view of energetics, galactic nuclei may be grouped in two main classes; the active galactic nuclei (AGN) with typical energy energy outputs of $> 10^8\ L_\odot$, and the quiescent nuclei possessing small luminosities. In the current understanding, activity in galactic nuclei is attributed to the accretion of material onto the supermassive black hole at the center. 'What the is actual mechanism responsible for feeding the black holes?'; 'is there a duty cycle between the AGN and quiescent modes of galactic nuclei?'; 'how do the active galaxies effect their small and large scale environments?' are debated questions in modern astrophysical research, and merit detailed investigation. In the following sections, we will briefly summarize the current status of research focused on galactic nuclei.

In order to be able to judge the importance of various processes taking place close to the central black hole, one has to consider the length and timescales at which these processes occur. Using the conventions $M_8 = M_{bh}/10^8 M_\odot$, $r_1 = r/1$ pc, $\sigma_{100} = \sigma_\star/100$ km/s, $N_6 = N_\star/10^6$, and $t_8 = \tau_p/10^8$ yr, for the mass of the central black hole, distance from it, velocity dispersion, the number of surrounding stars, and physical time, these scales can be summarized as follows (Alexander, 2006; Merritt, 2006):

The size of the event horizon (Schwarzschild radius) for a non-rotating black hole is

defined as:

$$r_s = \frac{2GM_{bh}}{c^2} = 3 \times 10^{13} M_8 \text{ cm,} \qquad (1.1)$$

where G is the gravitational constant, M_{bh} is the mass of the black hole and c is the speed of light. This is the smallest length scale for a given M_{bh}, since the escape velocity would have to be greater than c for a smaller radius.

When a gravitationally bound object (call it a star) approaches the black hole, the competition between its self-gravity and the pull of the black hole determines an other important scale related to the massive object; the tidal radius. For a star with a radius of $r_\star$, and mass $m_\star$ the tidal radius is given by:

$$r_t = r_\star \left(\frac{M_{bh}}{m_\star}\right)^{1/3} \cong 3.25 \times 10^{13} M_8 \left(\frac{M_\odot}{R_\odot}\right)^{-1/3} \text{ cm.} \qquad (1.2)$$

A star approaching to a black hole closer than this radius is torn apart.

Within a sphere of influence of radius r_{inf}, the dynamics of the region is dominated by the black hole. The radius of influence is defined as:

$$r_{\text{inf}} = \frac{GM_{bh}}{\sigma_\star^2} \cong 1.33 \times 10^{20} \; M_8 \sigma_{100}^{-2} \text{ cm,} \qquad (1.3)$$

where $\sigma_\star$ is the 1D velocity dispersion of the stars far from the black hole. This definition is not always unique since $\sigma_\star$ depends on the radius for most density distributions. One of the alternative definitions of r_{inf} is:

$$M_\star(r \leq r_{\text{inf}}) = 2M_{bh} \qquad (1.4)$$

$M_\star$ being the total mass in stars inside r_{inf}.

For a star orbiting the black hole, the dynamical time scale (circular orbital period), is defined as:

$$T_{\text{orb}} = 2\pi \sqrt{\frac{r^3}{GM_{bh}}} \cong 9390 \; M_8^{-1/2} r_1^{3/2} \text{ yr.} \qquad (1.5)$$

While the object orbits the black hole, there might be encounters between it and the other orbiting stars. The time scale on which such encounters cause evolution towards a Maxwellian velocity distribution is called the relaxation time scale. For a homogeneous

system of $N_\star$ stars it is given by (Binney & Tremaine, 1987):

$$T_{\mathrm{relax}} = \frac{N_\star}{8 \ln N_\star} T_{\mathrm{orb}} = 8.45 \times 10^7 N_6 r_1^{3/2} M_8^{-1/2} \text{ yr} \tag{1.6}$$

in terms of the dynamical time.

When the relaxation time by encounters with other stars is shorter than the age of the system, the orbits of the stars can be significantly altered during their lifetimes. It is often assumed that the encounters are uncorrelated, i.e. a star does not have a memory of its past encounter. If the potential in which the orbit evolves is not purely that of the central point mass, the orbit of a star experiences precession. The time scale of this precession, τ_{p}, is typically much longer than the orbital time scale, so the orbits remain almost unchanged for times $t < \tau_{\mathrm{p}}$. In this case it is more plausible to consider the gravitational interactions between a system of massive wires, to represent the time averaged stellar orbits, rather than individual stars. Since the radial and the azimuthal frequencies in a Keplerian potential are in resonance, the assumption of uncorrelated encounters become invalid since the wires feel eachother's torques during the long precession time. Although for a large number of stars the sum of the torques will sum to zero, due to statistical fluctuations there will be an excess torque in an unknown direction resulting in exchange of momentum. This process, termed resonant relaxation, results in a re-distribution of the orbits around the black hole (Rauch & Tremaine, 1996; Gürkan & Hopman, 2007). The time scale for resonant relaxation is given by (Hopman & Alexander, 2006):

$$T_{\mathrm{RR}} \simeq \frac{A_{\mathrm{RR}}}{N_\star} \left(\frac{M_{bh}}{m_\star} \right)^2 \frac{T_{\mathrm{orb}}^2}{\tau_p} = 8.82 \times 10^9 N_6^{-1} t_8 r_1 \text{ yr} \tag{1.7}$$

where A_{RR} is a numerical constant of order unity.

Tables (1.1) and (1.2) compare these scales for the nuclear environments of the Galactic Center, and the well studied Seyferts NGC4258, NGC1068, and Circinus.

1.1.1 The Center of the Galaxy

The center of the Milky Way Galaxy is the closest galactic nucleus to us at a distance of about 8 kpc (Genzel et al., 2000; Eisenhauer et al., 2003, 2005). Given this proximity, observations of the Galactic Center (GC) are rich in details, and they provide information on the processes that might be common to many galactic nuclei. The dust in the disk of the Galaxy, where the Sun is also located, prevents observation of the GC at optical wavelengths. Most studies

Object	$M_{bh}(10^7\ M_\odot)$	$r_{\rm s}$(AU)	$r_{\rm t}$(AU)	$r_{\rm inf}$(pc)	$\sigma_\star$(km/s)
Galactic Center	0.4	0.08	0.7	1.1	125
NGC4258	3.9	0.8	1.6	6	167
NGC1068	1.0	0.2	1	1.4	177
Circinus	0.17	0.03	0.6	0.3	167

Table 1.1: Comparison of the relevant length scales for the well documented objects: Galactic Center, and the Seyfert objects NGC4258, NGC1068, and Circinus. The mass of the Galactic Center black hole, SgrA*, is adopted from Trippe et al. (2008). Rest of the masses, and the assumed stellar velocity dispersions are from from Table (1) of Milosavljević & Loeb (2004).

Object	r (pc)	$T_{\rm orb}$(yr)	$T_{\rm relax}(10^7\rm yr)$	$T_{\rm RR}(10^7\rm yr)$
Galactic Center	0.06	690	0.62	0.22
NGC4258	0.16	962	0.9	40
NGC1068	0.6	1.3×10^4	12.5	538
Circinus	0.11	2627	2.4	0.6

Table 1.2: Comparison of the relevant time scales for the objects listed in Table (1.1). The listed distances are the inner edges of the maser disks (see section 1.3) for the Seyfert nuclei, and the inner edge of the clockwise rotating stellar disk (see section 1.1.1) for the Galactic Center. The orbital times are calculated at these radii. For the calculation of the relaxation and resonant relaxation time scales, $N_\star = 10^6$ is assumed. For the latter, coefficient $A_{\rm RR} = 1$, and $\tau_p = 10^8$yr is adopted.

therefore are conducted at either lower (X-and γ), or higher (mm-and IR) wavelengths.

At the very center, a supermassive black hole resides with a mass of $\sim 4 \times 10^6\ M_\odot$, and its location coincides with the radio source SgrA* (Balick & Brown, 1974; Eckart & Genzel, 1996; Genzel et al., 2000; Trippe et al., 2008). SgrA* is surrounded by a cluster of old stars, as well as a system of young stars some of which are arranged in a disk (Krabbe et al., 1995; Levin & Beloborodov, 2003; Genzel et al., 2003; Lu et al., 2006; Paumard et al., 2006; Schödel et al., 2007; Bartko et al., 2009; Lu et al., 2009), and by ionized and molecular gas (Guesten et al., 1987; Jackson et al., 1993; Morris, 1993). The following subsections summarize the current status of the GC research in terms of these constituents.

Stellar Content

A unique opportunity provided by the Galactic Center is that its stars can individually be observed. This section summarizes the current knowledge on the stellar content of the Galaxy's nuclear environment.

At distances smaller than 1" to SgrA* the so-called S-stars are found (1" ~ 0.04 pc at the distance of GC). Their orbits are consistent with being isotropic, and the probability distribution of their orbital eccentricities obeys $n(e) \sim e^{2.6}$ (Gillessen et al., 2009). Since the high angular resolution observations of the GC region started, one of the members of this cluster, S2, has completed one orbit around SgrA*, in approximately 15 years. Its orbit fits well to being Keplerian and yields an enclosed mass of $4 \times 10^6 M_\odot$ (Schödel et al., 2002; Gillessen et al., 2009). Like the other members of the cluster, it is a B-type star (Martins et al., 2008). B stars are massive, short lived stars, which suggests that there must have been an episode of star formation near SgrA* a few million years ago. In order for a molecular cloud near a SMBH to fragment into stars, its self-gravity should overcome the tidal field of the black hole. This requirement for star formation poses a constraint on the minimum cloud densities, of order $n_{\rm crit} \sim 10^{10} {\rm cm}^{-3}$ (Morris, 1993), if the S-stars are to be believed as fragments of such a collapse. However, the situation is such that not only the inner parsec of the Galaxy is devoid of molecular gas (Jackson et al., 1993), but also the molecular densities reached even at a few parsecs distance from SgrA* are of order $3 \times 10^{3-5} {\rm cm}^{-3}$ (Guesten et al., 1987). This is the so-called paradox of youth for GC S-stars (Ghez et al., 2003; Gillessen et al., 2009).

The other group of stars, which also suffers from the youth paradox, are observed at distances of $\sim 0.04-0.5$ pc from SgrA*. Their spectra are dominated by He-I emission lines, and they are consistent with being Wolf-Rayet stars (Genzel et al., 2003; Bartko et al., 2009). Unlike the S-stars, the orbits of the He-I stars are not randomly oriented (Bartko et al., 2009). Of the nearly 90 observed stars, 40 populate a disk which is observed to rotate clockwise (CW) on the plane of sky (Levin & Beloborodov, 2003; Genzel et al., 2003; Paumard et al., 2006; Lu et al., 2006; Bartko et al., 2009). Of the rest, 19 stars seem to populate a second disk highly inclined to the CW disk (Genzel et al., 2003; Paumard et al., 2006; Bartko et al., 2009). This second disk is seen to rotate counter clockwise (CCW) on the sky (but also see Lu et al. (2006, 2009)). Although the youth issue is less severe for the He-I stars, star formation is still prohibited at such distances. There have been several attempts to explain the existence of young stars in the GC. The two main scenarios tackling the problem are:

Infalling Cluster Scenario: Gerhard (2001) considered a cluster of stars, which form at

a distance of a few 10 parsecs from SgrA*. Due to dynamical friction between the newly formed cluster, and the background (nuclear) stars, the cluster sinks inwards to the position of the observed young stars while loosing its low mass members by tidal stripping until finally it dissolves. There have been many numerical follow-ups of this scenario. The aim of the simulations was to define the plausible parameter range for which the cluster reaches the central parsec in a few million years without dissolving due to the tidal field of the black hole. Paumard et al. (2006) argue that the infall time for the cluster exceeds the lifetime of the observed stars if the cluster is initially not extraordinarily dense. Cluster cores with the required high stellar densities can be maintained in the presence of an intermediate mass black hole (IMBH) at the cluster center (Hansen & Milosavljević, 2003). Simulations performed by Gürkan & Rasio (2005) suggest that IMBHs might result from collisions of stars during their infall to the center. Recently, Fujii et al. (2007) reported that when the stars stripped from the cluster are included in the tidal friction description, the inspiral timescale decreases.

One outcome of the infalling cluster scenario is that, when the cluster is on its way to the central parsec, it should leave trails of stars at any distance. However the published data contain no stars beyond 0.5 pc (Paumard et al., 2006; Bartko et al., 2009; Lu et al., 2009).

In-situ Formation in an Accretion Disk: In this picture, a molecular cloud is captured by SgA* and forms a gravitationally unstable accretion disk (Levin & Beloborodov, 2003; Milosavljević & Loeb, 2004; Nayakshin & Cuadra, 2005; Nayakshin et al., 2007). Stars form at the location where they are observed today. Although typical molecular cloud densities in the vicinity of SMBHs are not sufficient to overcome the tidal field of the hole, theoretical estimates suggest that the fragmentation conditions are met naturally on the accretion disks which become self-gravitating beyond a few tenth of parsec (Kolykhalov & Syunyaev, 1980; Gammie, 2001; Goodman, 2003).

Several numerical simulations have been performed aiming at modeling the fragmentation of a nuclear/accretion disk for parameters relevant to the Galactic Center. These simulations were run either by $a\ priori$ assuming a gravitationally unstable accretion disk already in place (Nayakshin et al., 2006; Alexander et al., 2008), or by trying to account also for the formation of the disk itself (Bonnell & Rice, 2008). Mapelli et al. (2008) simulated the infall of a turbulent cloud from a distance of a few 10 parsecs. They found that at around $t \sim 5 - 6 \times 10^5$ yr most of the cloud material is depleted, and forms stars. The disk extends radially between 0.06 to 0.5 parsecs which is close to the observed range, but they do not see a second disk forming. In order to circumvent this last point, Wardle & Yusef-Zadeh (2008) built up a scenario where they considered the passage of a giant molecular cloud

(GMC) past SgrA*. Since a typical-size GMC would engulf the GC while passing it there might be cancellation of angular momentum due to interaction of opposite sides of the cloud, and the authors argue qualitatively that this might be a way of forming two inclined stellar disks. Making use of a similar idea, Hobbs & Nayakshin (2009) simulated the collision of two GMCs with sizes of one to a few parsecs at the outer edge of the central parsec. Their simulations can produce the formation of two inclined star forming disks/rings, however the authors note that their results depend largely only the initial conditions regarding the location where the collision takes place, and the cooling prescription for star formation.

Today it looks like for suitably chosen parameters a star forming disk at the GC can be simulated. On the other hand, apart from the problem of youth, an other issue still to be addressed is their orbital distribution. It is reasonable to expect that a planar accretion disk leaves behind a planar distribution of stars when it fragments. While the clockwise rotating 40 stars seem to lie on a well defined disk, the counter clockwise rotating 19 stars have orbits which are highly inclined to the former (Paumard et al., 2006; Bartko et al., 2009). Moreover there is an evidence of a warp in the CW disk with an amplitude of about $60°$ (Bartko et al., 2009). A recent publication by Lu et al. (2009) points out that even though the stars might have formed in-situ, their current orbital distribution suggests a more sophisticated origin than a simple thin accretion disk. Simulations performed by Cuadra et al. (2008) are in line with this idea showing that once the stars form on a thin, i.e. cold, accretion disk it is not possible to perturb these stars to high inclinations.

An other stellar population at the GC is the dynamically relaxed, evolved, old stars with ages of several Gyr. Their orbits are isotropically distributed, and their spectra are dominated by CO absorption lines (Trippe et al., 2008). Theoretical models of galactic nuclei predict existence of density cups around SMBHs. Depending on the assumptions, such as the stellar mass diversity of the nuclear cluster, or the age of the stellar cluster in comparison to the relaxation time scale, models predict the cusps to be power-laws with indices between $-3/2$, and $-5/2$ (Schödel et al., 2007). In this respect, observations of the GC old stellar population provide an interesting test of the cusp theories. Observations by Genzel et al. (2003) indicate the existence of a cusp with an exponent of 1.3-1.4 between 0".15-0."2.

Gaseous Content

We have seen in the previous subsection that the presence of the young stars in the close vicinity of SgA* is a debated issue. In order to better understand the star formation process, it is useful to have a knowledge on the gaseous content of the region. We will summarize the

results regarding such observations and models in this subsection.

The observations carried out by Lo & Claussen (1983) revealed a structure of ionized gas in the inner 1.5 of the GC. The ionized gas is broken into several arms, which in projection look like a spiral, hence the name minispiral. The brightest of these arms are the Northern Arm, The Eastern Arm, and The Western Arc, and they lie in different planes which might have arisen due to tidal stretching of the gas streamers while falling into the center (Vollmer & Duschl, 2000).

The minispiral is surrounded by a disk-like structure of neutral and molecular gas called the circumnuclear disk (CND). It was discovered by Becklin et al. (1982) in the FIR continuum of dust. These authors found that the dust density decreases in the central 3 pc, and that the minimum of dust emission is located at the position of SgrA*. The emission peaks have a double-lobed structure at a radius of 1.7 pc from the center, which is the inner edge of the CND. Genzel et al. (1985) observed the GC in FIR C^+ and O^0 fine structure lines and confirmed the existence of a neutral gas ring of 10 pc diameter with a mass of several 10^4 $M_\odot$. The CND is inclined by $\sim 69°$ to the line-of-sight(LOS) and $\sim 20°$ to the plane of the Galaxy. Between the inner and outer edges, the CND consists of several clumps which have sizes $0.1 - 0.5$ pc (Genzel et al., 1985; Gatley et al., 1986). This clumpy nature lets the UV radiation from the central star cluster penetrate into the disk and heat the clumps. The CND rotates around the center with a velocity of ~ 100km/s corresponding to an enclosed mass of $\sim 4.6 \times 10^6$ $M_\odot$ at the inner edge of the disk, and its plane is warped (Jackson et al., 1993). The CND has also been observed through line transitions of NH_3 (Coil & Ho, 1999, 2000; McGary et al., 2001). The aim of these observations was to investigate the possible relations between the CND and the GMCs near the Galactic Center. At a projected distance of 10 pc from SgrA*, the 20 km/s cloud (M-0.13.008) appears to be feeding the CND through the 'southern streamer'. The other GMC, the 50 km/s cloud (M-0.02-0.07), seems to be related to the 20 km/s cloud where these clouds are connected by a molecular ridge.

On the basis of sticky particle calculations, Sanders (1998) modeled the CND as disruption of a gas cloud on a low angular momentum orbit. Moving in the potential of a central mass of $M_{bh} = 2.5 \times 10^6$ $M_\odot$ plus a spherically symmetric stellar distribution the cloud falls into the Galactic Center. The infall of the cloud could have been due to a collision of two oppositely moving clouds. After two or three orbital times, ($\approx 5 \times 10^5$ yr at a distance of 3.5 pc from the center), the cloud settles into an asymmetric disk with a central cavity. One interesting aspect of the simulation is that the highly elongated and intersecting orbits form strong shocks at the intersection points with velocities high enough to overcome the Roche

limit for star formation, and provide a possible mechanism for the formation of young stars at the Galactic Center. Following this work, Vollmer & Duschl (2001a,b, 2002) constructed analytic models to explain the dynamics of the CND. In their models, gas of several $10^4 \, M_\odot$ falls into the Galactic Center from distances smaller than 10 pc. An important parameter in their models is the UV radiation field from the central stellar cluster which determines the radius of the infalling clouds. At a critical distance from the center, the clouds with high enough densities to overcome the tidal effects either collapse, or fragment into clumps. This critical radius is found to be ~ 2 pc, which is the value for the inner edge of the CND proposed by several observations. Taking also into account the effects of rotation and magnetic field stabilizes the clouds against gravity. Contrary to the previous works, they found that the CND disk is a longer lived structure with a lifetime of 10^7 yr. Coker et al. (2003) performed 3D hydrodynamical simulations in order to explain the formation of the CND from multiple self-gravitating infalling clouds. They took into account the potential of a central point mass of $2.6 \times 10^6 \, M_\odot$ plus an extended stellar distribution. As the clouds on different trajectories fall into the center, they collide and form the clumpy structure. Small mass clouds are disrupted before reaching the inner edge of the disk, where larger mass clouds loose their outer parts by tidal stripping. The result emerging from their simulations is that, a single cloud is not sufficient to maintain the current structure of the CND, but collisions of multiple clouds is necessary, and in order for the CND to be a stable structure, it has to be continuously fed by the GMCs nearby.

1.1.2 Nearby Galactic Nuclei

Thanks to the recent advances in astronomical instrumentation it is now possible to observe the nuclei of nearby galaxies at high resolution. The nuclear regions of galaxies host various structures each of which contribute to the total potential of the nucleus. Nuclear star clusters, stellar, gas and dust rings, are the most prominent features at relatively large scales of about a few hundred down to a few ten parsecs (Carollo et al., 1998; Schinnerer et al., 2006; Böker et al., 2008; Hicks et al., 2009). At smaller scales, in the very vicinity of the SMBHs, our knowledge is mostly restricted to that obtained from theoretical models and simulations, apart for a handful of objects. Most of the effort in observing galactic nuclei is directed towards determining the masses of the central black holes which are thought to reside in most, if not all, galactic nuclei, and linking the nuclear phenomena to the large scale evolution of galaxies. In this subsection we will summarize the current status of research of nearby nuclei

in the light of the recent observational results.

From the point of view of stellar kinematics, the most well received result that emerged in the last decade is the discovery of an empirical correlation between the mass of the central black hole and the stellar velocity dispersion of the host bulge: the so-called $M_{bh} - \sigma_\star$ relation (Ferrarese & Merritt, 2000; Gebhardt et al., 2000; Tremaine et al., 2002). Ferrarese & Ford (2005) give:

$$\frac{M_{bh}}{10^8 M_\odot} = (1.66 \pm 0.24) \left(\frac{\sigma_\star}{200\mathrm{km/s}}\right)^{4.68 \pm 0.43}. \tag{1.8}$$

This relation is of importance not only in the studies of galactic nuclei, but also in studies addressing the galaxy evolution as a whole since its slope, normalization, scatter and evolution constrains models considering mergers of galaxies which are thought to lead to the formation of the SMBHs themselves.

The motion of gas in galactic nuclei can also be used to determine black hole masses, as well as to study phenomena related to nuclear activity in galaxies. Probably the most robust determination of black hole masses is provided by the observations of maser sources in the pc/sub-pc vicinity of the black holes. Most of the observed masers trace the orbital motion of the underlying accretions disks, hence are useful probes of the nuclear dynamics (in the nucleus of Circinus, some of the observed spots trace an outflow (Greenhill et al., 2003)). Moreover, the conditions required for maser activity, i.e. temperature, density etc., give constraints on the physical conditions in the masing parts of the accretion disks.

Maser emission from galactic nuclei is preferentially detected when the disk is observed edge-on. The spots lying in the LOS to the observer appear at the systemic velocity, v_{sys}, of the galaxy in the spectrum while the spots along the diameter perpendicular to the LOS are observed at $v_{\mathrm{sys}} \pm \sqrt{GM_{bh}/r}$ for receding, (-) sign, and approaching, (+) sign, parts of the disk (Kondratko, 2007).

NGC4258 is the first galaxy with a maser detection from its center (Claussen et al., 1984). The VLBI imaging of the maser spots provided the first firm evidence of an underlying disk structure (Miyoshi et al., 1995). The disk extends radially between 0.13-0.26 pc, and exhibits a warp in its shape (Herrnstein et al., 1996). Figure (1.1) shows the locations of the observed masers superimposed on a warped disk, together with their fitted rotation curve (from Herrnstein et al. (1999)). The Keplerian rotation curve traced by the masers implies a central black hole mass of $3.9 \times 10^7 M_\odot$. Moreover, after assuming a suitable disk model, the proper motions and the LOS accelerations of the maser spots provide a very precise measurement of
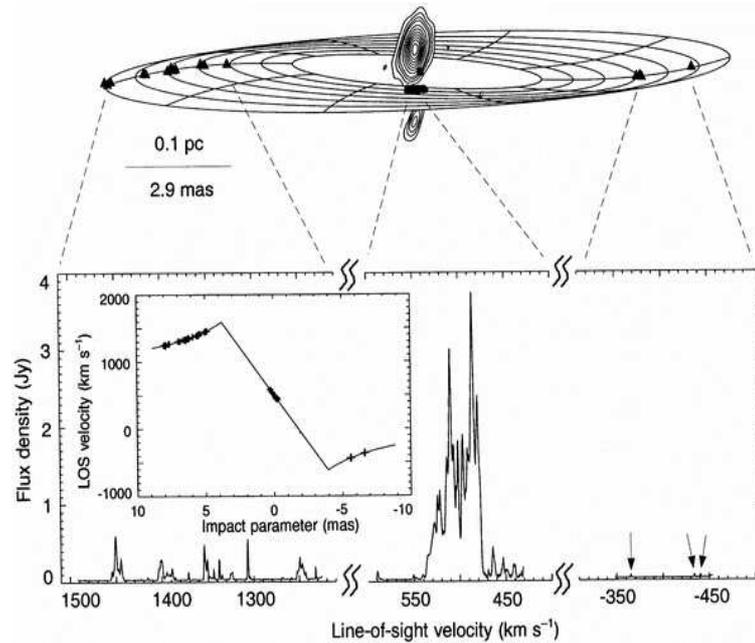
Figure 1.1: Warped nuclear disk of NGC 4258. The upper panel shows the best fit to the observed maser spots shown by the triangles. The lower panel is the VLBA total power spectrum. The inset shows the maser data superposed on a Keplerian rotation profile. Taken from Herrnstein et al. (1999).

the distance to the galaxy, $D = 7.2 \pm 0.3$ Mpc.

Another well monitored nearby nucleus with a maser detection from the center is that of the Circinus galaxy. Gardner & Whiteoak (1982) identified H_2O masers from the center of Circinus. Later, Greenhill et al. (2003) showed that the maser spots trace a warped nuclear disk between $0.11 - 0.4$ pc. Between $\sim 0.11 - 1$ pc a number of more spots are identified which trace a wide-angle outflow from the center. The support for the existence of a warped disk comes from: 1) the S-shape formed by the maser spots, 2) the highest red and blue-shifted emission bracketing the systemic velocity, 3) the antisymmetric distribution of the red and the blue shifted features along the S-shape with a velocity declining as $\sim b^{-0.5}$ where b is the position along the major axis of the distribution (the impact parameter), and 4) the orientation of the inner disk being roughly perpendicular to the axis of the observed radio lobes. When the innermost red and blue-shifted spots are assumed to share a common orbit (with observed velocity, and radius), the mass contained within the innermost radius can be calculated to be $1.7 \pm \times 10^6 M_\odot$. The rotation curve delineated by the masers is very close to Keplerian. If one assumes that the steepening of the rotation curve due to disk warping (both in position and inclination angles) is compensated by the effect of the disk mass, an upper

limit can be set for the disk mass as $M_d < 4 \times 10^5 M_\odot$.

Maser emission is detected also from the center of NGC1068, another nearby nucleus. The masers in this object trace a disk with an inner edge at 0.65 pc and an outer edge at 1.11 pc (Greenhill & Gwinn, 1997). The enclosed mass within 0.65 pc is $\sim 1.7 \times 10^7 M_\odot$ (Greenhill & Gwinn, 1997).

The examples of maser nuclei we have listed so far share the common property that their disks are warped. The discussion of the cause of the warps in nuclear disks is deferred to section (1.3.1) where we will summarize the warping mechanisms for nuclear disks in general. Before moving on to the next section, we should note that today, more than 70 galaxies are known with maser emission detected from their centers, and for 27 of these, there is good evidence for a disk origin (Water Maser Cosmology Project; WMCP (2009)). Future observations will give us more detailed information on the geometry of their disks.

1.1.3 Active Galactic Nuclei

The innermost central regions of some galaxies output large amounts of energy, typically $L > 10^8 L_\odot$. These objects are classified as active galactic nuclei (AGN). The cause of activity is believed to be the accretion of material onto the black hole at the center. In this section we list some main properties of AGN.

Properties common to most AGN are: high luminosities, variability on time-scales of days to years, and ability to produce highly collimated jets (Tadhunter, 2007).

Local AGN are divided into two main classes depending on their optical spectra. Seyfert 1 type spectra are dominated by broad (≥ 5000 km/s) and narrow (~ 1000 km/s) emission lines. Seyfert 2's on the other hand produce only narrow lines.

At high redshifts, quasars are the more luminous counterparts of Seyferts. Radio loudness is also a criteria in defining AGN types. The class of radio objects includes radio loud quasars, Blazars, and Faranoff Riley objects of type 1 and 2.

The maser nucleus NGC1068 briefly mentioned in the previous section has particular importance in AGN studies. Although it is classified as a Seyfert 2 nucleus, Antonucci & Miller (1985) observed a broad component in the polarized emission from its nucleus. They suggested that Seyfert 2 nuclei contain hidden broad line regions (BLRs) obscured by a dense dusty torus surrounding the black hole. This idea was the basis of unification of AGN classes. The unification theories try to group AGN depending on their appearance to the observer. In the very center, the SMBH is fed by the accretion disk. The accretion disk is surrounded by

some toroidal material of dust and gas (torus). When the observer's LOS passes through the toroidal structure, BLRs can not be observed, hence the nucleus appears as that of a Seyfert 2 galaxy. AGN viewed directly from above avoiding the obscuring media appear as Seyfert 1 nuclei. Figure (1.2) depicts schematically the AGN classes when viewed from different lines of sight.
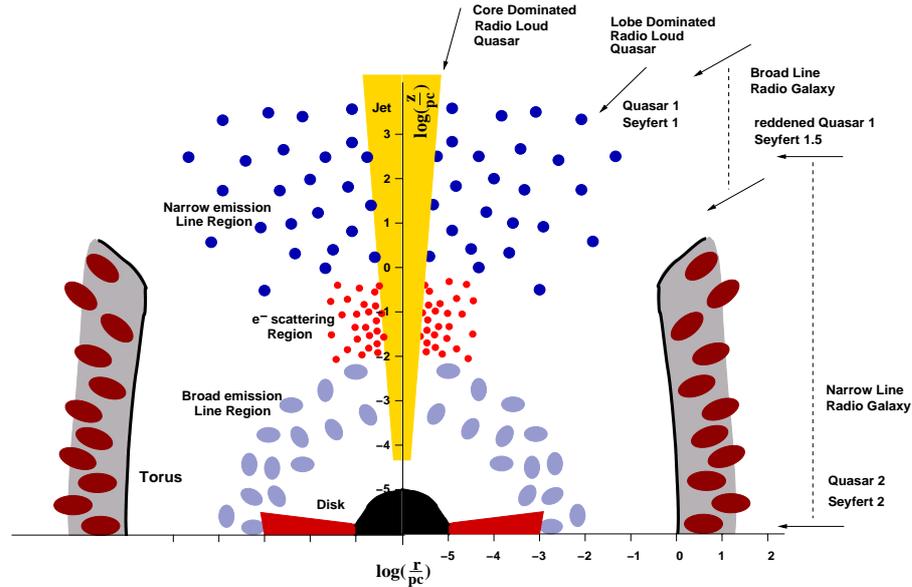

Figure 1.2: Classification of AGN according to viewing direction (schematic). Taken from Zier & Biermann (2002).

1.2 Accretion Disks

In the previous sections, we have briefly discussed the studies on nearby galactic nuclei based on their observations. In this section we describe the basics of theory of accretion onto compact central objects (black holes hereafter) based on the enlightening reviews by Pringle (1981); Papaloizou & Lin (1995); Lodato (2008), and on the dedicated book by Frank et al. (2002).

First consider a spherically symmetric steady flow towards the center. Equilibrium for a flow element consisting of electrons and protons is defined such that, the outward directed radiative force resulting from the Thomson scattering of electrons is balanced by the inward directed gravitational force acting on the electron- proton plasma. Neglecting the relatively small mass of the electrons in comparison to the protons one can write (Frank et al., 2002):

$$\frac{GM_{bh}m_p}{r^2} = \frac{\sigma_T L}{4\pi r^2 c}. \tag{1.9}$$

Here, m_p is the proton mass, and σ_T is the Thomson cross section. This relation sets the Eddington luminosity limit L_{edd} for the flow, which has the value:

$$\begin{aligned} L_{edd} &= 4\pi GM_{bh}m_p c/\sigma_T \\ &\cong 1.3 \times 10^{38}(M_{bh}/M_\odot) \text{ erg s}^{-1}. \end{aligned} \tag{1.10}$$

The Eddington luminosity can be converted into a mass accretion rate, $\dot{M}_{Edd}$, via:

$$L_{Edd} = \epsilon \dot{M}_{Edd}c^2, \tag{1.11}$$

where ϵ is the radiative efficiency.

Now consider the flow confined to an axisymmetric disk in differential rotation around the black hole. In this case neighboring fluid elements generate a viscous stress when they pass each other [see figure (1.3)].
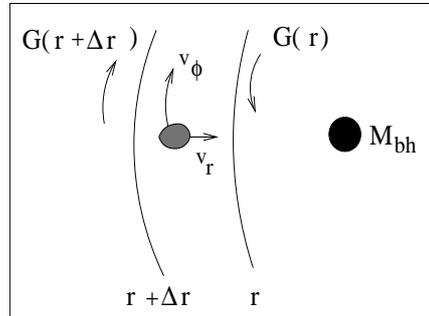

Figure 1.3: Schematic representation of the motion of a fluid element in an accretion disk under viscous torques.

The viscous torque exerted by the outer ring of gas on the adjacent inner ring of gas is given by:

$$G(r) = 2\pi\nu\Sigma r^3 \frac{d\Omega(r)}{dr}. \tag{1.12}$$

Here, Σ is the surface density of the disk at location r, ν is the viscosity coefficient, and $\Omega(r)$ is the angular velocity. The motion of a fluid element on its orbit around the black hole under the effects of viscous torques can be described by two velocity components: the orbital

motion, which can often be taken as Keplerian, has the velocity:

$$v_\phi = r\Omega(r), \tag{1.13}$$

with $\Omega(r) = \sqrt{GM_{bh}/r^3}$. The second component of the velocity of the disk element can be predicted from equation (1.12) which implies that for a rotation law where the angular velocity decreases with increasing radius, the inner parts of the disk lose angular momentum leading to spiraling of disk material towards the black hole with velocity v_r, while being fed by the outer parts. The temporal evolution of the disk arising from this flow is studied by considering the local conservation equations for mass (i.e. continuity equation), and angular momentum. The former is written as:

$$\frac{\partial \Sigma}{\partial t} + \frac{1}{r}\frac{\partial}{\partial r}(r\Sigma v_r) = 0. \tag{1.14}$$

The equation for the angular momentum conservation follows from considering the net viscous torque on the disk element, and is given by:

$$\frac{\partial}{\partial t}(\Sigma r^2 \Omega) + \frac{1}{r}\frac{\partial}{\partial r}(\Sigma v_r r^3 \Omega) = \frac{1}{2\pi r}\frac{\partial G}{\partial r}. \tag{1.15}$$

The drift velocity v_r can be obtained from the above equations, and for Keplerian rotation it is given by:

$$v_r = -\frac{3}{\Sigma\sqrt{r}}\frac{\partial}{\partial r}(\nu\Sigma\sqrt{r}). \tag{1.16}$$

From equation (1.16) we see that it is crucial to know the magnitude of viscosity ν to study the accretion process. However, although the consequences of viscous evolution of accretion disks have been studied widely (Lynden-Bell & Pringle, 1974; Papaloizou & Pringle, 1983; Pringle, 1992; Shafee et al., 2008) its origin remains debated. In recent years, the magneto-rotational instability (MRI) has been suggested as the cause of turbulence (Balbus & Hawley, 1991). Consider the two neighboring elements, A and B with $r_A > r_B$. When the disk is weakly magnetized, there is a magnetic tension between these elements. In a differentially rotating disk, where $\Omega_A < \Omega_B$, the motion of element A is accelerated by element B, while element B is retarded by A. In time, the separation between A and B increases, hence the tension between them. This process goes until the disk exhibits the MR instability [1].

---

[1]As an alternative to MRI, gravitational instabilities in self-gravitating disks as the driving mechanism of mass flow is starting to gain favor due to numerical convergence problems faced by many MRI simulations. See Lodato & Rice (2004, 2005) and references therein.

In studying accretion disks one usually makes use of the standard α-prescription introduced by Shakura & Syunyaev (1973). The viscosity is written as:

$$\nu = \alpha c_s H, \tag{1.17}$$

where c_s is the local sound speed, and H is the disk scale length. In this representation, all the unknowns of the accretion process, i.e. by which mechanism it is driven, is collected in the parameter α. Adopting parameters relevant to galactic nuclei, Frank et al. (2002) give an estimate of the viscosity as:

$$\nu = 1.8 \times 10^{18} \alpha^{4/5} \left(\frac{\dot{M}}{10^{26}} \right)^{3/10} \left(\frac{M_{bh}}{10^8} \right)^{-1/4} \left(\frac{r}{10^{14}} \right)^{3/4} f^{6/5} \ \mathrm{cm^2 s^{-1}}, \tag{1.18}$$

where $f = 1 - (6GM_{bh}/rc^2)^{1/2}$. The time scale by which the disk material is transported onto the black hole, the viscous time scale, is given by $t_{\mathrm{vis}} \sim 2r^2/\nu$. Assuming a constant surface density profile, and constant viscosity through the disk, and using equations (1.16), and (1.18) the drift velocity of accreting material, and the viscous time can be estimated to be $v_r = -562$ cm/s, and $v_{\mathrm{vis}} = 5 \times 10^7$ yr respectively at a distance of $r = 0.1$ pc, for typical parameters of $M_{\mathrm{bh}} = 10^8 M_\odot$, $\dot{M} = 10^{26} \mathrm{gcm^{-2}}$, and $\alpha = 0.1$.

1.3   Warps in Astrophysics

In the previous sections, we presented a brief overview of galactic nuclei. Both in discussing the Galactic Center (1.1.1), and the nearby nuclei (1.1.2), we encountered examples of nuclear disks with non-planar geometries. In the remaining parts of this introduction, we will summarize the studies of warps in astrophysics to give a more complete outlook to the main theme of this thesis.

Warped disks where the inclination of the disk with respect to a preferred plane changes with radius have been known to astronomers since decades. The early studies of warps were dedicated to explain the observed bending of the outer parts of galaxies. Observations showed that although the warps manifest themselves mostly in the HI layers of galaxies, warped stellar disks are also not rare (van der Kruit, 1979; Innanen et al., 1982; Reshetnikov et al., 2002). At a first glance, this suggests gravity as the cause of the warp, since it influences both the gaseous and the stellar components in a galaxy.

Hunter & Toomre (1969) studied the case of a self-gravitating, isolated, thin disk, where

the warp was represented by linear bending waves. They showed that such a disk does not permit any long-lasting modes when realistically smooth-edged density profiles are considered. Interaction of the galaxy with a nearby object as a cause of the warp was considered by many authors until observations showed that many warped galaxies lacked companions, or the companions were not massive enough. Later, as the evidence for dark matter halos around galaxies became stronger, modelers developed scenarios in which the disk assumes the shape of a normal mode in the potential of a flattened dark halo (Sparke, 1984; Kuijken, 1991). However, subsequent work showed that these modes are damped quickly when the internal dynamical response of the halo is taken into account (Nelson & Tremaine, 1995; Binney et al., 1998). Today, it seems most plausible that galactic warps result from interactions and from accretion of material with misaligned angular momentum (Jiang & Binney, 1999).

Increasing spatial resolution of observations has provided evidence that warps are not only common in galactic disks, but appear also in other astrophysical contexts at much smaller scales. One of the best studied examples of such a warped disk is surrounding the neutron star Her X-1. Besides an orbital period of 1.7 days, and a pulsation period of 1.24 seconds, it shows on-and-off states with a periodicity of 35 days (Tananbaum et al., 1972; Giacconi et al., 1973; Gerend & Boynton, 1976). This long periodicity in the X-ray light curve of Her X-1 is best explained by the existence of a warp occulting the central star as the disk precesses (Wijers & Pringle, 1999).

Yet an other class of objects where warps are pronounced are the nuclear disks surrounding the SMBHs of galactic nuclei. Examples of such disks have been presented in sections (1.1.1), and (1.1.2) in the discussions of the GC, and nearby nuclei. We summarize the theoretical models of warped nuclear disks in the following section.

1.3.1 Warped Nuclear/Accretion Disks

Nuclear disks in galaxies are subject to various torques in the environments they are embedded in. Under certain circumstances, an initially planar disk might become unstable against warping due to these torques.

The theoretical studies of nuclear warped disks focus on their viscous evolution in order to connect to the process of accretion. In this case, the equations governing the flat accretion disks have to be modified. For planar disks, considering a cylindrical symmetry, viscosity as parameterized by ν arises due to the $r - \phi$ stress between the disk elements. In a warped

disk, there is also a component of stress in the $r - z$ direction which tries to damp the warp. Papaloizou & Pringle (1983) proposed an α-like description for such disks. They found that in the small tilt regime, the radial (ν_1), and vertical (ν_2) coefficients of viscosity obey:

$$\frac{\nu_2}{\nu_1} = \frac{1}{2\alpha^2}. \tag{1.19}$$

Ogilvie (1999) considered the nonlinear corrections to the above approach. He showed that for small amplitude warps:

$$\frac{\nu_2}{\nu_1} = \frac{1}{2\alpha^2}\frac{4(1 + 7\alpha^2)}{4 + \alpha}, \tag{1.20}$$

and he also gave higher order correction terms for high amplitude warps. For highly inclined warps, the ratio of the two viscosities become close to unity (Caproni et al., 2006a).

Pringle (1992) devised a set of equations describing the viscous evolution of warped accretion disks. In a warped geometry, the drift velocity is given by:

$$v_r = \frac{(\partial/\partial r)(\nu_1\Sigma r^3(d\Omega/dr)) - \frac{1}{2}\nu_2\Sigma r^3\Omega|\partial \mathbf{l}/\partial r|^2}{r\Sigma(\partial/\partial r)(r^2\Omega)}. \tag{1.21}$$

Here $\mathbf{l}$ is the unit vector at location r in the disk. When inserted into the mass conservation equation, and assuming Keplerian rotation one arrives at:

$$\frac{\partial\Sigma}{\partial t} = \frac{3}{r}\frac{\partial}{\partial r}\left[r^{1/2}\frac{\partial}{\partial r}(\nu_1\Sigma r^{1/2})\right] + \frac{1}{r}\frac{\partial}{\partial r}\left[\nu_2\Sigma r^2\left|\frac{\partial \mathbf{l}}{\partial r}\right|^2\right]. \tag{1.22}$$

This equation describes the viscous evolution of the surface density of a warped disk. Similarly, the evolution of angular momentum, $\mathbf{L}$, of the disk elements under viscous torques can be written as:

$$\begin{aligned}
\frac{\partial\mathbf{L}}{\partial t} &= \frac{3}{r}\frac{\partial}{\partial r}\left[\frac{r^{1/2}}{\Sigma}\frac{\partial}{\partial r}(\nu_1\Sigma r^{1/2})\mathbf{L}\right] + \frac{1}{r}\frac{\partial}{\partial r}\left[\left(\nu_2 r^{1/2}\left|\frac{\partial \mathbf{l}}{\partial r}\right|^2 - \frac{3}{2}\nu_1\right)\mathbf{L}\right] \\
&+ \frac{1}{r}\frac{\partial}{\partial r}\left(\frac{1}{2}\frac{\partial}{\partial r}\nu_2 r|\mathbf{L}|\frac{\partial \mathbf{l}}{\partial r}\right). \tag{1.23}
\end{aligned}$$

In equations (1.22), and (1.23), the terms involving the coefficient ν_1 arise due to the radial drift of the disk material towards the black hole. On the other hand, the terms involving

the coefficient ν_2 are related to the motion of the disk elements in the vertical direction. In the case of flat disks where $\partial \mathbf{l}/\partial r = 0$, the only non-vanishing terms in equations (1.22), and (1.23) are the terms involving ν_1, and the equations reduce to the equations described in section (1.2). We see that the surface density evolution of a warped disk depends on the amplitude of the warp only to second order, i.e. for small amplitude warps for which $|\partial \mathbf{l}/\partial \mathbf{r}|^2$ can be neglected, the evolution is similar to that of a flat disk. However, the local angular momentum has a contribution given by the disk tilt even for small amplitude warps. In the case of high amplitude warps, where the second order derivatives of the unit vector can not be neglected, both the surface density, and the angular momentum evolve differently in comparison to a flat disk.

Equations (1.22) and (1.23) assume that the disk evolves only the under the effects of the viscous torques. If one wants to account for other possible torques acting on the disk, i.e. from a central radiation source, from a spinning black hole, or from the disk self-gravity, a term responsible for these torques has to be added to equation (1.23), and the evolution equations have to be solved self-consistently to account for the desired physics.

1.3.2 Warping Mechanisms for Nuclear/Accretion Disks

In the following, we summarize the most favorable warping mechanisms discussed so far in the literature.

Bardeen-Petterson Effect: An accretion disk close enough to a rotating black hole is subject to relativistic frame dragging if its angular momentum is misaligned with that of the black hole (Lense & Thirring, 1918). Frame dragging causes a differential precession of the disk with a rate given by (Kumar & Pringle, 1985):

$$\dot{\phi} = \frac{2G}{c^2} \frac{J_{bh}}{r^3},\tag{1.24}$$

where $J_{bh} = aGM_{bh}{}^2/c$ is the angular momentum of the black hole, and a is the black hole spin parameter taking values between 0 (for non-rotating black holes), and 1 (for maximally rotating black holes). Internal (viscous) torques try to align the disk angular momentum J_d with the black hole angular momentum. As we have seen, the viscous time scale increases with radius, hence the inner parts of the disk are forced to align with the black hole on time scales much shorter than those for the outer parts. Consequently, the disk develops a shape which for $r < R_{\mathrm{BP}}$ is aligned with the black hole, i.e. is flat, and for $r \geq R_{\mathrm{BP}}$ its angular momentum direction changes gradually from radius to radius. This is called the Bardeen-

Petterson effect (Bardeen & Petterson, 1975). The critical radius for Bardeen-Petterson warp-ing, assuming that the radial and vertical viscosities are equal, can be written as:

$$R_{\mathrm{BP}} = \frac{6aG^2 M_{\mathrm{bh}}^2 \Sigma \epsilon}{cL} \qquad (1.25)$$

In the limit where the misalignment of angular momenta of the disk and the black hole is small, Scheuer & Feiler (1996) calculated analytically the rate at which they become aligned. Assuming that the disk viscosity is constant throughout the disk, they showed that the align-ment timescale is given by:

$$t = \frac{3\nu_1}{\dot{M}} \left(\frac{acM_{bh}}{\nu_2 G} \right)^{1/2}. \qquad (1.26)$$

Natarajan & Armitage (1999) generalized this analytic solution to more strongly warped disks, considering a power-law radial dependence of viscous coefficients ν_1, and ν_2. Their simulations showed that for black holes with masses of order $10^8 \, M_\odot$, and accretion rates close to the Eddington limit, the alignment time scale is short ($t \leq 10^6$) yr. King et al. (2005) showed that for systems satisfying the condition $\theta > \pi/2$, and $J_d < 2J_{bh}$, the disk and the hole counter align for $t < t_{\mathrm{vis}}$, and eventually align when $t > t_{\mathrm{vis}}$, where θ is the mutual inclination between J_d, and J_{bh}.

Caproni et al. (2006a) applied the Bardeen-Petterson effect to the inferred warped disk of NGC1068. They found that the Bardeen-Petterson radius for this object is between 10^{-5} and 10^{-6} pc, which is well below the observed radius of the maser spots. The authors conducted a similar analysis to study the warped disk of NGC4258, and found that also for this galaxy, the warp radius lies below the inner radius of the maser disk (Caproni et al., 2007). Martin (2008) considered the same object allowing a more realistic surface density profile, and concluded that although the observations can be fit well, to reach a steady state the disk must be very long-lived.

Radiation Driven Warping: The effect of a central radiation source on the dynamics of a non-planar disk is known since the 1970s (Petterson, 1977). When a warped disk is exposed to radiation from a central source, or from its own inner portions, it is not illuminated isotropically. If it is also optically thick, the emission received at each position and re-radiated perpendicular to the local disk plane induces a torque on the disk, and the warp is modified. (Pringle, 1996) showed that perturbations to planar disks can cause radiation driven warping when:

$$L \geq 12\pi^2 \nu_2 \Sigma(r) v_\phi c. \qquad (1.27)$$

Defining $\eta = \nu_2/\nu_1$, and assuming the disk is in steady state, equation (1.27) can be expressed as a critical radius in terms of the Schwarzschild radius (Pringle, 1996):

$$\frac{r}{r_s} \geq \left(\frac{2\sqrt{2}\pi\eta}{\epsilon}\right)^2. \tag{1.28}$$

Assuming $\epsilon \sim 10^{-2}$, $\eta \sim 1$, and a black hole mass of $10^8 M_\odot$, equation (1.28) implies that the disk becomes warped beyond $r \geq 0.1$ pc. Maloney et al. (1996) studied the stable and unstable modes of radiatively excited linear warps. They showed that the inferred warps in NGC4258, Her-X1, and SS 433 might be explained by this mechanism as long as the radiative efficiency is high, but Caproni et al. (2006a) analyzing several AGN disks find that these are stable against radiation warping. Pringle (1997) considered the evolution of radiation driven warps with high amplitudes. Taking into account the self-shadowing of the disk, he showed that characteristic time scale for a disk orbiting a $10^8 M_\odot$ black hole is $t \sim 2 \times 10^6 \alpha^{-1}$.

Magnetically Driven Warps: When an accretion disk rotates around a magnetic star, the inner portions of the disk are subject to torques resulting from the interaction between the horizontal magnetic field of the star and induced electric currents on the surface of the disk. The warping and precession arising from such interactions was first studied by Lai (1999). In the linear regime, magnetic torque was modeled as an external torque acting on the disk. Pfeiffer & Lai (2004) carried this scenario to the nonlinear regime, and found that magnetically driven disks can develop highly inclined, steadily precessing warped configurations. Lai (2003) suggested a new mechanism, where the magnetic field was not external to the disk, but produced by outflows/jets, hence the scenario might well apply to AGN disks.

Gravity Driven Warps: A disk under the gravitational influence of its self-gravity and/or that of an other nearby object exists in a variety of astrophysical systems. For such disks, the quadrupole moment of the nearby object, when present, induces a differential precession of the disk, while self-gravity usually acts to prevent differential precession of its elements, such that the disk shape stays intact. Warps generated by gravitational interactions are studied in detail in numerous works on galactic disks (Hunter & Toomre, 1969; Toomre, 1983; Sparke, 1986; Arnaboldi & Sparke, 1994; Kuijken, 1991), and in the context of rings around planets (Borderies et al., 1983; Goldreich & Tremaine, 1979). On the nuclear/accretion disk scales, Papaloizou et al. (1998) studied the evolution of a thin self-gravitating viscous disk, with application to NGC4258. They found that when the density wave crossing time is much smaller than the dynamical time scale, the disk precesses rigidly. They concluded that the

warp in the maser disk of NGC4258 might have been excited by a binary companion having a mass comparable to or higher than that of the maser disk. Their model also suggests a small twist (i.e. varying line-of-nodes) due to viscosity. Nayakshin (2005) considered the case of a light non-self-gravitating disk perturbed by a massive ring. He modeled the disk as a collection of many rings. Employing the gravitational torques in the linear regime, he found that the rate of precession induced by the interaction of two rings with radii r and r_1 is:

$$\dot{\phi} \rightarrow -\frac{3M_1}{4M_{bh}}\cos\beta\frac{r^3}{r_1{}^3}\Omega \ \text{ for } r \ll r_1, \tag{1.29}$$

and

$$\dot{\phi} \rightarrow -\frac{3M_1}{4M_{bh}}\cos\beta\frac{r_1{}^2}{r^2}\Omega \ \text{ for } r \gg r_1. \tag{1.30}$$

Here, M_1 is the mass of the ring, and β is the mutual inclination between the rings. Already in this linear regime, Nayakshin (2005) argued that very high inclination are possible for nuclear disks in galaxies, and revisiting the idea of Phinney (1989), he suggested that such warps might be an ingredient in AGN unification theories. The importance of self-gravity can readily be seen from equations (1.29), and (1.30). When it is absent, the rings making up the disk precess differentially, tending to destroy the disk structure. Numerical simulations dedicated to Galactic Center stellar disks discussed in section (1.1.1) showed that, it is possible to constrain the masses of the disks in the warped disk scenario. The model disks with $M_d > 0.005M_{bh}$ lead to too much warping of the disk, i.e. β in equations (1.29)-(1.30), and do not explain the data.

1.4 Outline of the Thesis

This thesis is organized as follows:

In Chapter 2, a nonlinear model for steadily precessing, self-gravitating warped disks around nuclear black holes is introduced. The model considers the disk as a collection of circular rings inclined with respect to eachother, and which are in mutual gravitational interaction. Starting from the steady state equations of motion, a scaling relation is derived relating the global precession frequency of the disk to the disk mass in proportion to the black hole mass. Steadily precessing equilibrium solutions are evaluated for 2, 3, and many ring systems for various disk surface density profiles, mass fractions, radial extents, and precession frequencies. The linear theory of self-gravitating warped disks is revisited in order

to highlight the major differences resulting from both approaches. Using perturbation theory, the stability of the non-linear warps is studied, and checked by integration of the equations of motion for a few examples.

Chapter 3 proposes a new scenario for the formation mutually inclined warped disks around nuclear black holes in application to the Galactic Center. Assuming a radiation or Bardeen-Petterson warping origin, the time evolution of warped stellar disks with parameters relevant to the Galactic Center is followed. A qualitative comparison of the simulations to the observations is presented at the end of the chapter.

In Chapter 4, the outcomes of this thesis are summarized, and an outlook is presented.

CHAPTER 2

SELF-GRAVITATING WARPED DISKS AROUND SUPERMASSIVE BLACK HOLES *

Abstract

We consider warped equilibrium configurations for stellar and gaseous disks in the Keplerian force-field of a supermassive black hole, assuming that the self-gravity of the disk provides the only acting torques. Modeling the disk as a collection of concentric circular rings, and computing the torques in the non-linear regime, we show that stable, strongly warped precessing equilibria are possible. These solutions exist for a wide range of disk-to-black hole mass ratios M_d/M_{bh}, can span large warp angles of up to $\pm \sim 120°$, have inner and outer boundaries, and extend over a radial range of a factor of typically two to four. These equilibrium configurations obey a scaling relation such that in good approximation $\dot{\phi}/\Omega \propto M_d/M_{bh}$ where $\dot{\phi}$ is the (retrograde) precession frequency and Ω is a characteristic orbital frequency in the disk. Stability was determined using linear perturbation theory and, in a few cases, confirmed by numerical integration of the equations of motion. Most of the precessing equilibria are found to be stable, but some are unstable. The main result of this study is that highly warped disks near black holes can persist for long times without any persistent forcing other than by their self-gravity. The possible relevance of this to galactic nuclei is briefly discussed.

2.1   Introduction

The increasing power and spatial resolution of modern observations has provided evidence that warps are not unique to galactic disks, but appear also on much smaller scales. These include nuclear and accretion disks surrounding supermassive black holes in galactic nuclei (nuclear disks hereafter). The pioneering example is the maser disk of NGC4258. The high velocity masers mapped by Miyoshi et al. (1995) are best explained by the existence of a mildly warped disk extending from 0.13 to 0.26 pc (Herrnstein et al., 1996). The nearby Seyfert galaxies NGC1068 and Circinus also harbor warped disks in their centers, again traced by the maser emission (Greenhill et al., 2003; Gallimore et al., 2004). Of the ~ 100 massive young stars in the center of our Galaxy about half form a well-defined, warped disk, and some of the others are on a counter-rotating structure which may be a dissolving disk (Genzel et al., 2003; Paumard et al., 2006; Lu et al., 2009; Bartko et al., 2009).

Nuclear disks can develop a warped shape through several mechanisms. Very close to the center, the dragging of inertial frames by a rotating black hole (Lense & Thirring, 1918) causes precession of a planar disk, if it is inclined to the plane perpendicular to the black hole's spin. Internal viscous torques try to align the disk angular momentum with the black hole angular momentum. Beyond a transition radius, the disk does not feel the effect of the black hole and remains at its initial inclination, while inside this radius the alignment proceeds. Hence the disk becomes warped [the Bardeen & Petterson (1975) effect]. Natarajan & Armitage (1999) showed that for black holes with masses of order 10^8 M$_\odot$ and accretion rates close to the Eddington limit the alignment time scale is short ($t \leq 10^6$yr). Application of this effect to the warped disks of NGC4258 and NGC1068 shows that the alignment radius lies well inside the observed positions of the maser spots, and models can be constructed that fit the observed warps rather well (Caproni et al., 2007; Martin, 2008).

When a warped disk is exposed to radiation from a central source, or from its own inner portions, it is not illuminated isotropically. If it is also optically thick, the emission received at each position and re-radiated perpendicular to the local disk plane induces a torque on the disk, and the warp is modified (Petterson, 1977). Perturbations to planar disks can therefore cause radiation driven warping (Pringle, 1996). Assuming a radiative efficiency $\epsilon \sim 10^{-2}$, and a black hole mass of 10^8 M$_\odot$, an initially flat disk is prone to warping beyond $r \geq 0.1$ pc, when the vertical and radial viscosity coefficients are comparable (Pringle, 1997). Maloney et al. (1996) studied the stable and unstable modes of radiatively excited linear warps and found that the warp in NGC4258 may be explained by this mechanism only

if the radiative efficiency is high.

Warps generated by gravitational interactions have been investigated mainly in the galactic context. Hunter & Toomre (1969) studied the linear bending waves of a self-gravitating, isolated, thin disk. They showed that such a disk permits long-lasting bending modes only when its surface density near the outer radius is truncated sufficiently fast, but not when realistic smooth edges are considered. This suggested interactions with nearby companion galaxies as a likely cause of warp excitation. Later, as the evidence for dark matter halos around galaxies became stronger, modelers developed scenarios in which the disk assumes the shape of a normal mode in the potential of a flattened dark halo (Sparke, 1984; Kuijken, 1991). However, subsequent work showed that these modes are damped quickly when the internal dynamical response of the halo is taken into account (Nelson & Tremaine, 1995; Binney et al., 1998). Today, it seems most plausible that galactic warps result from interactions and from accretion of material with misaligned angular momentum (Jiang & Binney, 1999).

On nuclear disk scales, Papaloizou et al. (1998) studied in linear theory the evolution of a thin self-gravitating viscous disk interacting with a massive object orbiting the central mass, with application to NGC4258. They concluded that the warp in the maser disk of NGC4258 might have been excited by a binary companion with a mass comparable to or higher than that of the maser disk. Their model also suggests a small twist (i.e. varying line-of-nodes) due to viscosity. Nayakshin (2005) considered the case of a non-self-gravitating disk perturbed by a massive ring. Employing the gravitational torques in the linear regime, he evaluated the precession induced by the ring on the disk elements. When the self-gravity of the disk is not taken into account, the rings precess differentially, which tends to destroy the disk structure.

Can models of warped nuclear disks be generalized to the fully non-linear regime? And assuming that the observed warps in galactic nuclei have been excited by one of the mechanisms discussed above, can the disk self-gravity maintain the warp even after the exciting torque has ceased to exist? As a first step towards answering these questions, the goal of the present paper is to investigate the possibility of steadily precessing, stable, non-linearly warped self-gravitating disks in the (Keplerian) gravitational potential of a massive black hole. In the following sections, we use a simple circular orbit ring model to find stable warped equilibria for systems with 2, 3, and many rings, assuming that the self-gravity of the rings provides the only acting torques.

2.2   Steadily Precessing Warped Disks and Their Scaling Relation

2.2.1   Cold Disk Model and Equations of Motion

We consider a cold disk in which stars or gas are assumed to move on very nearly circular orbits. Following similar analysis of galactic warps (e.g., Toomre 1983, Sparke 1984, Kuijken 1991) we model such a disk as a collection of concentric circular rings. The orbital motion in the disk is maintained by the central black hole, and the self-gravity of the disk causes the rings to precess around the total angular momentum direction. Each ring may represent a set of stars or gas elements uniformly spread around their circular orbit. Moreover, when the precession frequency arising from the self-gravity of the disk is small compared to the orbital frequency of motion, the orbital parameters of single stars change only slowly and so one can average over the orbital motion. In this case, also the force exerted by a single star or mass element on the rest of the disk can be replaced by the force due to a ring of material spread over the orbit (Goldreich, 1966).

Any of the rings is characterized by its mass m_i, radius r_i, inclination angle θ_i with respect to the reference plane, and azimuthal angle ϕ_i where the line-of-nodes cuts this plane. Later we will identify the reference plane as the plane perpendicular to the total angular momentum vector. The Lagrangian $\mathcal{L}_i$ of ring i is given by (Goldstein et al., 2002):

$$\mathcal{L}_i \;=\; \frac{m_i r_i^2}{4}(\dot{\theta}_i^2 + \dot{\phi}_i^2 \sin^2 \theta_i) + \frac{m_i r_i^2}{2}(\dot{\psi} + \dot{\phi}_i \cos \theta_i)^2$$
$$- V(r_i, \theta_i, \phi_i). \tag{2.1}$$

The first two terms in equation (2.1) represent the kinetic energy of the motion T_i, $V(r_i, \theta_i, \phi_i)$ represents the gravitational potential energy, the Lagrangian is $\mathcal{L}_i = T_i - V_i$, and the energy of a ring is $E_i = T_i + V_i$. ψ is the position of a point on the ring, measured from the ascending node; (θ, ϕ, ψ) are Euler angles. The angular momentum of the motion along the ring

$$p_{\psi_i} = m_i r_i^2 \Omega(r_i) = m_i r_i^2 (\dot{\psi} + \dot{\phi}_i \cos \theta_i) \tag{2.2}$$

is conserved since $\mathcal{L}_i$ does not depend on the coordinate ψ. The other momenta are the p_{ϕ_i}, the angular momentum around the $z-$direction, and p_{θ_i}, the angular momentum around the

line of nodes. The equations of motion are:

$$p_{\theta_i} = \frac{m_i r_i^2}{2} \dot{\theta}_i, \tag{2.3}$$

$$p_{\phi_i} = \frac{m_i r_i^2}{2} \dot{\phi}_i \sin^2 \theta_i + p_{\psi_i} \cos \theta_i \tag{2.4}$$

$$\dot{p}_{\theta_i} = \frac{m_i r_i^2}{2} \dot{\phi}_i^2 \sin \theta_i \cos \theta_i - \dot{\phi}_i p_{\psi_i} \sin \theta_i - \frac{\partial V(r_i, \theta_i, \phi_i)}{\partial \theta_i} \tag{2.5a}$$

$$= -\frac{\partial V(r_i, \theta_i, \phi_i)}{\partial \theta} - 2 \frac{(p_{\phi_i} - p_{\psi_i} \cos \theta_i)(p_{\psi_i} - p_{\phi_i} \cos \theta_i)}{m_i r_i^2 \sin^3 \theta_i} \tag{2.5b}$$

$$\dot{p}_{\phi_i} = -\frac{\partial V(r_i, \theta_i, \phi_i)}{\partial \phi_i} \tag{2.6}$$

and the Hamiltonian is:

$$\mathcal{H}_i = \frac{p_{\theta_i}^2}{m_i r_i^2} + \frac{1}{2} \frac{p_{\psi_i}^2}{m_i r_i^2} + \frac{(p_{\phi_i} - p_{\psi_i} \cos \theta_i)^2}{m_i r_i^2 \sin^2 \theta_i} + V(r_i, \theta_i, \phi_i). \tag{2.7}$$

2.2.2 Components of $V(r, \theta, \phi)$, and Evaluation of the Torques

The gravitational potential energy, $V(r, \theta, \phi)$, has two components. One arises due to the central black hole, and is simply

$$V_{bh} = -\frac{G m_i M_{bh}}{r_i}. \tag{2.8}$$

at the position of the ring. The other component is the potential term V_m arising from the interaction of the ring under consideration with all other rings. We follow the description of Arnaboldi & Sparke (1994), using the derivation of Binney & Tremaine (1987) (Section 2.6.2), to evaluate the torque arising from the ring interactions.

The gravitational potential due to a circular ring of mass m_i and radius r_i in the $(\tilde{x}, \tilde{y})$ plane is

$$\Phi(\tilde{x}, \tilde{y}, \tilde{z}) = -\frac{2 G m_i}{\pi} \frac{K(k) \sqrt{(1 - k^2/2)}}{\sqrt{(r^2 + r_i^2)}}, \tag{2.9}$$

where

$$k^2 = \frac{4 R r_i}{(r^2 + r_i^2 + 2 R r_i)}. \tag{2.10}$$

Here $K(k)$ is the complete elliptic integral of the first kind, and R is the cylindrical radius $R^2 = \tilde{x}^2 + \tilde{y}^2$, so that $R^2 = r^2 - \tilde{z}^2$. A second ring of radius r_j at an angle α_{ij} to the first ring follows a curve $\tilde{z} = r_j \sin\alpha_{ij} \sin\psi$, where ψ runs between 0 and 2π. The mutual potential energy is

$$V_{ij}(\alpha_{ij}) = -\frac{Gm_i m_j}{\pi^2 (r_i^2 + r_j^2)^{1/2}} \int_0^{2\pi} K(k)\sqrt{1 - k^2/2}\,d\psi \qquad (2.11)$$

where m_j is the mass of the second ring, and k depends on r_i/r_j, $\sin\alpha_{ij}$ and ψ. The angle α_{ij} between the two rings is given by

$$\cos\alpha_{ij} = \cos\theta_i \cos\theta_j + \sin\theta_i \sin\theta_j \cos(\phi_i - \phi_j), \qquad (2.12)$$

which reduces to $\cos\alpha_{ij} = \cos(\theta_i - \theta_j)$ when the line-of-nodes are aligned ($\phi_i = \phi_j$). The torque between the two rings (i, j) is

$$\frac{\partial V_{ij}}{\partial \alpha_{ij}} = \frac{Gm_i m_j r_i r_j \sin 2\alpha_{ij}}{(r_i^2 + r_j^2)^{3/2}}\, I_{ij}(\alpha_{ij}, r_i/r_j), \qquad (2.13a)$$

$$
\begin{aligned}
I_{ij} \;\equiv\; &\frac{4}{\pi^2} \int_0^{\pi/2} \left[\frac{E(k)(1 - k^2/2)}{(1 - k^2)} - K(k) \right] \\
&\times \frac{(1 - k^2/2)^{3/2}}{k^2}\, \frac{\sin^2\psi\,d\psi}{\sqrt{1 - \sin^2\alpha_{ij}\sin^2\psi}}.
\end{aligned}
\qquad (2.13b)
$$

We use the numerical program of Arnaboldi & Sparke (1994) for evaluating the integrals in this expression. The torques with respect to the angles (θ_i, ϕ_i) follow from multiplying equation (2.13a) by $\partial\alpha_{ij}/\partial\theta_i$ or $\partial\alpha_{ij}/\partial\phi_i$. In the following, we will write $V_{m,i} \equiv \sum_{j \neq i} V_{ij}$ for the potential energy of ring i due to the other rings, so that its *total* potential energy becomes $V(r_i, \theta_i, \phi_i) = V_{bh}(r_i) + V_{m,i}$. For further reference we also define $M_{ij} \equiv -\partial V_{ij}/\partial\theta_i$, and $M_{G,i} \equiv -\partial V_{m,i}/\partial\theta_i$ for the total gravitational torque on ring i around its line-of-nodes.

Figure 2.1 shows the torque between two rings with radii in the ratio $\nu \equiv r_{\mathrm{out}}/r_{\mathrm{in}}$ as a function of their mutual inclination α. The maximum of the torque occurs at very small angles, as noted previously by Kuijken (1991) who gives the approximation $\alpha_{\max} \simeq 1.2|\nu - 1|$. Only for $\alpha < \alpha_{\max}$ can the mutual torque be approximated as a linear function of α. Thus solutions $\theta(r)$ for the warp shape in linear theory can be scaled by a constant multiplicative factor only so long as the local gradient $d\theta/dr < 1.2/r$. Otherwise the local self-gravity torques of the disk are no longer able to maintain the linear theory warp shape, the non-linear
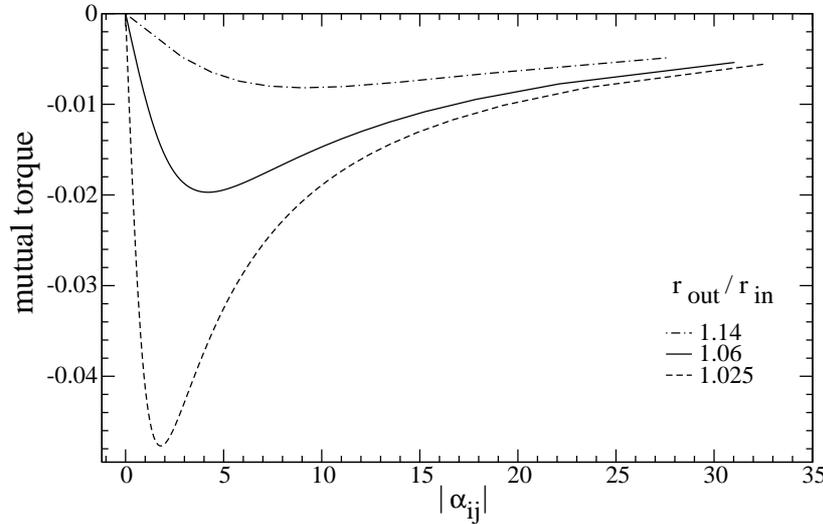
Figure 2.1: The mutual torque between two neighboring concentric rings, whose radii r_{out} and r_{in} are in the ratio ν as specified on the plot. The linear regime is limited to the left of the peak amplitude in these curves.

equations must be used, and the shape of the warp must change.

2.2.3 Steadily Precessing Equilibria

A configuration of inclined rings precessing as a rigid body with constant $\dot{\phi}$ will in the following be denoted as a steadily precessing equilibrium, or equilibrium for short. In earlier works by Hunter & Toomre (1969); Sparke (1984), and Sparke & Casertano (1988) it was found that the eigenfrequencies of linear m=1 warp modes are purely real. Papaloizou et al. (1998) showed that this is a consequence of the self-adjointness of the operator in the tilt equation when there are no viscous or non-conservative forces. Then the eigenvectors are also real and thus the warp has a straight line-of-nodes and no spirality[1]. In the light of these linear theory results our effort will also be to find equilibria where all the rings have the same azimuth ϕ. The condition that all rings maintain constant inclination, $\dot{\theta} = 0$, implies also $\dot{p}_\theta = 0$, and for a given precession rate $\dot{\phi}$, the simultaneous solution of this equation for each of the rings determines the inclination angles, i.e. the equilibrium shape corresponding to this value of $\dot{\phi}$. We note that for $\dot{\phi} = 0$ equations (2.5a) admit a trivial tilt solution $\theta_i = \text{const.}$ but will

---

[1]The line-of-nodes for a set of orbits is here defined as the union of points where all inclined orbits ($\theta_i \neq 0$) with respect to the reference plane intersect this plane.

assume $\dot{\phi} \neq 0$ in what follows.

From equations (2.5a) and (3.23) we can solve for the precession rate of ring i:

$$\dot{\phi}_i = \frac{\Omega_i}{\cos\theta_i} \pm$$
$$\sqrt{\frac{\Omega_i^2}{\cos^2\theta_i} + \frac{2}{m_i r_i^2 \cos\theta_i \sin\theta_i} \sum_j \frac{\partial V_{ij}}{\partial\theta_i}} \qquad (2.14)$$

when $\theta_i \neq 0$. Here $\Omega_i = \sqrt{GM_{bh}/r_i^3}$ is the angular velocity of particles on the ring around the black hole, and the term $\sum_j \partial V_{ij}/\partial\theta_i$ is the torque on ring i caused by all other rings j. The precession rate can therefore be fast or slow, corresponding to the plus and minus signs in this expression. When the interaction potential V_{ij} increases away from the plane $\theta = 0$, the second term in the square root is positive, so that the slow precession is retrograde ($\dot{\phi} < 0$). In the remainder of this paper we focus on such slow retrograde precession.

The components of angular momentum along the original (x, y, z) axes for a single ring read:

$$l_{x_i} = p_{\theta_i} \cos\phi_i + \frac{\sin\phi_i(p_{\psi_i} - p_{\phi_i}\cos\theta_i)}{\sin\theta_i}, \qquad (2.15)$$

$$l_{y_i} = p_{\theta_i} \sin\phi_i - \frac{\cos\phi_i(p_{\psi_i} - p_{\phi_i}\cos\theta_i)}{\sin\theta_i}, \qquad (2.16)$$

$$l_{z_i} = p_{\phi_i}. \qquad (2.17)$$

Let us assume that we have found a precessing equilibrium from solving equations (3.21-3.24), with $p_{\theta_i} = 0$, $\dot{p}_{\theta_i} = 0$, and $p_{\phi_i} = \text{const.}$, $\dot{\phi} = \text{const.}$, $\phi_i = \phi$. Inserting equations (2.5a) and (3.22) into the expression for l_{x_i}, simplifying and summing over all rings gives the total angular momentum

$$l_x = \sum_i l_{x_i} = -\frac{\sin\phi}{\dot{\phi}} \sum_{i \neq j} \frac{\partial}{\partial\theta_i} V_{ij} = 0 \qquad (2.18)$$

which sums to zero because for each pair of rings with interaction potential V_{ij} the torques are equal and opposite. Similarly, the total $l_y = 0$. Thus the total angular momentum of such a precessing equilibrium configuration is parallel to the z-axis. By construction, the angular momentum of the precession alone is also along the z-axis, i.e., the disk precesses around the total angular momentum vector axis.

For a uniformly precessing configuration, additional insight may be obtained by moving to a coordinate system which rotates around the angular momentum axis with the disk's precession frequency $\dot{\phi}$ (Kuijken 1991). In this reference frame the shape of the precessing

disk is stationary, but the particles in the different rings still spin about their rings' symmetry axes. If the particles in ring i rotate with velocity $\Omega(r_i)r_i$ in the positive sense, they experience a Coriolis force in the rotating system which, integrated over the ring, results in a Coriolis torque on ring i along the p_θ-axis (line-of-nodes), given by

$$M_{C,i} = -m_i r_i^2 \Omega(r_i) \dot{\phi} \sin \theta_i. \tag{2.19}$$

For $0 < \theta < \pi/2$ and negative $\dot{\phi}$ this torque is along the positive p_θ-axis, i.e., is trying to retard the ring relative to the rotating frame. Because the retrograde precession speeds are small, we can neglect the centrifugal force terms. In this case, a stationary precessing configuration is obtained when the forward gravity torques and the retarding Coriolis torque balance in the rotating frame.

2.2.4 2-Ring and 3-Ring Cases

The argument just described suggests that there should exist steadily precessing 2-ring configurations in which one ring is tilted above the plane $\theta = 0$ and a second ring is tilted below this plane. Both rings are pulled towards $\theta = 0$ by the gravitational force from the other ring. The resulting gravity torques cause the angular momentum vectors of the two rings to precess in the same sense, and are balanced by the Coriolis torques in the precessing frame. To find such configurations we need to solve $\dot{p}_\theta = 0$ using eq. (2.5a) for both rings simultaneously. Assuming $\dot{\phi} \ll \Omega$, we can neglect terms of order $\dot{\phi}^2$; then using eq. (3.23) the equation for the inner ring at r_1 becomes

$$\sin \theta_1 \simeq -\frac{\partial V_{12}}{\partial \theta_1} / m_1 r_1^2 \Omega(r_1) \dot{\phi} \tag{2.20}$$

and the ratio of the two equations is

$$\sin \theta_1 / \sin \theta_2 \simeq -m_2 r_2^2 \Omega(r_2) / m_1 r_1^2 \Omega(r_1), \tag{2.21}$$

where m_1, m_2 are the two ring masses, r_1, r_2 their radii, θ_1, θ_2 their inclinations, and V_{12} the interaction potential. Given the ring masses and radii and θ_1, say, we can determine from these equations θ_2, the interaction potential, and thus finally the precession rate $\dot{\phi}$ required for steady precession.

Using the expression in (2.13a) for the torque between the rings, equation (2.20) can be
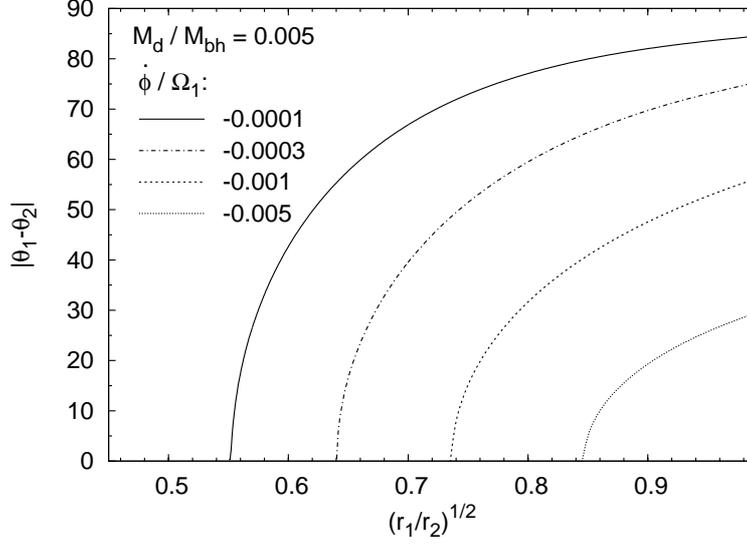
Figure 2.2: Relative inclination of two rings precessing together around a central mass M_{bh}, as a function of the square root of the ratio of their radii. The combined mass of the two rings is 0.5% of the central mass, approximately as in the Galactic center. The different curves are for various values of the precession frequency of the two-ring system, in units of the Keplerian frequency at r_1.

cast into a more useful form:

$$\frac{\dot{\phi}}{\Omega_1} = -\frac{\sin 2\alpha \; I_{12}(\alpha, \nu)}{\sin \theta_1} \frac{\nu \mu}{(1+\nu^2)^{3/2}} \frac{m_1}{M_{bh}}, \tag{2.22}$$

where the angle $\alpha = \theta_1 - \theta_2$, $\nu \equiv r_2/r_1$, $\mu = m_2/m_1$, and I_{12} denotes the integral expression of equation (2.13b).

Figure 2.2 shows the difference $\theta_1 - \theta_2$ between the inclination angles of the two rings versus the square root of the ratio of their radii, r_1/r_2, for different precession frequencies, expressed in units of the Keplerian frequency at r_1. The combined mass of the two rings is chosen to be 0.5% of the central mass, approximately as inferred for the system of two stellar rings in the Galactic center (Genzel et al., 2003). $\theta_1 - \theta_2$ increases with decreasing precession speed when the mass ratio is fixed. Eq. (2.22) shows that the same precessing equilibrium configuration can be obtained by changing $\dot{\phi} \propto M_d = m_1 + m_2$ and leaving all other parameters unchanged. More massive rings must precess faster for the same inclinations. Thus the sequence of curves in Fig. 2.2 can also be interpreted as a sequence of fixed precession frequency but with mass ratio M_d/M_{bh} increasing from bottom right to upper left.

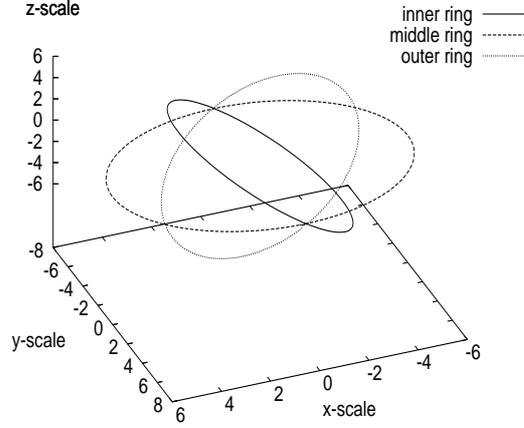Next consider three rings. In this case, each of the rings precesses in the potential of

Figure 2.3: 3D view of a 3-ring system. The middle ring lies close to the equator, while the others are distributed almost symmetrically around it.

the other two rings, and the reference frame is defined by the common plane of precession perpendicular to the total angular momentum vector. Again $\dot{p}_\theta$ [eq. (2.5a)] should be zero at equilibrium for each of the rings. We can sum these three equations:

$$\sum_i^3 \dot{p}_{\theta_i} = \sum_{i=1}^3 \left(\frac{m_i r_i^2}{2} \dot{\phi}^2 \sin \theta_i \cos \theta_i - \dot{\phi} p_{\psi_i} \sin \theta_i \right)$$
$$- \sum_{i=1}^3 \sum_{j \neq i} \frac{\partial V_{ij}}{\partial \theta_i} = 0. \tag{2.23}$$

The V_{ij} terms cancel since $\partial V_{ij}/\partial \theta_i = -\partial V_{ij}/\partial \theta_j$. The remaining terms can be rewritten as

$$\dot{\phi} \left(\sum_{i=1}^3 m_i r_i^2 \sin \theta_i \left[-\Omega(r_i) + \frac{1}{2} \dot{\phi} \cos \theta_i \right] \right) = 0, \tag{2.24}$$

making use of eq. (3.23). This shows that, apart from the no-precession solution, a steadily precessing equilibrium is possible only when at least one of the rings lies on the opposite side of the equator with respect to the others, i.e., has $\theta_i < 0$. Likewise the two rings of a precessing two-ring system must lie on opposite sides of the equator. Figure 2.3 shows as an example the 3D view of a 3-ring system with mass $M_d = 0.05 M_{bh}$ and $\dot{\phi} = -0.0021 \Omega(r_2)$.
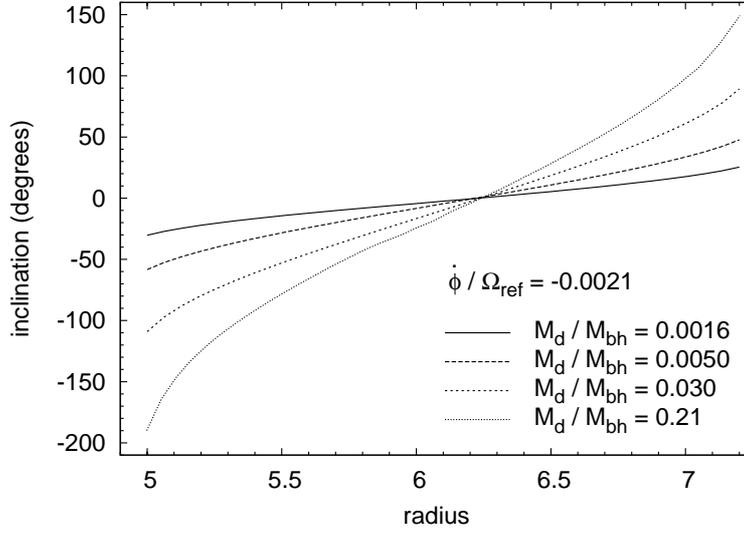
Figure 2.4: Inclination of a disk of constant surface density at different radii. The model consists of 35 rings precessing at a rate of $\dot{\phi} = -10^{-3}$ units, so that $\dot{\phi}/\Omega(r_{\mathrm{ref}}) = -0.0021$ on its middle (reference) ring. Each curve corresponds to a different M_d/M_{bh} mass fraction. The warp becomes more pronounced when the disk mass is increased. The smallest and highest masses correspond to the limits for stability (see Section 2.2.7).

2.2.5   Approximation of A Disk With n-Rings

We now consider a disk represented as a collection of n concentric rings. To find a precessing equilibrium, we solve $\dot{p}_\theta = 0$ (eqs. 2.5a) for all rings simultaneously, summing over the torques from all other rings (eqs. 2.13a). These are n equations for n+1 unknowns, the n inclinations θ_i and $\dot{\phi}$, which we solve keeping $\dot{\phi}$ fixed (Arnaboldi & Sparke, 1994)[2]. Figure 2.4 shows a sequence of equilibria obtained for a constant surface density disk consisting of 35 rings. On each curve, the extent of the disk (*i.e.* $\Delta r = r_{\mathrm{out}} - r_{\mathrm{in}}$) is fixed at 2.2 units, and the precession rate is $\dot{\phi}/\Omega(r_{\mathrm{ref}}) = -0.0021$ where $\Omega(r_{\mathrm{ref}})$ is the circular frequency on the middle (reference) ring. The disk mass fraction M_d/M_{bh} varies from 0.16% to 21%. As the mass of the disk increases, the degree of warping increases dramatically so that the Coriolis torques can keep the balance of the gravity torques. The basic shape of the disk is similar to that of the system of three rings in Fig. 2.3. The middle rings lie closest to the equator, while the inner and outer rings are almost symmetrically distributed around it.

Obviously, the larger the number of rings the better the approximation to a continuous disk. Figure 2.5 shows the convergence of the total torques (upper panel), and of the inclina-

---

[2]Note that this does not work in linear theory because the linear solution can be scaled arbitrarily, i.e., one of the θ_i can be eliminated.
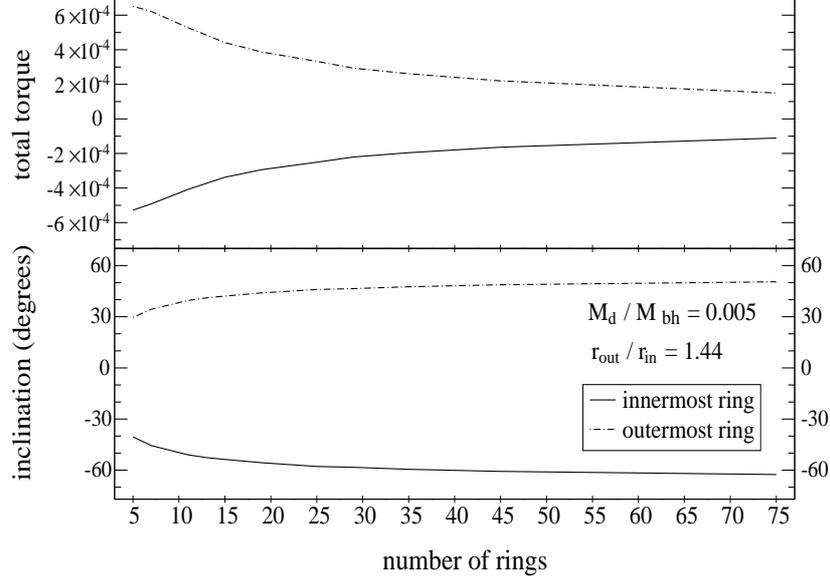
Figure 2.5: Convergence of the total torques (upper panel), and inclinations (lower panel), for the innermost (solid lines) and outermost rings (dot-dashed lines), when the number of rings to represent the disk is increased but the extent and the mass of the disk are kept fixed.

tion angles obtained in steadily precessing equilibrium (lower panel), for the innermost and outermost rings, when the number of rings to represent the disk is increased but the extent and the mass of the disk are kept fixed. One sees that quite a number of rings are needed before the torques converge. The inclination of the outer and inner rings have approximately converged when $n \gtrsim 30$.

2.2.6   Scaling the Solutions

Now we go back to the equilibria themselves, in particular to the question of their scaling properties. When the torque on ring i from all other rings is decomposed as

$$M_{G,i} = -\sum_j \frac{\partial V_{ij}}{\partial \theta_i} = -\sum_j \frac{\partial V_{ij}}{\partial \alpha_{ij}} \frac{\partial \alpha_{ij}}{\partial \theta_i}, \qquad (2.25)$$

the mass- and radius-dependent part is the first derivative on the r.h.s. The second factor in each term of this sum depends from equation (2.12) only on the two sets of angles θ_i, ϕ_i, θ_j, ϕ_j. For equilibria with a common precessing line-of-nodes, $\alpha_{ij} = (\theta_i - \theta_j)$, so the deriva-
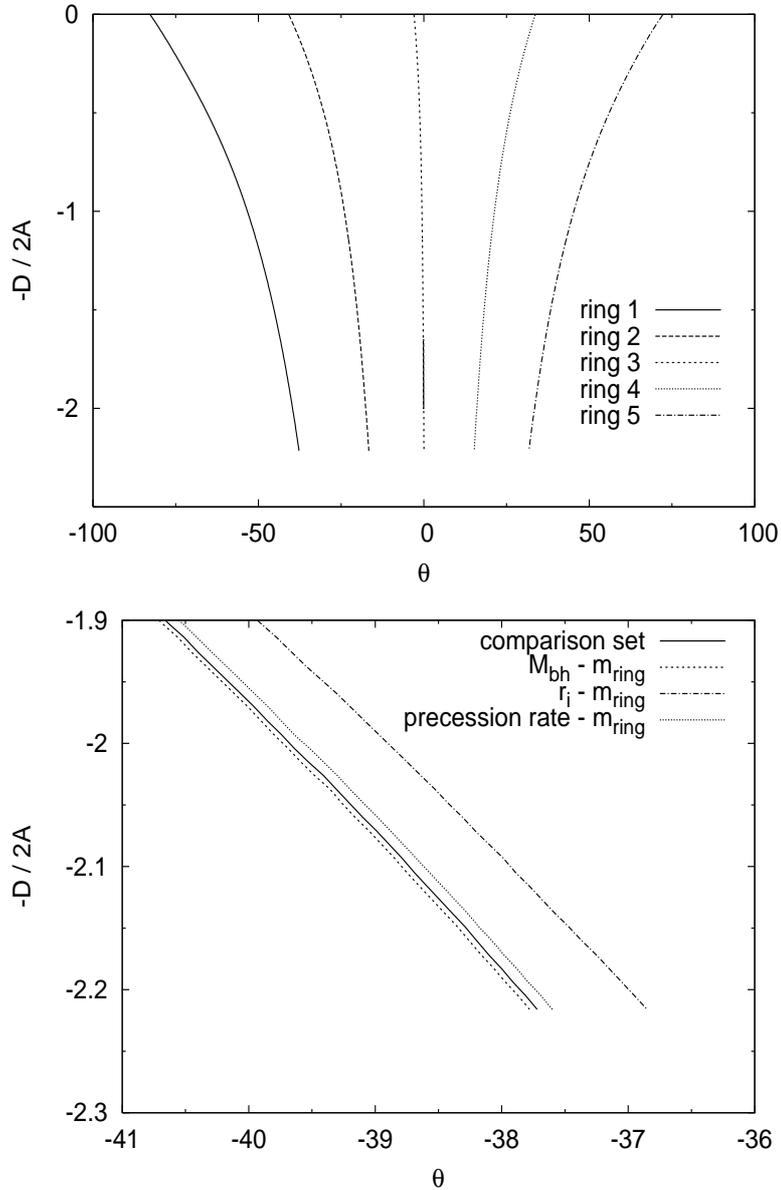
Figure 2.6: Top: Values $-D_i/2A_i$ (eq. 2.28) for a system of 5 rings with the parameters described in the text. The absolute value of the precession speed increases along the curves from top to bottom. Bottom: Parameter scaling of this system according to eq. (2.28). This figure shows a zoom into the region where the orientation of the 1st ring predicted by the scaling deviates from the orientation in the original 5 ring model (shown as the solid line). Dots show when the black hole mass is increased by a factor of 4 and the ring mass is increased by a factor of 2, the dotted-dashed line shows when the radius is increased by a factor of 4 and ring mass by a factor of 8, and the long dashed line shows when the scaling is done by increasing the precession rate by a factor of 2 while increasing again the ring mass by a factor of 2.

tive is always unity. For the potential derivative terms, we use equation (2.13a) and express all ring masses and radii in terms of the mass and radius of a reference ring, i.e., we write $\mu_i \equiv m_i/m_{\text{ref}}$, $\nu_i \equiv r_i/r_{\text{ref}}$, and similar for j. Then (2.25) takes the form:

$$M_{G,i} = -\frac{Gm_{\text{ref}}^2}{r_{\text{ref}}} \underbrace{\left[\sum_j \frac{\mu_i \mu_j \nu_i \nu_j \sin \alpha_{ij}}{(\nu_i^2 + \nu_j^2)^{3/2}} I_{ij}(\alpha_{ij}, \nu_i, \nu_j) \right]}$$
(2.26)

where we denote the expression over the brace as $D_i/2$. For each precessing equilibrium disk configuration as in Fig. 2.4 D_i is a constant, and the torques on all rings scale as $\propto m_{\text{ref}}^2/r_{\text{ref}}$. If we now go back to equation (2.14), insert equation (2.26), and normalize the precession rate with the circular frequency at the reference radius, $\Omega_{\text{ref}} \equiv (GM_{bh}/r_{\text{ref}}^3)^{1/2}$, we find

$$\frac{\dot{\phi}_i}{\Omega_{\text{ref}}} = \frac{1}{\nu_i^{3/2} \cos \theta_i} \left(1 \pm \sqrt{1 + \frac{\nu_i \cos \theta_i}{\mu_i \sin \theta_i} D_i \frac{m_{\text{ref}}}{M_{bh}}} \right).$$
(2.27)

For negative $\dot{\phi}$ and after a Taylor expansion of the term in the square root, appropriate for slow retrograde precession, equation (2.27) becomes

$$\frac{\dot{\phi}_i}{\Omega_{\text{ref}}} \simeq -\frac{D_i}{2\mu_i \nu_i^{1/2} \sin \theta_i} \frac{m_{\text{ref}}}{M_{bh}} \equiv -\frac{D_i}{2A_i} \frac{m_{\text{ref}}}{M_{bh}}.$$
(2.28)

A precessing equilibrium is one for which all rings precess with the same common frequency, $\dot{\phi}_i = \dot{\phi}$. Equation (2.28) thus shows that for a fixed precessing disk mass configuration (i.e., fixed ring masses, radii, and inclinations, hence fixed $D_i/2A_i$), the precession rate $\dot{\phi}$ scales proportional to the Keplerian frequency at some reference radius in the disk and proportional to the disk-to-black hole mass ratio. Vice versa, equation (2.28) can be interpreted as a scaling relation which says that a precessing equilibrium solution remains unchanged in shape (θ_i) under changes of the disk mass, disk radius, black hole mass, and precession rate, provided the ratio $(\dot{\phi}/\Omega_{\text{ref}})/(M_d/M_{bh})$ is held constant.

Figure 2.6 depicts the values of $-D_i/2A_i$ for a system of 5 rings. The radii of the rings are calculated such that $r_i = \kappa^{i-1} \times r_1$, with $i = 1, 2, ..n$, $\kappa = 1.07$, $r_1 = 5.75$, and $n = 5$, so if the third ring is the reference ring, $\nu_i = \kappa^{i-3}$. The ring masses are assumed to all have the same value, 0.5516, so $\mu_i = 1$, the black hole has a mass of 51.16, and $M_d/M_{bh} = 0.054$. On each curve in Fig. 2.6, the precession rate $\dot{\phi}$ increases with steps of -5×10^{-5} ($\Delta\dot{\phi}/\Omega(r_3) = -1.18 \times 10^{-4}$) starting from a value of -1×10^{-4} (i.e., $\dot{\phi}/\Omega(r_3) =$

-2.4×10^{-4}) at the top. We checked the accuracy of the scaling and of our calculations by computing $-D_i/2A_i$ values for different parameter pairs of the system that should give the same $-D_i/2A_i$ according to equation (2.28). We overlay the results for the first ring and precession speed $\dot{\phi}/\Omega(r_3) = -0.0021$, in the lower panel of Fig. 2.6, zooming into the parameter region $-2.3 < D_1/2A_1 < -1.9$ where the different curves deviate from each other the most. In the worst case, due to the scaling of the ring radii, the deviations of the θ_i's from their values for the original 5 ring system are still less than $1°$. Changes in radii cause the largest deviations from the scaling relation because of the way in which they enter in the quantity D_i (equation 2.27). The scaling results for the other rings are similar.

2.2.7   Stability

In this section we investigate the stability of the precessing equilibrium solutions found above. Hunter & Toomre (1969) proved that isolated thin self-gravitating disks are stable to all $m = 1$ warp perturbations and this carries over to disks embedded in spherical or oblate potentials (e.g. Sparke & Casertano, 1988). We show here that the non-linearly warped precessing disks can be both stable and unstable to general ring-like perturbations. We describe small perturbations of the precessing disk solutions by the linearized equations of motion around equilibrium:

$$
\begin{aligned}
\Delta\dot{\theta}_i &= \frac{\partial^2 T_i}{\partial p_{\theta_i}^2}\Delta p_{\theta_i}, \\
\Delta\dot{\phi}_i &= \frac{\partial^2 T_i}{\partial p_{\phi_i}\partial\theta_i}\Delta\theta_i + \frac{\partial^2 T_i}{\partial p_{\phi_i}^2}\Delta p_{\phi_i}, \\
\Delta\dot{p}_{\theta_i} &= -\frac{\partial^2 T_i}{\partial\theta_i\partial p_{\phi_i}}\Delta p_{\phi_i} - \frac{\partial^2 T_i}{\partial\theta_i^2}\Delta\theta_i - \frac{\partial^2 V_{m,i}}{\partial\theta_i^2}\Delta\theta_i \\
&\quad -\frac{\partial^2 V_{m,i}}{\partial\theta_i\partial\phi_i}\Delta\phi_i - \sum_j \frac{\partial^2 V_{m,i}}{\partial\theta_i\partial\phi_j}\Delta\phi_j - \sum_j \frac{\partial^2 V_{m,i}}{\partial\theta_i\partial\theta_j}\Delta\theta_j, \\
\Delta\dot{p}_{\phi_i} &= -\frac{\partial^2 V_{m,i}}{\partial\phi_i\partial\theta_i}\Delta\theta_i - \frac{\partial^2 V_{m,i}}{\partial\phi_i^2}\Delta\phi_i \\
&\quad -\sum_j \frac{\partial^2 V_{m,i}}{\partial\phi_i\partial\theta_j}\Delta\theta_j - \sum_j \frac{\partial^2 V_{m,i}}{\partial\phi_i\partial\phi_j}\Delta\phi_j.
\end{aligned}
\tag{2.29}
$$

Here T_i and $V_{m,i}$ are the kinetic and potential energy terms in the Hamiltonian (2.7) for ring i, respectively, and the partial derivatives are evaluated at the equilibrium solution ($\theta_i, \phi_i =$ const., $\dot{p}_{\theta_i} = 0, \dot{p}_{\phi_i} = 0$). The kinetic terms in equation (2.29) can be found in the Appendix
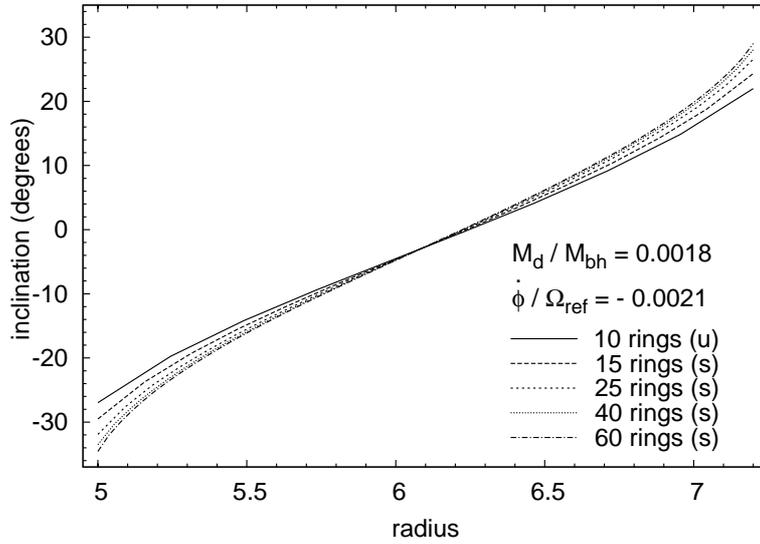
Figure 2.7: Change of the shape of a solution near the lower stable boundary of Fig. 2.4 with the number of rings used to represent the disk. The disk-to-black hole mass ratio, precession speed, and number of rings are given on the plot. The letters "u" and "s" in parentheses following the number of rings stand for unstable and stable solutions respectively.

B. These linear equations have solutions of the form $e^{\lambda t}\Delta\theta_0, \ldots$ etc., where $\lambda = \lambda_{\mathcal{R}} \pm i\lambda_{\mathcal{I}m}$ with its real and imaginary parts. The (constant) coefficients of the Δ terms in equation (2.29) form a matrix H which carries the information on stability. When the real parts of the eigenvalues of the matrix H, $\lambda_{\mathcal{R}} = 0$, the imaginary parts of the eigenvalues, $\lambda_{\mathcal{I}m}$, constitute a rotation matrix through which the solutions oscillate around the precessing equilibrium with frequencies $\lambda_{\mathcal{I}m}$, and the equilibrium is said to be stable. When $\lambda_{\mathcal{R}} < 0$, the solutions spiral towards the unperturbed equilibrium positions, leading to asymptotic stability of the equilibrium. If, however, any of the eigenvalues have a nonzero real part, $\lambda_{\mathcal{R}} > 0$, the system moves away from equilibrium exponentially, and is unstable.

For determining the stability of any of our precessing n-ring solutions, we compute the $4n \times 4n$ stability matrix H, using the equilibrium $(\theta_i, \phi_i = \text{const.}, \dot{p}_{\theta_i} = 0, \dot{p}_{\phi_i} = 0)$. We then evaluate the eigenvalues of the matrix H, using routine F02EBF of the Numerical Algorithms Group (NAG). This routine is suitable for computing eigenvalues and optionally eigenvectors of real matrices.

First, we briefly discuss one example for the convergence of the linear stability results. In Section 2.2.5 we had already discussed the convergence of the gravitational torques, and of the inclination angles obtained for the precessing equilibrium solutions, as a function of the number of rings used to represent the disk (see Fig. 2.5). Figure 2.7 shows how the shape of a
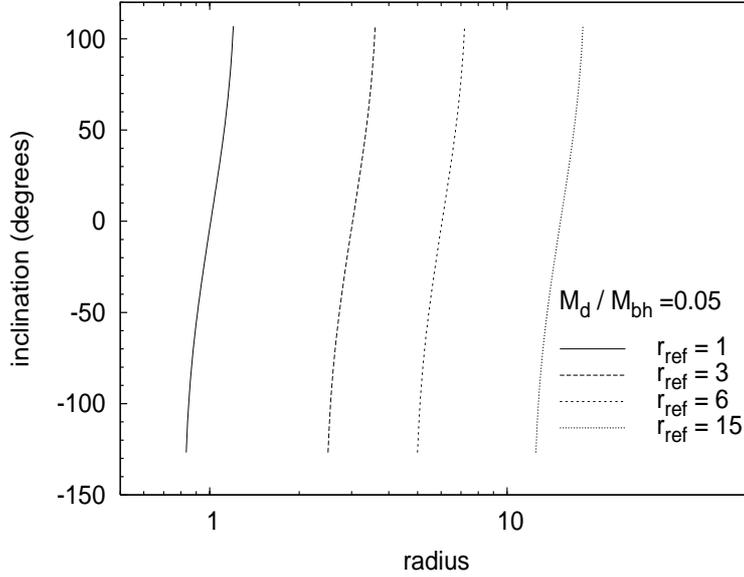
Figure 2.8: 35-ring-disks with constant $M_d/M_{bh} = 0.05$ but different sizes. The curves from left to right show warped disk solutions for which the scale radius r_{ref} is shifted to ever higher values while correspondingly $\dot{\phi}$ is decreased to keep $\dot{\phi}\sqrt{r_{\mathrm{ref}}^3}$ fixed. The innermost and outermost ring inclinations are identical for all disks, as expected from the scaling relation, and all rescaled disks are found to be stable.

solution near the lower stable boundary of Fig. 2.4 and its stability changes with the number of rings used to represent the disk. The transition from unstable to stable occurs at a disk mass fraction of $M_d/M_{bh} = 0.0018, 0.0013, 0.0011, 0.0011$ for $n = 15, 25, 45, 75$ rings. This shows that the transition has approximately converged when $n \simeq 45$.

Next, we consider the issue of scaling. We have already seen that the equilibrium solutions can be scaled in radius, mass, and precession speed according to the approximate (but accurate) scaling relation (2.28): the angles θ_i for all rings in the disk remain unchanged if the precession speed expressed in units of the angular frequency scales linearly with the disk-to-black hole mass fraction. Figure 2.8 shows disks with $M_d/M_{bh} = 0.05$ consisting of equal mass rings with constant ratios of all ring radii relative to each other. Keeping the ratio $\dot{\phi}\sqrt{r_{\mathrm{ref}}^3}$ constant, we have moved the midpoints of these disks to various radii. All these configurations are stable, and actually represent a similar warped disk (i.e. innermost and outermost inclinations being the same) at different distances from the black hole.

Figure 2.9 illustrates the stability properties for these disks when the disk mass and precession speed are changed simultaneously. The boundaries of the stable solutions obtained for a fixed disk mass configuration, i.e., a configuration with constant ratios of all ring masses
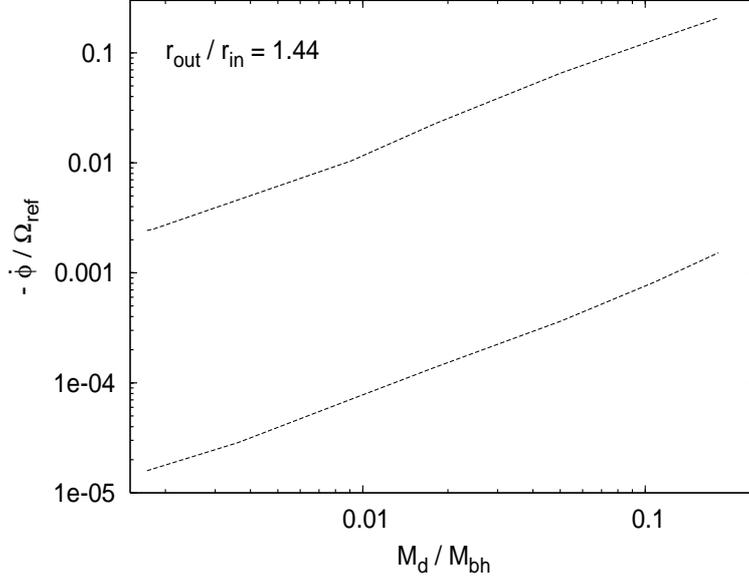
Figure 2.9: Schematic representation of stable warped disk solutions in the M_d/M_{bh} versus $\dot{\phi}/\Omega$ plane. The two inclined dashed lines enclose the stable region: the upper (lower) dashed line corresponds to the maximum (minimum) stable precession frequency at fixed disk-to-black hole mass ratio. This diagram is for disks with the same surface density profile and inner and outer boundaries r_{in}, r_{out}.

and radii relative to each other, are shown by the two dashed lines in the figure. All stable solutions lie between the two lines. These dashed lines are nearly straight, indicating that the minimum and maximum $\dot{\phi}/\Omega_{\mathrm{ref}}$ solutions at different mass fractions can be essentially scaled to eachother - if the same (scaled) equilibrium solution was the stability boundary for all mass ratios, the lines would reflect the scaling relation of eq. (2.27) resp. eq. (2.28) precisely.

Figure 2.9 shows that for each ratio of disk mass to black hole mass, there is a minimum and maximum stable precession speed $\dot{\phi}/\Omega$, and vice-versa. (see Fig. 2.4 and Section 2.3.1 below). The minimum (maximum) stable mass for given $\dot{\phi}/\Omega$ is stable for all precession speeds lower (higher) than the original $\dot{\phi}/\Omega$, until the other boundary curve is reached. For other disk mass configurations, the range of stable mass ratios and the corresponding boundary lines change, but the qualitative behavior remains the same.
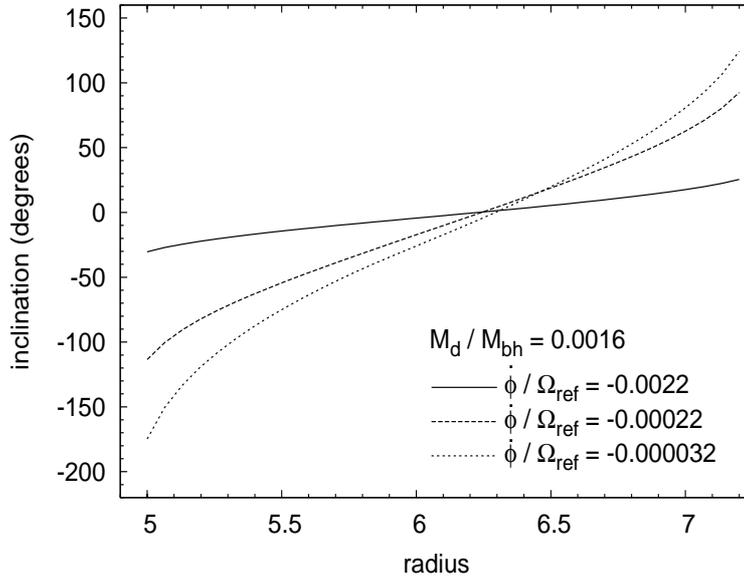
Figure 2.10: Inclination of a disk of 35 rings at different radii for $M_d/M_{bh} = 0.0016$. On each curve the precession frequency $\dot\phi$ has a different value, given on the figure in terms of the orbital frequency at the position of the middle ring. The upper and lower curves show the boundaries of stable solutions. See Section 2.2.7 and Fig. 2.9.

2.3   Steadily Precessing, Non-linearly Warped Keplerian Disks: Results

2.3.1   Warp Shapes and Warp Angles of Stable Precessing Disks

We have already seen in the discussion of three-ring and n-ring systems in Section 2.2 that self-gravitating precessing disks in a Keplerian potential can be strongly warped. In fact, some of the disks shown in Fig. 2.4 are so strongly warped that they would obscure the central black hole from most lines-of-sight.

In this section we discuss these results in more detail. Figure 2.10 shows the warped stable equilibrium solutions obtained for a sequence of disks with varying precession frequency. These disks have constant surface density between fixed inner and outer radii, and a total disk-to-black hole mass ratio of $M_d = 0.0016 M_{bh}$. The solutions shown in Fig. 2.10 are all linearly stable, according to the analysis described in Section 2.2.7. Outside the range of models bounded by the upper and lower curves one can find further equilibria, but these are unstable.

By construction, these disks have a fixed line-of-nodes at all radii, and their shapes are
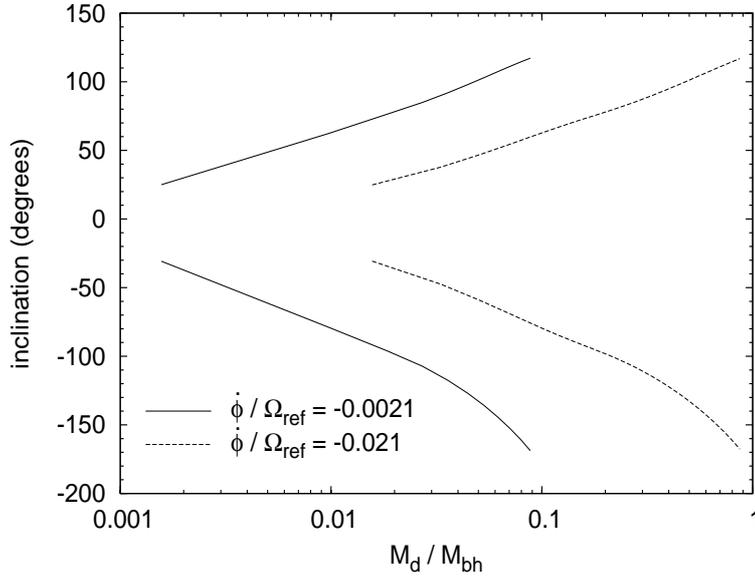
Figure 2.11: Variation with disk-to-black hole mass ratio of the inclinations of the outermost ($\theta > 0$) and innermost ($\theta < 0$) rings of a 35-ring warped disk with $r_{\rm out}/r_{\rm in} = 1.44$, for two different values of the precession frequency. The figure shows how the warping increases with increasing disk mass fraction and with decreasing precession speed, and also illustrates the scaling relation of equation (2.28). Up to numerical errors, the minimum and maximum values of θ are the same on all two curves.

given in terms of the inclination angle θ relative to the plane defined by the total angular momentum vector. In all cases there is a middle section of the disk which lies approximately in this plane, whereas the inner and outer parts warp away from this plane in opposite directions. For the most strongly warped stable solution in Fig. 2.10 the inner warp is by $\sim 180°$ and the outer warp by $\sim 120°$. This is obtained for the lowest stable pattern speed, in accordance with the balance between gravitational and Coriolis torques [see Fig. 2.1 and equation (2.19)]: the torques are weakest for the large inclinations. This can be seen already in the two-ring problem [see equations (2.20) and (2.22)]. The least strongly warped disk solution in this example has inner and outer warps $\sim 25 - 30°$.

The variation of the maximum inner and outer warp angles with disk mass fraction is shown in Figure 2.11 for fixed precession frequency and radial extent of the disk. The curves with $\theta > 0$ represent the outermost ring inclinations, and those with $\theta < 0$ show the innermost ring inclinations for different precession speeds. As we have already seen in Figs. 2.4, 2.10, these inclinations increase with increasing disk mass fraction and with decreasing precession speed. Fig. 2.11 also illustrates the scaling relation of equation (2.28). Up to numerical errors, the different curves can be scaled on top of each other.

Some three-dimensional illustrations of warped disks from this family are shown in Figure 2.12. From top to bottom, these plots shows warped disks with increasing amplitude of the warp, such that the disk in the bottom panel of Fig. 2.12 completely encloses the central black hole.
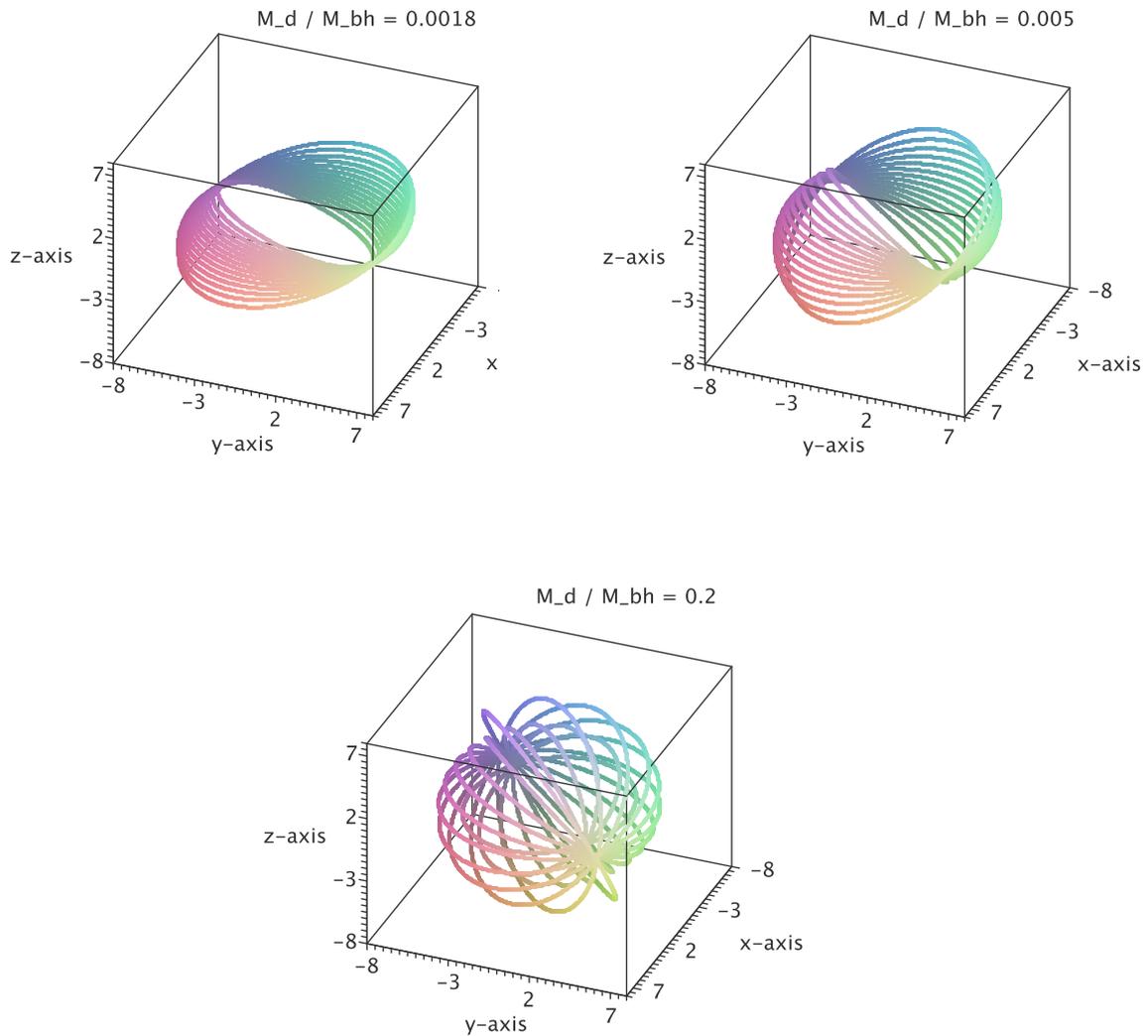

Figure 2.12: Three-dimensional views of several 15-ring disks similar to those shown in Fig. 2.4, with mass ratios given on the plots. The degree of warping increases with the disk mass fraction until (for disk mass fraction greater than 2 percent) the central black hole is completely hidden behind the warped disk.

2.4 Comparison with Linear Theory Solutions

Previous work on warped and twisted disks around black holes has often made use of the linear approximation, in which the inclination angles of all parts of the warped disk are assumed to be small. It is therefore interesting to briefly consider the linear limit of our analysis above.

For small warping angles α_{ij}, the self-gravity torques simplify considerably. Because the leading term in equation (2.13a) is already $O(\alpha_{ij})$, only the $O(1)$ part of the I_{ij} terms in this equation need to be included, while the next order, $O(\alpha_{ij}^2)$, can be neglected. Thus in computing I_{ij} the k^2 term for ring j in equation (2.10) can be approximated as:

$$k_{ij}^2 \approx \frac{4r_i r_j}{(r_i + r_j)^2} \tag{2.30}$$

and the I_{ij} term can be integrated to give

$$I_{ij} \approx \frac{1}{\pi} \left[\frac{E(k_{ij})(1 - k_{ij}^2/2)}{1 - k_{ij}^2} - K(k_{ij}) \right] \frac{(1 - k_{ij}^2/2)^{3/2}}{k_{ij}^2}. \tag{2.31}$$

The mutual torque on ring i from ring j becomes, to first order in α_{ij},

$$\frac{\partial V_{ij}}{\partial \theta_i} = \frac{\partial V_{ij}}{\partial \alpha_{ij}} \frac{\partial \alpha_{ij}}{\partial \theta_i} \approx \frac{2Gm_i m_j r_i r_j I_{ij} \alpha_{ij}}{(r_i + r_j)^{3/2}} \frac{\partial \alpha_{ij}}{\partial \theta_i}. \tag{2.32}$$

For a precessing equilibrium when $\phi_i = \phi_j$, $\alpha_{ij} = \theta_i - \theta_j$, the equation $\dot{p}_{\theta_i} = 0$ becomes to $O(\theta)$:

$$\dot{p}_{\theta_i} = \dot{\phi}^2 \frac{m_i r_i^2}{2} \theta_i - \dot{\phi} p_{\psi_i} \theta_i - \sum_{j=1}^{n} \frac{2Gm_i m_j r_i r_j I_{ij} (\theta_i - \theta_j)}{(r_i^2 + r_j^2)^{3/2}} = 0. \tag{2.33}$$

Equation (2.33) is a quadratic eigenvalue problem for the precession frequencies with the following form:

$$Q(\lambda) = (\lambda^2 M + \lambda C + K)x = 0. \tag{2.34}$$

In order to solve equations like (2.34), one first makes a linearization. This can be done by substituting $u = \lambda x$, in which case equation (2.34) becomes $\lambda M u + \lambda C + K x = 0$, and can be written as the generalized eigenvalue problem (GEP) (Tisseur & Meerbergen, 2001):

$$
\begin{bmatrix} uI - \lambda xI \\ -Kx - Cu - \lambda Mu \end{bmatrix} = \begin{bmatrix} 0 & I \\ -K & -C \end{bmatrix} \begin{bmatrix} x \\ u \end{bmatrix} - \lambda \begin{bmatrix} I & 0 \\ 0 & M \end{bmatrix} \begin{bmatrix} x \\ u \end{bmatrix} = 0. \quad (2.35)
$$

Here, I is the $n \times n$ unitary matrix, n being the number of rings, and the matrices M, C and K follow from equation (2.33). As can be seen from the matrix equation (2.35), the transformation doubles the size of the original matrix. The $2n$ eigenvalues correspond to the precession frequencies, and their associated eigenvectors $[\theta_i, \dot{\phi}\theta_i]$ give the shape of the warp.

We use the NAG routine F02BJF to find the eigenvalues and eigenvectors of equation (2.35).

The $2n$ eigenvalues constitute two distinct families in the frequency spectrum of the disk; the fast prograde, and the slow retrograde frequencies (Hunter & Toomre, 1969). In figure (2.13) we show the full spectrum of precession frequencies for a disk of 35 rings with $M_d/M_{bh} = 0.005$, and $r_{\rm out}/r_{\rm in} = 1.44$. The frequencies are normalized to the orbital frequency at the position of the reference (middle) ring. The dashed line separates the prograde and retrograde families.
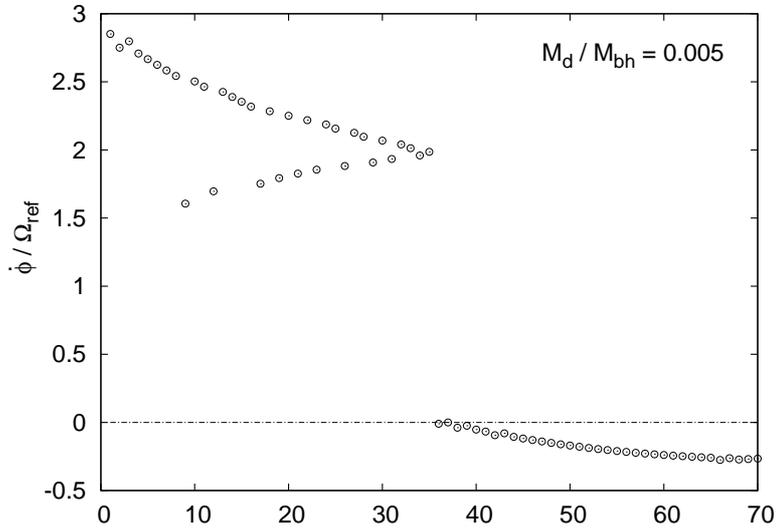
Figure 2.13: Full spectrum of precession frequencies for a disk with $M_d/M_{bh} = 0.005$, and $r_{\rm out}/r_{\rm in} = 1.44$. The precession frequencies are normalized to the orbital frequency at the position of the reference (middle) ring. The dashed line separates the prograde and retrograde families.

To our interest are the disks precessing retrograde with respect to the direction of the orbital motion. Figure (2.14) shows a zoom into this region of the spectrum.
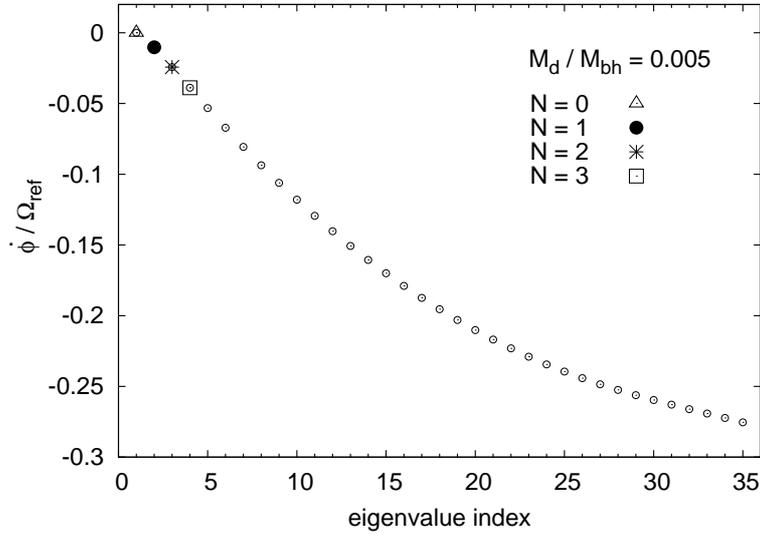
Figure 2.14: Normalized retrograde precession frequencies sorted in decreasing order for a disk consisting of 35 rings with $M_d/M_{bh} = 0.005$, and $r_{\rm out}/r_{\rm in} = 1.44$. First few frequencies are shown with different symbols. They correspond to $N = 0$ (triangle), $N = 1$ (filled circle), $N = 2$ (star), and $N = 3$ (square) modes of the disk.

When sorted in decreasing order, the first retrograde frequency shown by the triangle symbol has a value of zero, and its associated eigenvector represents a rigid tilt of the whole disk by a constant angle, i.e. $\theta_i = {\rm constant}$. This is the so-called rigid tilt mode of the disk. The next eigenvalue corresponds to the warp shapes we have discussed so far, where the disk has one radial node, i.e. $N = 1$ (Hunter & Toomre, 1969; Sparke, 1984; Sparke & Casertano, 1988). This is shown with the filled circle in figure (2.14), while the star and the square symbols correspond to the $N = 2$, and $N = 3$ modes respectively. In figure (2.15) we show these mode shapes for the same disk parameters. In the following, we restrict our discussion to linear warp shapes of the kind $N = 1$. In Figure 2.16 we show the modified tilt mode in linear theory of a disk with $M_d/M_{bh} = 0.005$, $r_{\rm in} = 5$ and $r_{\rm out} = 7.2$ for 40 rings. This is obtained by solving equation (2.33) and is shown with the dashed line. We note that in linear theory the warp shape can be arbitrarily scaled as long as the local gradient of the tilt satisfies $d\theta/dR < 1.2/R$ (see Section (2.2.2)); if this condition is violated, the linear approximation to the self-gravity torques breaks down. Therefore in Fig. 2.16 the linear mode is scaled to its maximum possible amplitude such that the condition is everywhere satisfied. As mentioned above, the precession frequency of this mode is the first nontrivial eigenvalue in the retrograde family, and here it has a value of $\dot{\phi}/\Omega_{\rm ref} = -0.0103$ when normalized to the rotation frequency of the reference ring. For this frequency, we then solve equation (2.5a) to
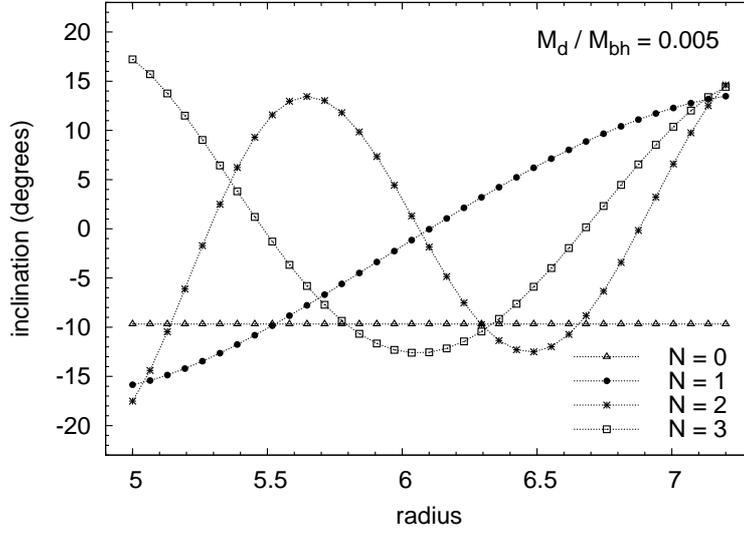
Figure 2.15: Different mode shapes for a disk of 35 rings with $M_d/M_{bh} = 0.005$, and $r_{\text{out}}/r_{\text{in}} = 1.44$. The $N = 0$ mode shown by with the triangle symbol is a simple tilt of the disk where all the rings have are at the same inclination. $N = 1$ mode shown with the filled circle contains a single node in the radial direction. Higher order shapes are depicted with the star and the square symbols for $N = 2$, and $N = 3$ respectively.

obtain the nonlinear warp shape shown by the solid line in Figure 2.16. The larger curvature of the non-linear warp near the inner and outer boundaries of the disk, with respect to the scaled linear mode, shows that the linear approximation overestimates the torques in these parts of the disk.

However, the main difference between linear modes and non-linear warps is that, for a given mass distribution of the disk (surface density profile, inner and outer boundaries), the precession frequency and shape of the modified tilt mode in linear theory is uniquely determined, whereas non-linear equilibrium warp solutions may exist for a range of precession frequencies and warp shapes or, e.g., for extended disks, may not exist at all. For the case shown in Fig. 2.16, non-linear warped equilibria are found for precession frequencies in the range $\dot{\phi}/\Omega_{\text{ref}} = -8.87 \times 10^{-5} \rightarrow -1.16 \times 10^{-2}$ and are stable in the range $\dot{\phi}/\Omega_{\text{ref}} = -9.24 \times 10^{-5} \rightarrow -9.63 \times 10^{-3}$. The particular non-linear warp shape obtained for the frequency of the linear mode and shown in Fig. 2.16 is unstable.

Alternatively, the warp shape may be parameterized by the inclination of the outermost ring, say, θ_n. Linear theory warps can in the previous example be considered valid up to $\theta_n \simeq 10°$, and have all the same precession frequency. Non-linear warp modes are found in the range $\theta_n = 19.1° \rightarrow 130°$, and are stable in the range $\theta_n = 20.9° \rightarrow 129°$. They are
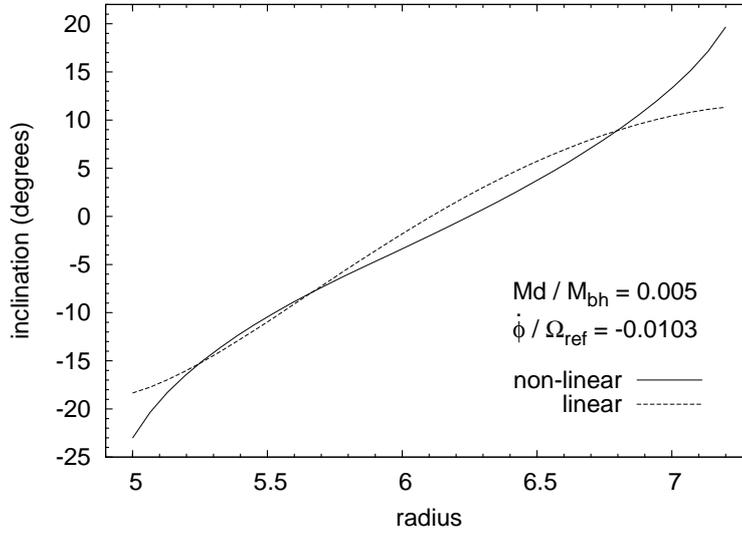
Figure 2.16: Warp shapes for a disk with $M_d/M_{bh} = 0.005$ as obtained in the linear (dashed line), and nonlinear (solid line) torques regimes, for the same precession speed. The linear mode is scaled to the maximal amplitude for which the linear approximation to the gravitational torques can be used. The non-linear disk shape is determined for the precession frequency given by the eigenvalue of the linear mode; it is unstable. Stable non-linear warps for this mass configuration have lower precession speeds and are more strongly warped than the solution shown.

disjunct in θ_n from the linear modes, and their precession speed decreases with θ_n according to the balance of gravitational and Coriolis torques.

2.4.1 Dependence on Surface Density Profile and Radial Extent

The warped disks presented in Figs. 2.4, 2.11 have constant surface density. For comparison, Figure 2.17 shows the warping of an exponential disk, with surface density $\Sigma(r) = \Sigma_0 \exp(-r/r_d)$ where Σ_0 denotes the central density and r_d is the scale length, chosen to be 2.5 units in this example. The other parameters (relative ring radii, precession speed) are identical to those used in Fig. 2.4. The basic warp shapes are similar as for constant surface density, but the maximum outer warp angles are slightly larger. The range of stable disk masses is also comparable to that for the constant surface density disk (for the same precession speed); see the curves showing the boundaries of stability in Figs. 2.4, 2.17.

Because the condition for a warped equilibrium is that the Coriolis and gravitational torques balance, clearly not only the mass fraction and mass distribution, but also the radial extent of the disk must be important for determining the warp shape and its stability. To
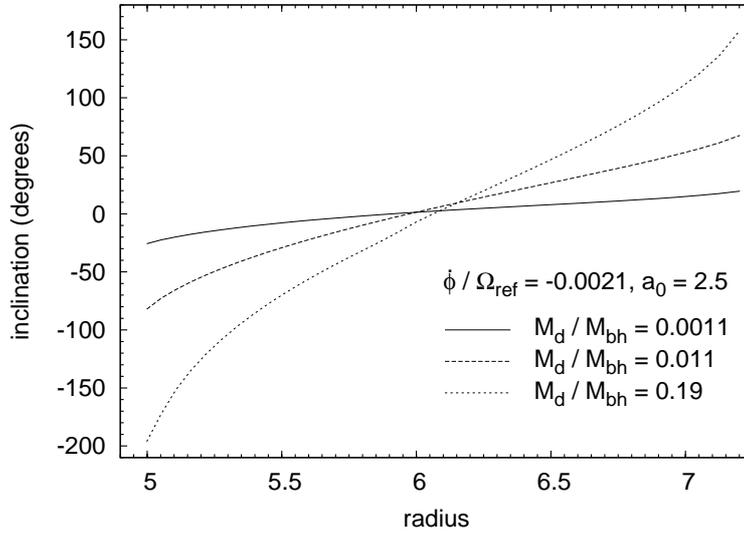
Figure 2.17: Inclination of a 35-ring-disk at different radii as in Figure 2.4, but for an exponential surface density profile with scale length $r_d = 2.5$. The precession speed is identical to that in Fig. 2.4. The upper and lower curves correspond to the limiting mass ratios for disk stability; see Section 2.2.7.
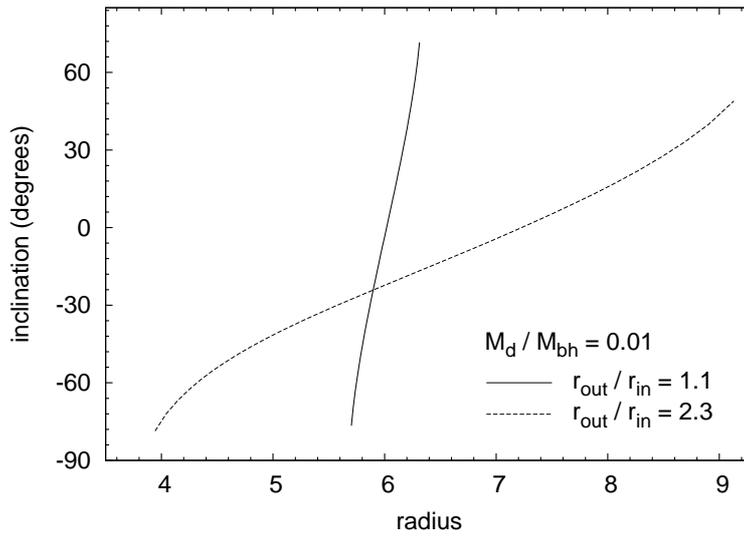

Figure 2.18: Stable warped equilibria for 35-ring-disks with constant surface density but varying radial extent, and with $M_d = 0.01 M_{bh}$. The solid and dashed lines demarcate the boundaries of the region of stable solutions.
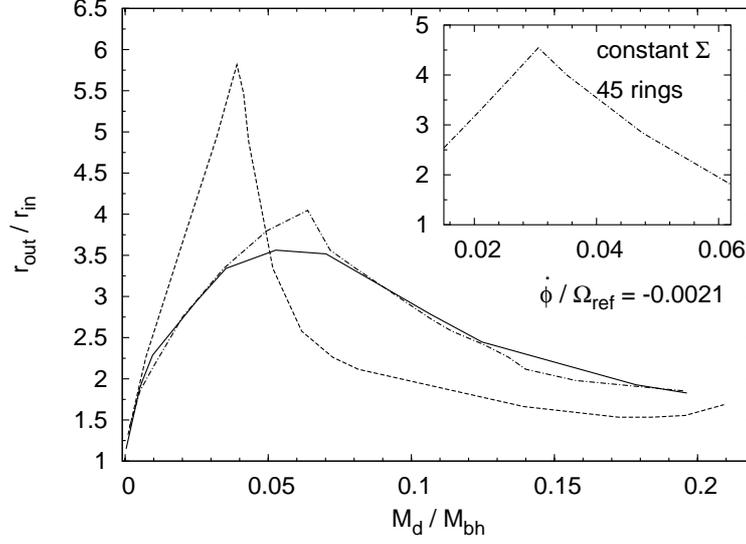
Figure 2.19: Maximum radial extent of stable warped disk equilibria $r_{\mathrm{out}}/r_{\mathrm{in}}$, as a function of disk-to-black hole mass ratio. The dashed line represents the result for a disk of 15 rings with constant surface density, the solid line is for an exponential disk with scale-length $r_d = 5.2$, and the dot-dashed line is for an exponential disk with scale-length $r_d = 2.5$. The inset shows results obtained for the constant surface density disks when instead approximated by 45 rings, near the mass ratio with maximum $r_{\mathrm{out}}/r_{\mathrm{in}}$. Typical ratios are $r_{\mathrm{out}}/r_{\mathrm{in}} =$2-4.

investigate this we compiled a set of precessing equilibria with varying radius scaling factor κ, as follows (see also Section 2.2.5). After fixing the radius of the middle ring of the disk, r_{mid}, we determine the remaining ring radii such that

$$r_i = r_{\mathrm{mid}}\kappa^j \begin{cases} j = i - \frac{n+1}{2} & n \text{ odd} \\ j = i - \frac{n}{2} & n \text{ even} \end{cases} \qquad i = 1, 2, \ldots, n \qquad (2.36)$$

where n is the number of rings. For illustration, we consider a family of disk models with the same disk-to-black hole mass fraction $M_d = 0.01 M_{bh}$, each with its own constant surface density given by M_d and κ. All disks are made of $n = 35$ rings, and the middle ring radius is set to $r_{\mathrm{mid}} = 6$ units.

Figure 2.18 shows precessing equilibria for such disks for different κ. The upper and lower curves show the two disk shapes that bound the stable range of solutions in terms of the κ-factor. In the case where the rings have minimum possible separation from each other, the inner ring has a radius of $r_1 = 5.7$ units, and the outer ring has $r_n = 6.3$ units. On the other hand, for the most extended stable disk in this family, $r_1 = 3.9$, and $r_n = 9.1$. When the extent of the disk is increased, a slight decrease in the warping is observed in Fig. 2.18.

This is due to the fact that the torque from a ring of constant mass decreases with distance to the ring, cf. equation (2.13a).

Figure 2.19 shows the radial extent of the disk $r_{\mathrm{out}}/r_{\mathrm{in}}$ for which stable warped equilibria can be found, for different surface density profiles and as a function of disk-to-black hole mass ratio. The most important result of these calculations is that stable non-linear warps can be maintained only for disks with inner and outer boundaries, for which $r_{\mathrm{out}}/r_{\mathrm{in}} \simeq$ 2-4. This is reminiscent of the result of Hunter & Toomre (1969) that in linear theory only truncated disks permit long-lasting bending modes.

2.4.2   Time-Evolution of Ring Systems

In this section we consider the explicit time-evolution of a precessing system of self-gravitating rings in a massive black hole potential. By integrating the equations of motion, equations (3.21)-(3.24), starting from initial conditions corresponding to one of the precessing disk solutions found earlier, we can check the stability of this solution directly and compare with the linear stability analysis.

In these integrations, we use disks of 20 equal mass rings, equally spaced in radius. The ratio of the outermost ring radius to that of the innermost ring is 1.44. The initial θ_i are obtained from precessing equilibrium solutions; all rings have the same line-of-nodes, i.e., the same initial ϕ_i. The equilibrium precession speed is given by $\dot{\phi}/\Omega_{\mathrm{ref}} = -0.0021$.

In the following figures, symbols starting from the outer circle show the variation of inclination θ with ring radius, where the ring radii are shown as distances from the center of the plot, with scale shown on the lower right. The symbols starting from the inner circle show how the azimuthal angle ϕ changes with the ring radius; for this part of the plot, the ring radii are scaled down to the half of their values to make the figure more easily readable. The elapsed time of the integration is shown on top of the figures, in terms of the number of orbital periods at the position of the outermost ring n where $\dot{\phi}/\Omega_n = -0.0027$.

Figure 2.20 shows the time evolution of a disk of 20 rings with $M_d = 0.05 M_{bh}$. The disk stays in equilibrium for 12 orbital periods, consistent with its linear stability. Figure 2.21 shows the evolution of disk of 20 rings with $M_d = 0.1 M_{bh}$. This disk precesses as a unit for 8 orbital periods, but then it starts to break into parts, hence the disk is unstable, as also predicted by linear stability analysis.

To strengthen the agreement between linear stability and time evolution results, we integrate two of these ring systems for longer. Figures 2.22 and 2.23 show the time evolution of
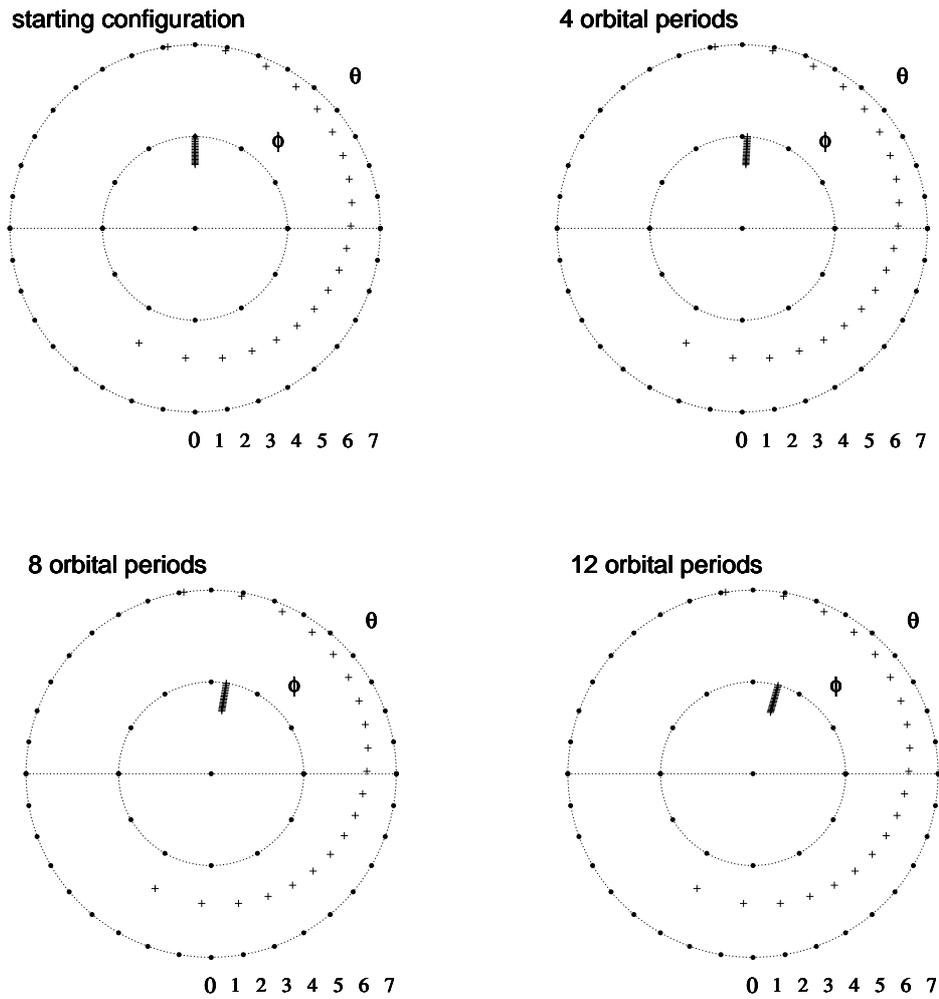
Figure 2.20: Time-evolution of a disk of 20 rings with total mass $M_d = 0.05 M_{bh}$. The disk is stable.
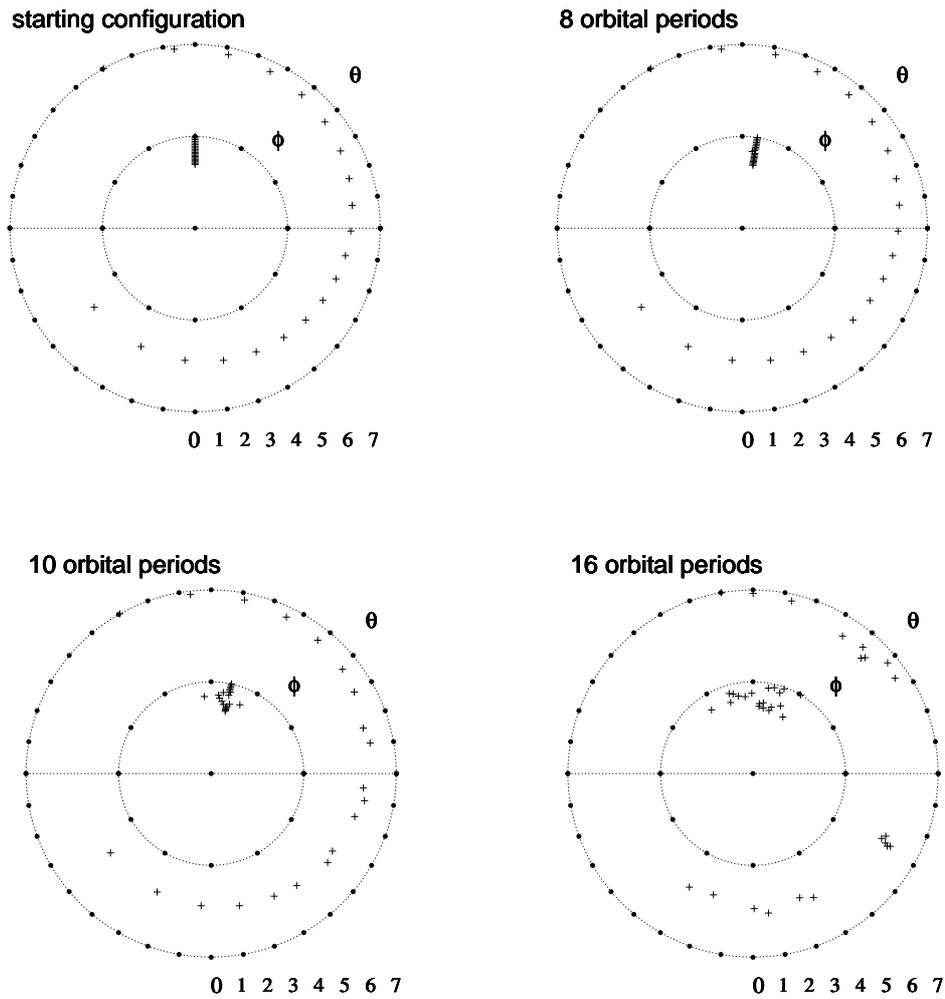
Figure 2.21: Time evolution of a disk of 20 rings with total mass $M_d = 0.1M_{bh}$. The disk precesses as a unit for nearly 8 orbital periods, but then it starts to break up, so is unstable.
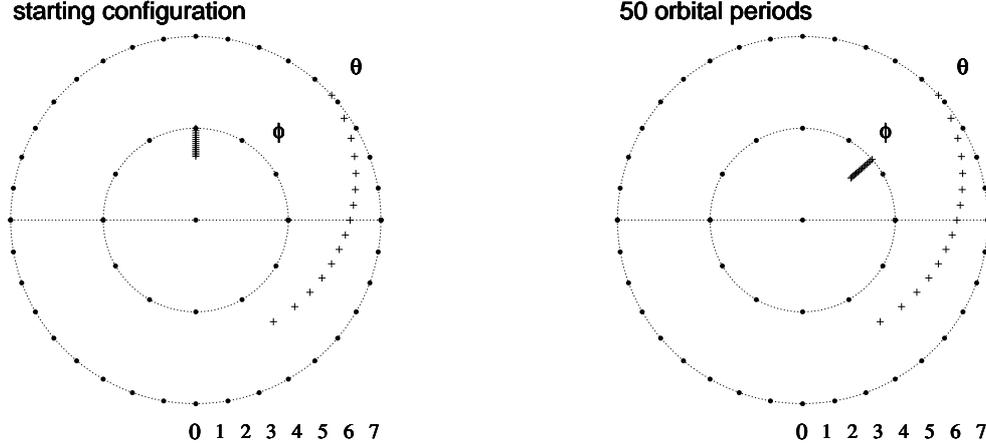
Figure 2.22: Time-evolution of a disk of 15 rings with mass fraction $M_d/M_{bh} = 0.005$. The disk is followed for 50 orbital periods and is stable.

two disks with masses $M_d = 0.005M_{bh}$ and $M_d = 0.02M_{bh}$, with 15 logarithmically spaced rings according to equation (2.36), over 50 orbital periods. In both cases the disks are stable, as expected from the linear stability analysis.

2.5 Discussion

2.5.1 Theoretical Issues

In this work we have considered warped disks around black holes for which the only acting force is gravity and the disk is approximated as a nested sequence of circular rings. We have focussed on non-linearly warped, steadily precessing disk configurations, contrary to most previous work in which small amplitude warps were considered, often of a transient nature. We have found that stable, steadily precessing, highly warped disks can be constructed, albeit only over a limited radial range, such that the typical ratio of the outer to the inner boundary radius is $\sim$ 2-4.

In one illustrative case, we have compared with a linear theory warped disk. For a given disk mass configuration, the precession frequency of the linear, modified tilt mode is given as an eigenvalue, and the shape can be scaled up to the amplitude where the validity of the linear approximation to the gravitational torques breaks down. The corresponding non-linear warp with the same precession frequency is unstable. Stable non-linear warps for the same mass configuration exist for a disjunct range of precession speeds which are all slower than
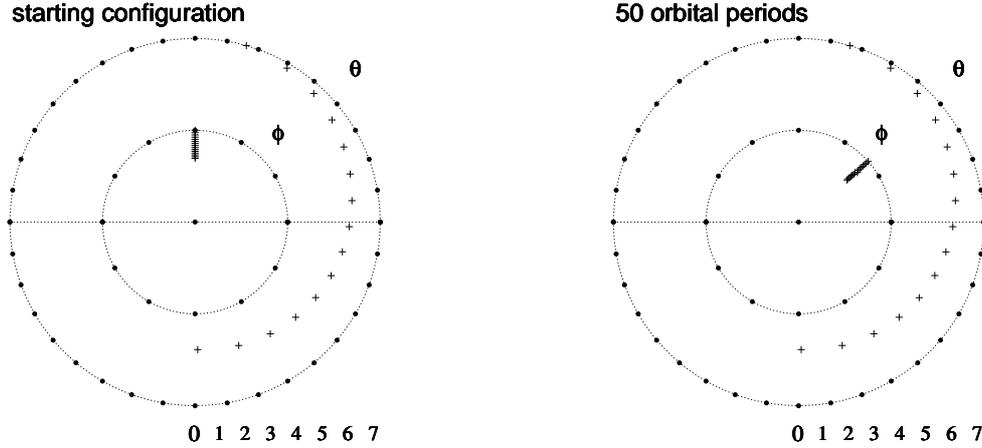
Figure 2.23: Time-evolution of a disk of 15 rings with mass fraction of $M_d/M_{bh} = 0.02$. The evolution is followed for 50 orbital periods and the disk is stable.

that of the linear mode. Their warp angles increase with decreasing precession speed, and the non-linear solutions are more strongly warped than the linear mode at the maximum scaling.

These warped disks obey a scaling relation in the sense that (i) they can be scaled to an arbitrary radius r, provided the precession speed is scaled to the circular frequency $\Omega(r)$, and (ii) they can be scaled in mass, provided the ratio of precession frequency to $\Omega(r)$ keeps in line with the ratio of disk mass to black hole mass.

In constructing these solutions, we have neglected the background potential generated by the surrounding nuclear star cluster, whose quadruple moment will often be important on scales of ~ 0.1 pc. Figure 2.24 shows steadily precessing warped disk inclinations for one case including the background potential. For the parameters chosen, the solutions are qualitatively similar to those discussed earlier.

Stability was tested with respect to perturbations of the ring parameters, that is, the orbits of gas and stars were assumed to remain circular. We did not investigate instabilities by which the disk would become eccentric or lop-sided. Answering the question whether such instabilities are relevant for the warped disks considered here requires different techniques and must remain for future work (see, e.g., Touma, 2002).

Neglecting gas pressure and viscosity for our warped disk solutions is justified if the disks are cold and the viscous time-scale is much longer than the precession time-scale. Pringle (1992) has devised a system of equations for the evolution of the surface density and local angular momentum vector of a non-linearly warped, viscous disk. A logical next step is to add the gravitational torques to these equations and study the evolution of viscous, self-
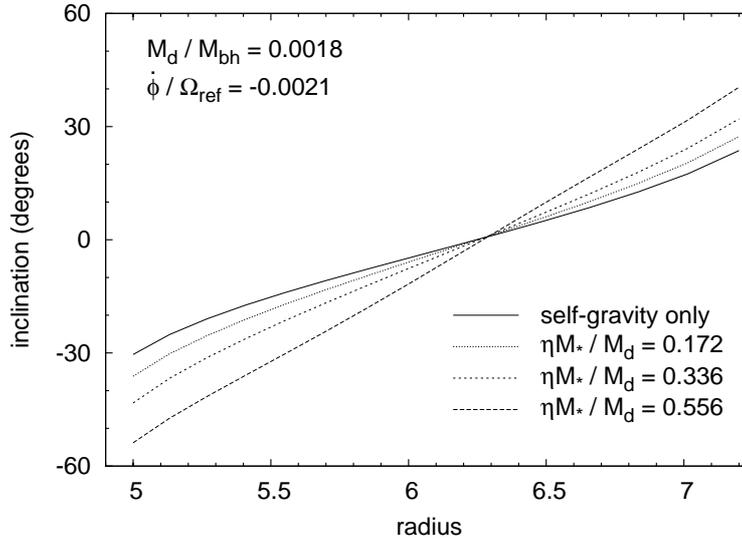
Figure 2.24: Inclination of a disk of constant surface density at different radii, under the self-gravity torques and the quadrupole torques of a surrounding star cluster. This is parameterized by the ratio $\eta M_*/M_d$, where η measures the flattening of the potential (equation (2) of Sparke 1986) and M_*/M_d is the ratio of the mass of the star cluster to the mass of the disk, inside the outermost ring radius.

gravitating, non-linearly warped disks; this is work in progress.

2.5.2 Origin of Warped Disks

An important question is whether, and if so how, the warped nuclear disks we have considered can be set up in nature. Infall of gas clouds on inclined orbits has been discussed in the context of observations of the Galactic center (see next section) as a possible model for generating a warped disk in the central parsec (Hobbs & Nayakshin, 2009). If the potential of the nuclear star cluster is important, accretion of gas onto a plane inclined relative to its principal plane may lead to a warped disk. The combined quadrupole moment of the gas disk itself and of the background cluster potential would cause the orbits to precess and the disk to become warped. In both cases, the accreting gaseous material with misaligned angular momenta will not directly end up in a warped disk with the right density structure for steady state precession. However, the disk may settle into a warp mode if the energy associated with the transient response can be transported outwards by bending waves (Toomre, 1983; Hofner & Sparke, 1994), or in the case of gaseous disks, if it can be dissipated (see discussion in Papaloizou et al., 1998); this remains to be investigated.

Caproni et al. (2006b) discuss four warping mechanisms for extragalactic accretion disks: tidal, irradiative, magnetic, and Bardeen-Petterson. If a planar disk has become warped by the radiation pressure instability discussed by Petterson (1977); Pringle (1996) or through magnetic instabilities (Lai, 2003), the gravitational torques might start to dominate once the source of the initial warping disappears. Highly warped disks have been reported before by Pringle (1997) in the context of the radiation pressure instability. We have done some simple time evolution calculations to show that initially highly warped disks often do not dissolve through self-gravity precession; the torques then cause wobbling but not break-up of the disk. The role of self-gravity in such models would be to ensure the long term persistence of the warp. Future work along the lines discussed at the end of the last subsection may be able to clarify whether this is feasible.

2.5.3 Warped Disks in Galactic Nuclei

Warped disks around central black holes have been inferred through observations of water maser emission in several nearby active galaxies such as NGC 4258, NGC 1068, and the Circinus galaxy. The maser disks in these galaxies extend radially between $0.16 - 0.28$ pc (Herrnstein et al., 1999), $0.65 - 0.11$ pc (Greenhill & Gwinn, 1997), and $0.11 - 0.4$ pc (Greenhill et al., 2003), respectively. The most widely studied of these maser disks is in NGC 4258, where from the near-Keplerian rotation curve of the high-velocity masers the black hole mass is deduced to be $3.8 \times 10^7 M_\odot$, and the dynamical upper limit to the mass of the disk is $< 10^6 M_\odot$ (Herrnstein et al., 2005). Stationary, power-law accretion disk models constrained by theory and observations have mass fractions $10^{-4} - 10^{-3}$ of the central black hole, in which case the gravitational and viscous torques are comparable (Caproni et al., 2007; Martin, 2008). Several explanations have been suggested for the observed warp in the disk (Caproni et al., 2006b). In one model the warp is caused by a binary companion orbiting outside the disk (Papaloizou et al., 1998); this would need a mass comparable to that of the disk. A second possibility is radiation pressure from the central source (Pringle, 1996; Maloney et al., 1996), but Caproni et al. (2006b) analyzing several AGN disks find that these are stable against radiation warping. The most favored explanation for the warp is the Bardeen-Petterson effect (Caproni et al., 2007; Martin, 2008) but to reach a steady state the disk must be very long-lived. Gravitational torques have so far been mostly neglected; our results suggest that it may be worthwhile to consider models including both the gravity from the disk and possibly the quadrupole moment of the stellar cusp.

In the Galactic center, NIR observations have identified one or possibly two disks of young stars at a distance of ~ 0.04 to 0.4 pc from the central black hole SgrA* (Genzel et al., 2003; Paumard et al., 2006; Lu et al., 2009; Bartko et al., 2009). These stellar disks are highly inclined both with respect to the Galactic plane, and with respect to each other. The total mass in the disks, as inferred from stellar number counts, is around 10^4 M$_\odot$ (Paumard et al., 2006). This is a non-negligible fraction of the mass of SgrA*, $M_{\rm bh} \sim 4 \times 10^6$ M$_\odot$ (Genzel et al., 2000; Ghez et al., 2005). The recent analysis of Bartko et al. (2009) shows that the clockwise rotating disk is warped, with angular momentum direction slewing over $\sim 60°$ from the inner to the outer stars. We consider the precession of the warped disk in the Galactic center elsewhere.

Warped disks could also have important implications for the unification of AGN (Phinney, 1989). The unification theories rely on the obscuration along some lines-of-sight of the radiation from the central source by intervening matter. While this obscuring matter is usually depicted as a doughnut-like torus, an alternative possibility is that it could have the shape of a flared or warped disk. The highly warped solutions discussed above in principle provide the geometry to obscure the central engine from most lines-of-sight. The obscuring medium required for these unification scenarios must be clumpy (Nenkova et al., 2002), perhaps suggesting fragmentation of the disk (Goodman, 2003). Nayakshin (2005) studied the evolution of a highly inclined warped disk, where he showed that the disk indeed can conceal the central object for most of its lifetime. In the nonlinear regime, warped disks can obscure a significant part of the solid angle of the source (see Figure 2.12 in Section 3.4 above). Recently, Wu et al. (2008) showed that because the outer parts of a warped disk receive a larger fraction of the central emission, the line ratios of the reprocessed Balmer emission lines can be successfully predicted by a warped disk model.

2.6 Summary and Conclusions

In this paper we have investigated non-linearly warped disk solutions around black holes for which the only acting force is gravity. We used a simple model in which the disk is approximated as a nested sequence of circular rings. We have shown that with these approximations stable, steadily precessing, highly warped disks can be constructed.

These disks have a common line-of-nodes for all rings. In all cases there is a middle section of the disk which lies approximately in this plane, whereas the inner and outer parts warp away from this plane in opposite directions. The warp angles of these solutions can be

very large, up to $\sim \pm 120°$, but they extend only over a limited radial range, such that the typical ratio of the outer to the inner boundary radius is $\sim$ 2-4. Such precessing equilibria exist for a wide range of disk-to-black hole mass ratios M_d/M_{bh}, including quite massive disks.

The stability of these precessing disks was determined using linear perturbation theory and, in a few cases, confirmed by numerical integration of the equations of motion. We found that over most of the parameter range investigated, the precessing equilibria are stable, but some are unstable.

These disks obey a scaling relation: they can be scaled to arbitrary radii r, provided the precession speed is scaled to the circular frequency $\Omega(r)$, and they can be scaled in mass, provided the ratio of precession frequency to $\Omega(r)$ is changed, in good approximation, proportionally to the ratio of disk mass to black hole mass.

The main result of this study is that persistent forcing of the disk other than by its own self-gravity is not necessarily required for maintaining a non-linearly warped disk in a Keplerian potential. Further work combining self-gravity with gas physics etc. will show whether these self-gravitating warped disk solutions help to understand the observed warped disks in galactic nuclei.

Chapter 3

On the Origin of Warped Stellar Disks at the Galactic Center

The Galactic Center hosts population of young stars which orbit SgrA* on clockwise and counter clockwise orbits on the plane of the sky. The clockwise orbits form a well defined disk, and a secondary disk of the counter clockwise stars is also becoming pronounced in some of the recent observations. While the formation of stars in the close proximity of the massive black hole is already problematic, their orbital configuration makes the situation even more bizarre.

We present a possible warped disk origin scenario for these stars, which assumes an initially flat accretion disk becoming warped due to a central radiation source via Pringle instability, or due to a spinning black hole via Bardeen-Petterson effect. The young stars form after the disk becomes warped. The warped disk of stars then evolves in the combined potential of the black hole, and the disk self-gravity. We show that the disks with a mass ratio $M_d/M_{bh} > 0.001$ break into two pieces, while below this this limit they remain intact. Comparison of our models with the observations suggest that the configuration of the clockwise disk can be explained by a non-breaking disk, and that the counter rotating disk probably has a different origin.

3.1 Introduction

The center of our Galaxy hosts a supermassive black hole (SMBH), SgrA*, with a mass of $3.95\pm0.06\times10^6\ M_\odot$ (Genzel et al., 2000; Ghez et al., 2005; Trippe et al., 2008; Gillessen et al.,

2009). SgrA* is surrounded by a cluster of old (Schödel et al., 2007; Trippe et al., 2008), as well as a group of young stars (Krabbe et al., 1995; Genzel et al., 2003; Levin & Beloborodov, 2003; Paumard et al., 2006; Lu et al., 2006, 2009; Bartko et al., 2009).

Of the nearly 90 young stars observed at distances ~ 0.05 pc to ~ 0.5 pc, 40 populate a disk (Genzel et al., 2003; Levin & Beloborodov, 2003; Paumard et al., 2006; Lu et al., 2006, 2009; Bartko et al., 2009) which is observed to rotate clockwise (CW) on the plane of sky. Of the rest, 19 stars seem to populate an other disk highly inclined to the CW disk (Genzel et al., 2003; Paumard et al., 2006; Bartko et al., 2009). This second disk is seen to rotate counter clockwise (CCW) on the sky (but also see Lu et al. (2006)). Ages of these young stars are consistent with being a few Myr, suggesting that there has been a star formation episode in the Galactic Center (GC) a few million years ago.

In order for a molecular cloud near a SMBH to fragment into stars, its self-gravity should overcome the tidal field of the black hole. This requirement for star formation poses a constraint on the minimum cloud densities, which are orders of magnitude higher than the observed cloud densities near the GC. However theoretical estimates suggest that the fragmentation conditions are met naturally on the accretion disks which become self-gravitating beyond a few tenth of parsec (Kolykhalov & Syunyaev, 1980; Gammie, 2001; Goodman, 2003). Therefore several numerical simulations have been performed aiming at modeling the in-situ fragmentation of a nuclear/accretion disk for parameters relevant to the GC. The simulations were run either assuming *a priori* a gravitationally unstable accretion disk already in place (Nayakshin et al., 2006; Alexander et al., 2008), or trying to account also for the formation of the disk itself through infall of molecular clouds into the vicinity of the black hole (Bonnell & Rice, 2008; Mapelli et al., 2008; Hobbs & Nayakshin, 2009).

Today it looks like a star forming disk at the GC can be simulated, albeit perhaps for a somewhat fine-tuned parameter range. On the other hand, apart from the problem of youth, another issue still to be addressed is the distribution of the inclinations of the stars. It is reasonable to expect that a planar accretion disk leaves behind a planar distribution of stars when it fragments, but the recent data published by Bartko et al. (2009) provide evidence for a warp in the CW disk with an amplitude of about $60°$ (Bartko et al., 2009). Lu et al. (2009) point out that even though the stars might have formed in-situ, their current orbital distribution suggests a more sophisticated origin than a simple thin accretion disk. Simulations performed by Cuadra et al. (2008) are in line with this idea showing that once the stars form on a cold accretion disk it is not possible to perturb these stars to the high inclinations at which they are observed.

Warped disks, although monitored only through maser emission from gas disks, exist on similar scales in other nearby galactic nuclei such as NGC4258 (Herrnstein et al., 1996), NGC1068 (Greenhill & Gwinn, 1997), and Circinus (Greenhill et al., 2003). An initially planar accretion disk could become warped when torqued by a spinning black hole (Bardeen & Petterson, 1975; Armitage & Natarajan, 1999; Lodato & Pringle, 2007; Martin, 2008), or when exposed to radiation from a central source (Petterson, 1977; Pringle, 1996, 1997). Milosavljević & Loeb (2004) pointed out that the maser nuclei, and the Galactic Center might represent different epochs of a cycle during the lifetime of a typical spiral galaxy.

In this chapter, we develop an alternative scenario for the formation of a star-forming, warped disk at the Galactic Center. According to this scenario, a flat accretion disk forms around SgrA*, extending out to the location of the young stars observed today. During a supposed period of active accretion, the disk is illuminated by the central source, or torqued by a spinning black hole, and becomes warped due to the Pringle instability or the Bardeen-Petterson effect, respectively. When the AGN activity subsides, the disk cools and forms stars. Afterwards, the stellar disk evolves in the gravitational field of the black hole, and its own self-gravity. We investigate under which conditions this scenario could work, and show that with a low mass such as inferred today the remnant warped stellar disk survives for the life-time of the observed young stars, but with significantly higher mass it often breaks into two coherent pieces.

In Section 3.2 we work out the conditions for which the disk would become warped due to the mechanisms mentioned above, and then fragment into stars. In Section 3.3 we describe our model and the numerical scheme for studying the subsequent time evolution of the warped stellar disk. The results of our calculations evolution are presented in Section 3.4, and in Section 3.5 we compare these models with the observations. The results of this chapter are discussed in Section 3.6, and finally in Section 3.7 we list our conclusions.

Before moving on, we list in Table 3.1 some parameters of the Galactic Center and the above mentioned disks. Throughout this chapter, we will assume a mass of $M_{bh} = 4 \times 10^6 M_\odot$ for SgrA*, $r_{\rm in} = 0.06$ pc, and $r_{\rm out} = 0.4$ pc for the inner and outer edges of the disk whenever needed.

3.2 Warping the Galactic Center Disk

In this section, we discuss a plausible scenario of how a disk of young stars in the Galactic Center might have acquired its warped shape. For now we only consider a single disk, refer-

Parameter	Value	References
M_{bh}	$\sim 4 \times 10^6 \; \mathrm{M_\odot}$	Trippe et al. (2008); Gillessen et al. (2009)
L/L_{edd}	$\sim 10^{-9} \; \mathrm{ergs^{-1}}$	Narayan (2002); Baganoff et al. (2003)
r_{in}	$0.06 \; \mathrm{pc}$	Paumard et al. (2006); Bartko et al. (2009)
r_{out}	$0.4 \; \mathrm{pc}$	Paumard et al. (2006); Bartko et al. (2009)
P_{in}	$\sim 690 \; \mathrm{yr}$	
P_{out}	$\sim 1.19 \times 10^4 \; \mathrm{yr}$	
$M_d|_{CW}$	$< 1 \times 10^4 \; \mathrm{M_\odot}$	Nayakshin (2005)
$M_d|_{CCW}$	$< 5 \times 10^3 \; \mathrm{M_\odot}$	Nayakshin (2005)

Table 3.1: Parameters of the nuclear region of the Galaxy and of the stellar disks. r_{in}, and r_{out} are the innermost and outermost radii of the stellar disk, and P_{in}, and P_{out} are the corresponding orbital periods respectively.

ring to the clockwise rotating disk whose warped shape is described in Bartko et al. (2009). We start with the assumption that an accretion disk builds up, leading to an active phase of sub-Eddington accretion onto the Galactic Center black hole. We then investigate two possible mechanisms: radiation pressure instability (Petterson, 1977; Pringle, 1996, 1997) and Bardeen Petterson effect (Bardeen & Petterson, 1975) for warping the accretion disk, which have both been extensively discussed in the context of the maser disks in nearby Seyfert galaxies (Maloney et al., 1996; Scheuer & Feiler, 1996; Pringle, 1997; Armitage & Natarajan, 1999; Lodato & Pringle, 2007; Martin, 2008). We further assume that after some time the accretion and energy production is reduced, following which the warped disk can cool and form stars. Thereafter the stellar disk is only subject to gravity, precessing under the influence of the gravitational torques from the disk itself.

In Section 3.2.1, we constrain the surface density of the disk prior to fragmentation from the observed number density of young stars. In the following subsections 3.2.2 and 3.2.3, we consider in turn warping by the radiation pressure instability and the Bardeen-Petterson effect. In Section 3.2.4, we compare the radiation, viscous, and gravitational torques on the disk, and in Section 3.2.5 we consider fragmentation and star formation.

3.2.1   Surface Density of the Disk Prior to Fragmentation

The warping mechanisms we will shortly be considering in sections (3.2.2) and (3.2.3) are generally studied within the framework of viscous, steady-state accretion disks. As such they make use of a number of parameters which from the observations of the stellar disks can not be tested or constrained. For these, we will mostly refer to the canonical values for AGN

disks when needed. Still, there is one parameter, the surface density of the supposed gaseous disk which may be determined by the observations. To do so we make use of the stellar number counts on the Galactic Center (GC) disks. The total number of stars $N_\star$ in a stellar population can be calculated by writing:

$$N_\star = \int_{M1}^{M2} \xi(M)dM, \tag{3.1}$$

where $\xi(M)$ is the initial mass function, IMF, and M_1 and M_2 are the lowest and highest stellar masses assumed to exist in this population. The IMF describes how the mass is distributed in stars in a newly born population. For a given IMF, the total mass in stars, M_s, is calculated from:

$$M_s = \int_{M1}^{M2} M\xi(M)dM. \tag{3.2}$$

Paumard et al. (2006) deduce from the K-band luminosity function of the observed early type stars an IMF $\xi(M) = \xi_0 M^{-0.85}$ for the GC disks. The Bartko et al. (2009) sample includes 40 stars in the clockwise (CW) disk, and 19 stars in the counter clockwise (CCW) disk. Using equations (3.1) and (3.2), and assuming a lower mass end of $1M_\odot$, and an upper mass end of $120M_\odot$, the current total stellar mass in the disks can be found to be $M_s|_{CW} + M_s|_{CCW} = M_s \sim 4000M_\odot$, where $M_s|_{CW}$, and $M_s|_{CCW}$ are the masses of the CW and CCW rotating disks respectively. The total stellar mass inferred today is a fraction of the mass of the original gaseous disk since presumably not all the gas was converted to stars. Assuming a star formation efficiency ϵ_{SF} the total mass of the seed disk can be calculated. Since the radial extent of the disks is observationally constrained, this mass can be converted into a surface density Σ of the proposed gas disk. The observations of the stellar disks suggest that the mass density decreases nearly as $1/r^2$ (Paumard et al., 2006; Bartko et al., 2009), so we write for the mass M_d and surface density Σ_d of the gaseous disk:

$$M_d = 4000\mu_{4000}\epsilon_{SF}^{-1}M_\odot, \tag{3.3}$$

where $\mu_{4000} = (M_s/4000M_\odot)$ and for $\Sigma_d(r) = \Sigma_{0.1}\hat{r}^{-2}$ we find:

$$\Sigma_{0.1} = 3.356 \times 10^4 \mu_{4000}\epsilon_{SF}^{-1} \frac{M_\odot}{\text{pc}^2} = 7.013\mu_{4000}\epsilon_{SF}^{-1} \frac{\text{g}}{\text{cm}^2}. \tag{3.4}$$

with $\hat{r} \equiv r/0.1\text{pc}$. In Figure 3.1 we show for two star formation efficiencies the surface density of the disk obtained as described above. The solid line assumes $\epsilon_{SF} = 0.01$, and the

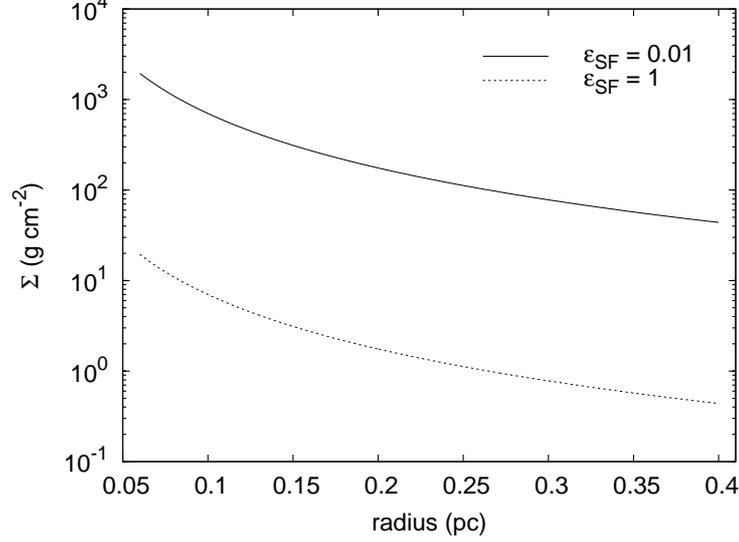dotted line assumes $\epsilon_{SF} = 1$.

Figure 3.1: Surface density of the supposed GC gaseous disk for star formation efficiencies of 0.01 (solid line), and 1 (dotted line).

3.2.2   Radiation Driven Warping and the Galactic Center Disk

Radiation warping of accretion disks is studied in detail by many authors (Pringle, 1996; Maloney et al., 1996; Pringle, 1997; Ogilvie & Dubus, 2001). When an optically thick is exposed to central radiation, and it re-emits the absorbed incident photons parallel to the disk local normal, an inward directed force is experienced by each side of the disk. If the disk is slightly distorted, a net torque is induced which results in a modification of the warp, and precession of the disk around the total angular momentum direction. Whether the disk will acquire a pronounced warp or not, depends on the competition between the net torque, and the component of the stress in the $r - z$ direction in cylindrical symmetry, present in warped disks. The latter forces the disk to settle onto a plane on an alignment time-scale. The alignment time scale at distance r from the black hole is associated with the $r - z$ stress, and can be written as $t_{\nu_2} = 2r^2/\nu_2$, where ν_2 is the vertical viscosity coefficient. The condition that the warp growth time scale, t_{warp}, be smaller than the viscous time scale, t_{ν_2} is written as (Pringle, 1997):

$$\frac{12\pi\Sigma r^3 \Omega c}{L} \leq \frac{2r^2}{\nu_2}, \tag{3.5}$$

where, L is the luminosity of the central source, c is the speed of light, and α is the Shakura-Sunyaev parameter (Shakura & Syunyaev, 1973). Equation (3.5) assumes an accretion disk which is in steady state. For such disks, the luminosity of the disk L is related to the radiative efficiency $\epsilon \equiv L/\dot{M}c^2$, where $\dot{M}$ is the mass accretion given by $\dot{M} = 3\pi\Sigma\nu_1$, and ν_1 is the radial viscosity coefficient. In order to evaluate the warping criterion given in (3.5) one has to estimate the magnitude of the vertical viscosity ν_2. Previous studies of linear hydrodynamic warps and magnetized shearing box simulations of accretion disks showed that $\eta_\nu = \nu_2/\nu_1 = 1/2\alpha^2$ (Papaloizou & Pringle, 1983; Ogilvie, 1999; Torkelsson et al., 2000). Lodato & Pringle (2007) find with SPH simulations of small and large-amplitude warps that the vertical viscosity saturates for small α such that $\eta_\nu < 3.5\alpha$. Using these, the warp damping time scale becomes:

$$t_{\nu_2} = \frac{2r^2}{\nu_2} \simeq \left(\frac{\alpha}{3.5}\right)\frac{2r^2}{\nu_1} \approx 2 \times 10^5 \frac{\alpha\mu_{4000}\epsilon}{\epsilon_{\mathrm{SF}}\eta_{\mathrm{edd}}}\mathrm{yr}, \tag{3.6}$$

where $\eta_{\mathrm{edd}} \equiv L/L_{\mathrm{edd}}$. Equation 3.5 can now be rearranged to give the radiation warping critical radius:

$$R_{\mathrm{rad}} > \frac{2\eta_\nu^2}{\gamma_{\mathrm{crit}}^2\epsilon^2}\frac{2GM}{c^2}, \tag{3.7}$$

where $\gamma_{\mathrm{crit}} \simeq 0.32$ (Pringle, 1997). One way to obtain a stronger torque is if the irradiation of the disk is driving an outflow (Schandl & Meyer, 1994). In this case, the torque is determined by the outflow momentum or pressure at the sonic point, which is basically $\propto L$, but also depends on the detailed disk structure in a complicated way. The enhancement of the torque could be significant, as the ratio of momentum to energy for particles may be much larger than for photons. Although a gross over simplification, we may parameterize this by an additional (not constant) multiplicative factor F_{wind} on the radiation torque, so that the warping criterion become:

$$R_{\mathrm{rad}} > \frac{2\eta_\nu^2}{\gamma_{\mathrm{crit}}^2\epsilon^2 F_{\mathrm{wind}}^2}\frac{2GM}{c^2} = 9.1 \times 10^{-3}\alpha^{-2}\epsilon_{0.1}^{-2}F_{\mathrm{wind}}^{-2} \mathrm{pc} \tag{3.8}$$

where for the numerical value we have used $\gamma_{\mathrm{crit}} \simeq 0.32$, $\epsilon = 0.1\epsilon_{0.1}$ and $\eta_\nu \simeq 3.5/\alpha$ (Lodato & Pringle, 2007). Thus warping the disk in the radial range of the Galactic Center (0.06-0.4pc) requires $\alpha \sim 0.3$, or $\alpha \sim 0.1$ and radiatively efficient accretion by a rotating black hole or modest enhancement of the torque by a disk wind.

3.2.3 Bardeen Petterson Effect and the Galactic Center Stellar Disk

In this section, we show under which conditions the Galactic Center disk might have been warped due to Bardeen Petterson effect.

An accretion disk forming around a rotating (Kerr) black hole might initially have a total angular momentum misaligned with that of the black hole. Inner portions of the disk close to the black hole experience general relativistic frame dragging which causes a differential precession, the so-called Lense-Thirring precession (Lense & Thirring, 1918). As we have seen in the previous section, the viscous time scale increases with radius, hence the inner parts of the disk are forced to align with the black hole on time scales much shorter than those for the outer parts. Consequently, the disk develops a shape which for $r < R_{\mathrm{BP}}$ is aligned with the black hole, i.e. is flat, and for $r \geq R_{\mathrm{BP}}$ its angular momentum direction changes gradually from radius to radius (Bardeen & Petterson, 1975). Like the radiation pressure warping, the Bardeen Petterson effect also is a competition between the vertical viscous time scale, and the precession time scale (Armitage & Natarajan, 1999). The precession induced by the Bardeen Petterson effect is given by (Kumar & Pringle, 1985):

$$\dot{\phi} = 2ac \left(\frac{GM_{bh}}{c^2} \right)^2 \frac{1}{r^3}, \qquad (3.9)$$

where a is the black hole spin parameter which can take values between 0 and 1 for stationary, and maximally rotating black holes respectively. The precession time scale $\tau_{\mathrm{BP}} = 2\pi/\dot{\phi}$ is:

$$\tau_{\mathrm{BP}} = \frac{\pi c^3 r^3}{a G^2 M_{bh}^2}. \qquad (3.10)$$

The critical radius, where the vertical viscous time scale equals the precession time scale is then obtained writing:

$$\frac{\pi r^3 c^3}{a G^2 M_{bh}^2} = \frac{2r^2}{\nu_2} \rightarrow R_{\mathrm{BP}} = \frac{2a G^2 M_{bh}^2}{\pi c^3 \nu_2}. \qquad (3.11)$$

Using the steady state relations introduced in the previous section equation (3.11) becomes:

$$R_{\mathrm{BP}} = \frac{6a G^2 M_{bh}^2 \epsilon \Sigma(R_{\mathrm{BP}})}{\eta_\nu c L}. \qquad (3.12)$$

In order to estimate the Bardeen Petterson radius for the GC, we need to solve equation (3.12)

for R_{BP}. Writing $\Sigma(R_{\mathrm{BP}}) = \Sigma_0/\hat{r}^{-2}$ we obtain:

$$R_{\mathrm{BP}} = 8.9 \times 10^{-4} \left(\frac{a \epsilon \alpha \mu_{4000}}{\eta_{\mathrm{edd}} \epsilon_{\mathrm{SF}}} \right)^{1/3} \mathrm{pc.} \tag{3.13}$$

This estimate shows that the Bardeen Petterson radius for the GC is quite small, i.e. much below the inner edge of the observed disks. We should remind that the alignment time scale t_{ν_2} for the assumed surface density profile is independent of radius, and is short. This means that the disk can be warped out to large distances since both R_{BP} and t_{ν_2} depend on the disk parameters only weakly.

The angular momentum of the disk at r is $\propto 2\pi\Sigma r dr \sqrt{GM_{bh}r} \propto r^{-1/2}dr$ and varies only slowly with r. The ratio of the disk to black hole angular momenta can thus be estimated as:

$$\frac{J_d}{J_{\mathrm{bh}}} \simeq \frac{M_d\sqrt{GM_{bh}r_d}}{aGM_{bh}^2/c} = \frac{1}{a}\frac{M_d}{M_{bh}}\sqrt{\frac{2r_d}{r_s}} \sim 0.7\epsilon_{\mathrm{SF}}^{-1}a^{-1}, \tag{3.14}$$

where $r_d \sim 0.1\mathrm{pc}$. This suggests that by the time the disk is significantly warped at $r_d \sim 0.1\mathrm{pc}$, the black hole spin should be significantly aligned: the alignment time-scale found by Lodato & Pringle (2006) under similar circumstances is $\sim 0.3t_{\nu_1} \sim 0.3(3.5/\alpha)t_{\nu_2} \sim \alpha^{-1}t_{\nu_2}$. These arguments suggests that if the Galactic Center disk was first warped through the Bardeen-Petterson effect, and then fragmented to form the observed surface density of young stars, the star formation efficiency had to be high, $\epsilon_{\mathrm{SF}} < 1$, to prevent the disk from dominating the angular momentum, and $\alpha < 0.1$ to give the disk time to warp before it is accreted and will align the black hole spin.

3.2.4 Comparison of Gravitational, Viscous and Radiation Torques

In section (3.2.2) we have discussed the conditions for radiation warping. While equation (3.5) has to be satisfied for warping, it is also useful to compare the magnitude of radiation and gravitational torques acting on the disk.

The magnitude of the radiation torque on a ring of radius r with radial width dr can be approximated as (Ogilvie & Dubus, 2001):

$$2\pi r dr T_{\Gamma} \simeq \frac{L}{6cr}r dr, \tag{3.15}$$

thus $T_{\Gamma} = \Sigma r^2 \Omega / t_{\Gamma}$ (more details on the radiation torque can be found in Appendix C). On the other hand the viscous torque on the ring, which tries to damp the warp in the case of
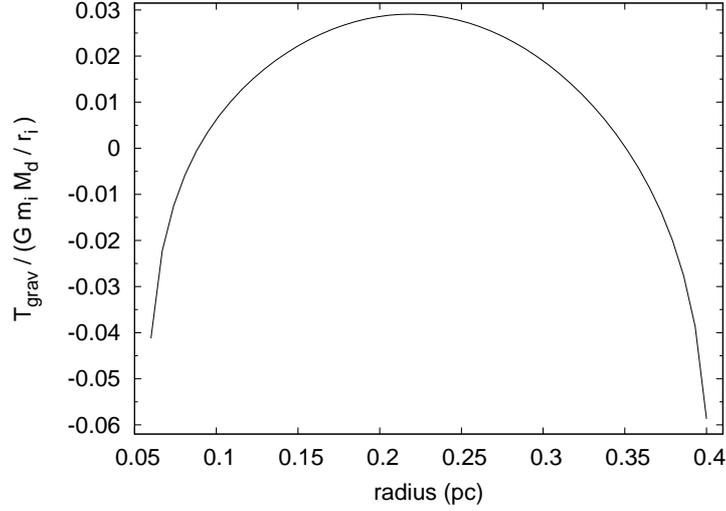
Figure 3.2: Normalized gravitational torque for the Galactic Center disk when the warp spans a range of $-12° \rightarrow 8°$ in inclination.

radiation pressure warping, and which sets up the warped density distribution in the Bardeen-Petterson mechanism, is given by:

$$2\pi r dr T_{\nu_2} = \frac{\Sigma r^2 \Omega 2\pi r dr}{2r^2/\nu_2} = \frac{\eta_\nu L\Omega r dr}{3\epsilon c^2}. \tag{3.16}$$

The gravitational torque of the disk on the same ring can be determined by integrating over the disk:

$$2\pi r dr T_{\text{grav}} \simeq \frac{GM_d \Sigma(r) 2\pi r dr}{r} J, \tag{3.17}$$

where $J \equiv T_{\text{grav}}/(Gm_i M_d/r_i)$ is a dimensionless integral depending on r/r_1, r/r_2:

$$J = \int_{r_1}^{r_2} \frac{2\pi r' dr' \Sigma(r')}{M_d} \frac{r^2 r'}{(r'^2 + r^2)^{3/2}} \sin(2\beta) \, I(\beta, r/r') \frac{\partial \beta}{\partial \theta}, \tag{3.18}$$

and where $\beta(r, r')$ is the angle between the normals of the two rings at r and r', θ is the inclination of the ring at r, so $\partial\beta/\partial\theta = O(1)$ [see eq. 2.14 in Chapter 2], and $I(\beta, r/r')$ is the integral in equation (2.13b) in the same chapter. We show in Figure 3.2 the values of the J-terms at different distances from the black hole when the warp spans a range of $-12° \rightarrow 8°$ in inclination. For larger warps, the gravitational torques are weaker. Also if we include the part of the disk outside $[r_{\text{in}}, r_{\text{out}}]$ the product $M_d J$ decreases as the torques are dominated by the nearby parts of the disk. Using the surface density profile above, the ratio of the radiation

and gravity torques is:

$$\frac{T_\Gamma}{T_{\text{grav}}} = \frac{L}{6cr}\frac{r}{2\pi GM_{\text{GCD}}\Sigma(r)J} = 123\frac{\eta_{\text{edd}}\epsilon_{\text{SF}}^2}{\mu_{4000}^2}\frac{\hat{r}^2}{J}, \tag{3.19}$$

and the ratio of the viscous torque to the gravitational torque is:

$$\frac{T_{\nu_2}}{T_{\text{grav}}} = \frac{\eta_\nu L\Omega}{3\epsilon c^2}\frac{r}{2\pi GM_{\text{GCD}}\Sigma(r)J} = 11.9\frac{\eta_{\text{edd}}\epsilon_{\text{SF}}^2}{\mu_{4000}^2\alpha\epsilon_{0.1}}\frac{\hat{r}^{3/2}}{J}. \tag{3.20}$$

We see from Figure 3.2 that the J-terms for the Galactic Center disk surface density profile are typically O(0.1). Thus at $r = 0.1$ pc $T_\Gamma \gg T_{\text{grav}}$ if $\epsilon_{\text{SF}} < 1$, but not if $\epsilon_{\text{SF}} \ll 1$. For a high central luminosity η_{edd} and/or high star formation ϵ_{SF} the viscous torque on the disk dominates over its self-gravity. We have also seen for the case of the Bardeen Petterson effect that $\epsilon_{\text{SF}} < 1$. This shows that it is justified to neglect the effects of the gravitational torques on the evolution of the disk in its active phase.

3.2.5 The Warped Stellar Disk After Fragmentation

In sections (3.2.2) and (3.2.3) we have seen that for a range of assumed accretion disk parameters, the disk at the Galactic Center could have been warped in the accretion phase. The evolution of the disk is likely to be governed by the viscous or radiation torques during this phase.

We now assume that after some time the disk has become warped, the active phase of the Galactic Center ends. Since η_{edd} and the accretion rate will then be highly reduced the disk will receive much smaller energy input and it is reasonable to assume that it can now cool rapidly. If the cooling time is short, fragmentation and star formation can occur an a dynamical time scale (Gammie, 2001). The gas content of the disk could then be converted into stars with efficiency ϵ_{SF} and the rest of the gas will be lost.

Subsequently, the now stellar disk would evolve purely gravitationally. We have seen in Chapter 2 that the rate of the precession induced by the self-gravity of the disk depends on the disk-to-black mass ratio approximately as $\dot{\phi} \equiv \mathcal{C}(\theta)\Omega M_d/M_{bh}$, so we expect more massive disks for the otherwise set of identical parameters precess faster.

3.3   Warp Model for the Galactic Center Disk

In the previous sections we have argued that for a range of parameters, a flat disk around SgrA* could become warped before forming stars, after which the disk evolves gravitationally. In this section, we will introduce the model we have used to to follow the time evolution of the warped stellar disk.

3.3.1   The Equations of Motion

As in Chapter (2), we model a warped disk as a collection of concentric circular rings which are tilted with respect to each other, and which are are in gravitational interaction with each other. They are characterized by their masses m_i, and radii r_i. The fast orbital motion around the SMBH of mass M_{bh} is thereby time-averaged. The geometry of the rings is defined by the Euler angles (ψ, θ, ϕ). For a system of n rings, the equations of motion for any of the rings i are given by:

$$p_{\theta_i} = \frac{m_i r_i^2}{2} \dot{\theta}_i, \tag{3.21}$$

$$p_{\phi_i} = \frac{m_i r_i^2}{2} \dot{\phi}_i \sin^2 \theta_i + p_{\psi_i} \cos \theta_i, \tag{3.22}$$

$$\dot{p}_{\theta_i} = \frac{m_i r_i^2}{2} \dot{\phi}_i^2 \sin \theta_i \cos \theta_i - \dot{\phi}_i p_{\psi_i} \sin \theta_i - \frac{\partial V_i}{\partial \theta_i}, \tag{3.23}$$

$$\dot{p}_{\phi_i} = -\frac{\partial V_i}{\partial \phi_i}. \tag{3.24}$$

Here $p_{\psi_i} = m_i r_i^2 \Omega_i$ is the orbital angular momentum, $\dot{\phi}_i$ and $\dot{\theta}_i$ are the rates of precession and nutation caused by the torques $\partial V_i / \partial \theta_i$ and $\partial V_i / \partial \phi_i$ respectively where V_i is the potential energy of ring i in the field of the other rings.

The numerical approach we use to study the time evolution of the disk is similar to the one presented in Chapter 2. There, we integrated the equations of motion for the rings after evaluating the steadily precessing equilibria for the given parameters to test the stability of those configurations. For parameters relevant to the GC disk we do not find such steadily precessing equilibria. Here we adopt as the initial warp shapes, the disk configurations which are likely to be imposed by the warping mechanisms discussed in the previous sections.
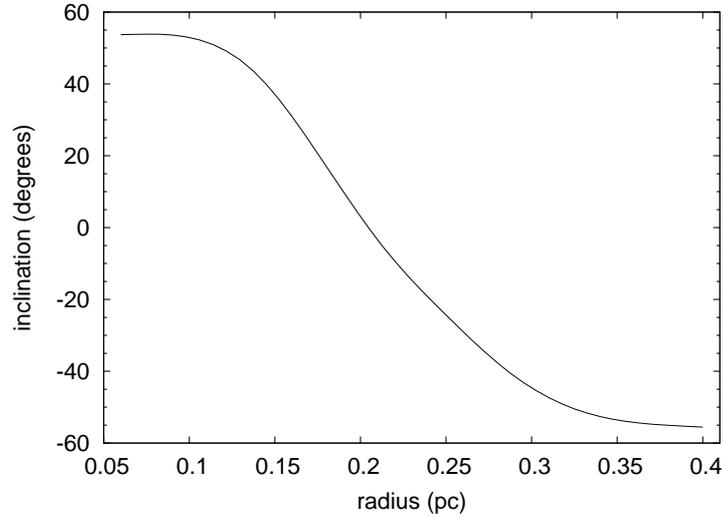
Figure 3.3: Approximate initial warp shape as imposed by radiation instability. Adopted from Pringle (1997).

3.3.2 Numerical Setup and Initial Conditions

In the simulations we have performed, we distribute the rings equally in radius between $r_{\mathrm{in}} = 0.06$ pc, and $r_{\mathrm{out}} = 0.4$ pc. The initial conditions, i.e. the inclination, and azimuth of the rings are chosen to mimic a radiation or Bardeen Petterson warping.

For the radial structure of a radiation warped disk, we adopt the approximate nonlinear warp shape obtained by Pringle (1997) which we show in Figure 3.3. Keeping the shape of the warp similar to those presented by Pringle (1997), we scale its amplitude to simulate disks with various degrees of warping. These nonlinear warp shapes are such that the inner rings share a common plane in inclination, then beyond a radius r in the disk the inclination changes gradually. The outer parts of the disk are again coplanar which comes about because of the assumption that the disk becomes optically thick to radiation and warping does not proceed there.

The initial conditions for the Bardeen Petterson effect are adopted from Lodato & Pringle (2007) such that:

$$
\begin{aligned}
\theta_i &= \begin{cases} -0.5 & \text{for } r < r_1, \\ 0.5\sin(C(\theta)) & \text{for } r_1 \le r \le r_2, \\ 0.5 & \text{for } r > r_1, \end{cases} \\
\phi_i &= 0,
\end{aligned}
\tag{3.25}
$$
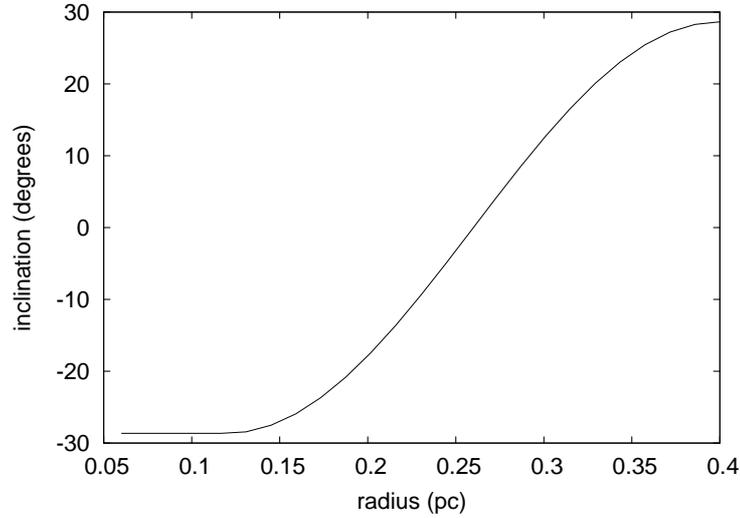
Figure 3.4: Approximate initial warp shape as imposed by Bardeen Petterson effect (adopted from Lodato & Pringle (2007)).

where $C(\theta) = \pi(r - r_0)/(r_2 - r_1)$, $r_0 = (r_1 + r_2)/2$, and we set $r_1 = 0.1$ pc, and $r_2 = 0.35$ pc. Figure 3.4 shows the inclination of the disk at different radii for the Bardeen Petterson initial conditions.

We consider two cases for the surface density one of which is constant with radius, and the second one decreases as $1/r^2$. Table (3.2) summarizes the parameters of the runs that we will discuss in the next section.

3.4   Results

In this section we show examples of simulations following the time evolution of the remnant stellar disk in which the disk mass takes different fractions of the black hole mass around which it rotates.

We first consider the evolution of a light disk with $M_d/M_{bh} = 0.001$, and a surface density profile decreasing as $1/r^2$. This is our model M1. The adopted disk mass implies the assumption that the star formation efficiency was $\epsilon_{SF} = 1$. We choose an initial warp shape which mimics a radiation pressure origin. At the start of the simulation, i.e. at $t = 0$, the disk spans a range of $\Delta\theta_{max} = 58°$ in inclination, and the azimuthal angles form a spiral. The disk is initially given a constant precession frequency. We followed the evolution of this system for 1000 orbital periods. In Figure 3.5 we show the 3-dimensional shape of the disk at various stages of the simulation. We see immediately that due to the long precession time

Model	$M_\mathrm{d}/M_\mathrm{bh}$	Σ	shape$|_\mathrm{i}$	$\Delta\theta_\mathrm{max}$
M1	1×10^{-3}	$1/r^2$	R	58°
M2	1×10^{-3}	$1/r^2$	R	218°
M3	1×10^{-3}	const.	R	110°
M4	1×10^{-3}	const.	R	110°
M5	3×10^{-3}	$1/r^2$	BP	58°
M6	6×10^{-3}	$1/r^2$	BP	58°
M7	1×10^{-2}	$1/r^2$	BP	58°
M8	1×10^{-2}	$1/r^2$	BP	58°

Table 3.2: Parameters of the simulations performed. The first column is the name associated with the simulation. The second column is the disk mass expressed in terms of the black hole mass, and the third column is the surface density profile where *const.* stands for constant. The fourth column is the assumed initial shape of the warp. The abbreviations $\mathrm{R, BP}$ stand for radiation warping and, Bardeen-Petterson warping respectively. The fifth column is the magnitude of the initial inclination of the warp such that $\Delta\theta_\mathrm{max} = |\theta_\mathrm{in} - \theta_\mathrm{out}|$.

scale induced by the self-gravity torques, the disk doesn't change its appearance noticeable. The initially adopted inclinations also do not vary in time, and although they can not be treated as the equilibrium solutions presented in Chapter 2, they remain constant.

In order to see whether initially more inclined warps exhibit a different behavior, we next consider a disk which has an inclination of $\Delta\theta_\mathrm{max} = 218°$ in our model M2. It is also for a disk with a mass fraction of $M_d/M_{bh} = 0.001$, and a surface density profile $1/r^2$. In Figure 3.6 we show the 3d views of the disk at different times. Although the initial warp shape is noticeably different from the previous example, the evolution of the disk proceeds in a similar way to the previous example in that the appearance of the disk remains almost unaltered. This comparison leads to the conclusion that for a mass ratio 10^{-3} the initial inclination of the disk does not affect its evolution in the pure self-gravity regime.

The next thing we would like to investigate is the possible effect of a change of distribution of mass in the disk. We therefore adopt a constant surface density profile for the same total mass in model M3. This model is followed for 1000 orbital periods. We see in Figure 3.7 that the result is similar to M1 in that the disk doesn't exhibit a noticeable change in its shape. The rings precess slowly under the mutual gravity torques while their inclinations do not deviate from their initial values.

The last example we would to discuss for the same mass fraction differs from previous one in that initially, the azimuthal angles of the rings form a spiral line of nodes. We therefore aim at exploring whether the gravity torques in such a case will destroy the coherence
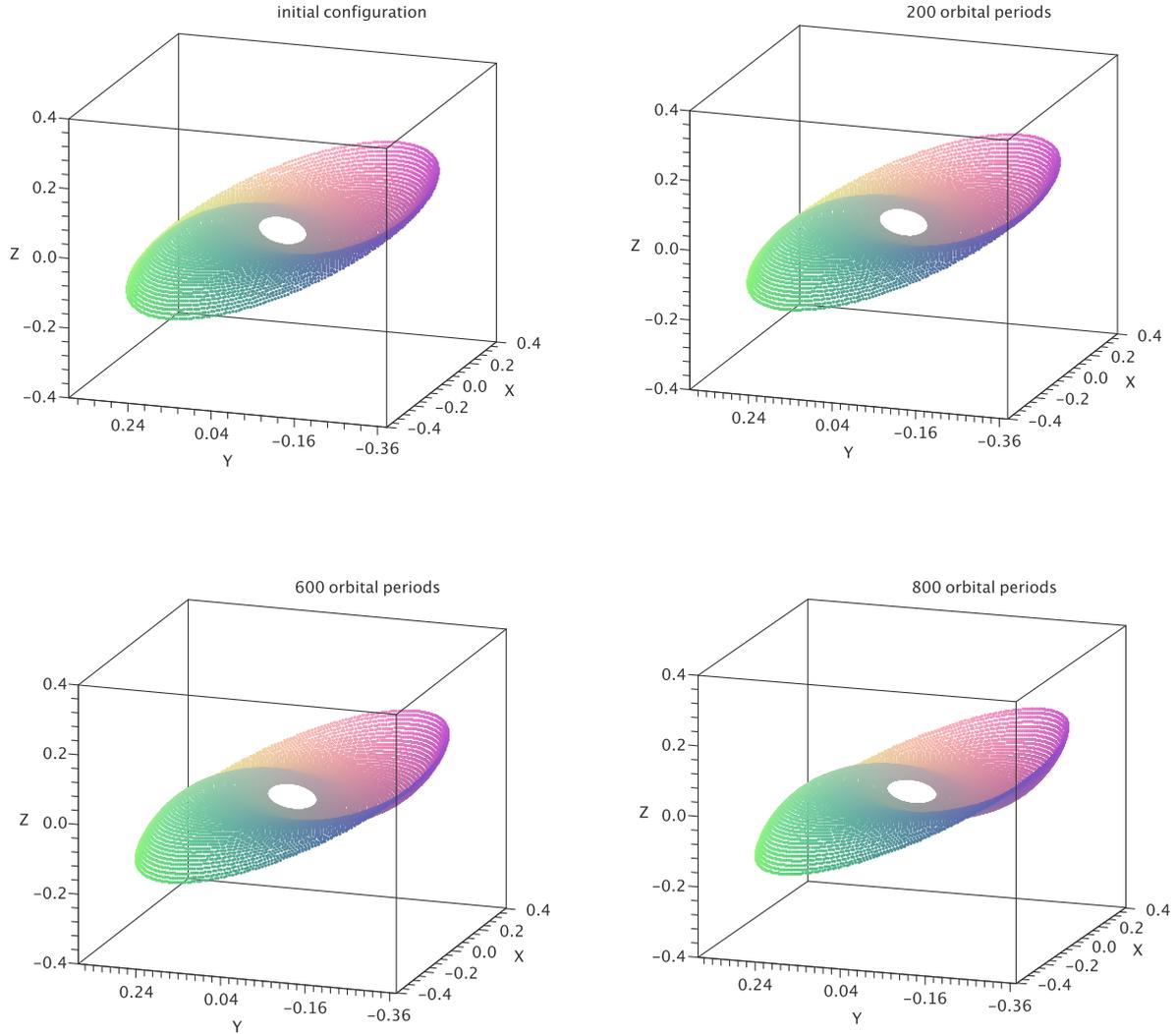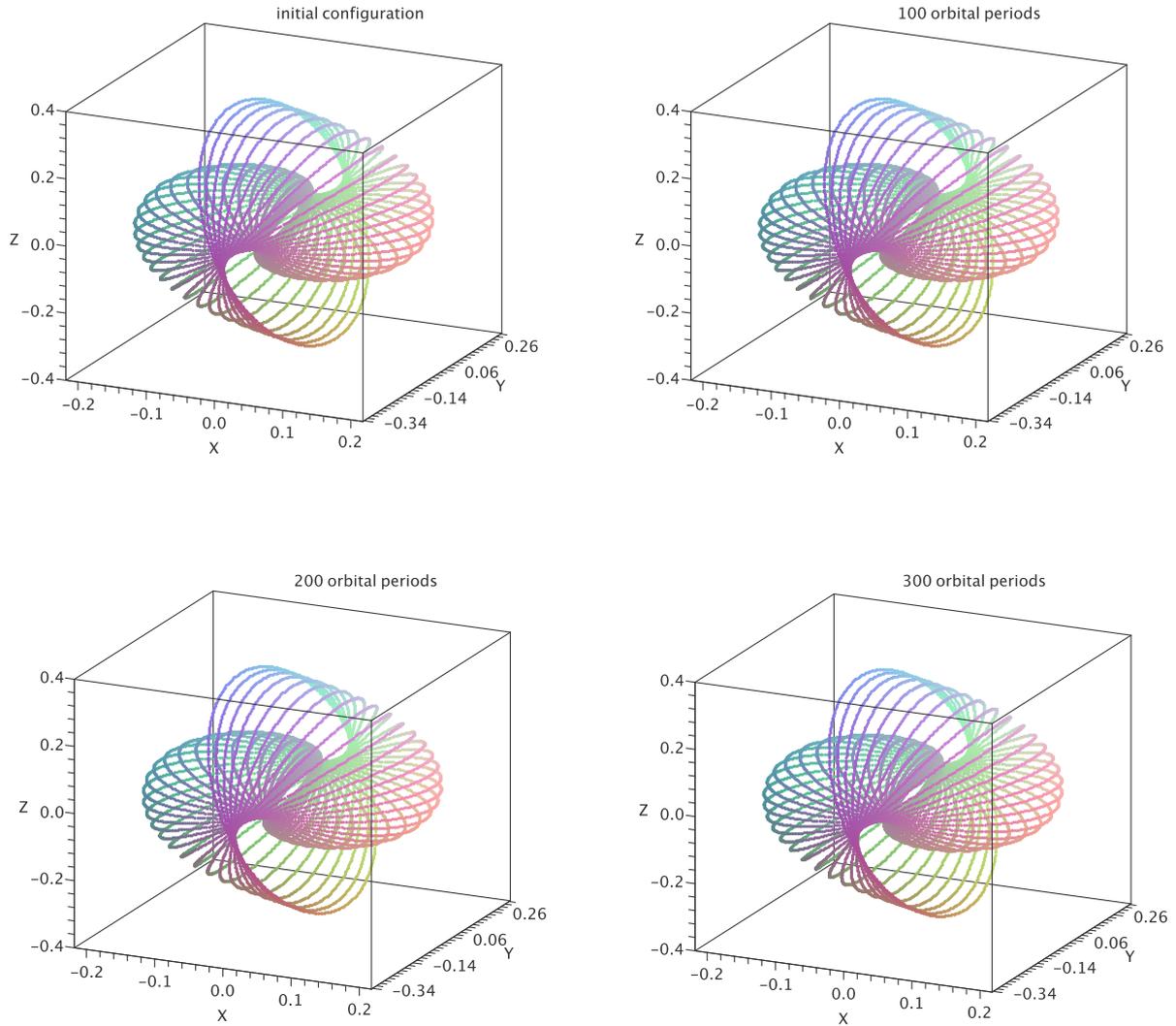
Figure 3.5: 3d views of the M1 disk at different stages of its evolution. The disk has a mass of $M_d/M_{bh} = 0.001$, and a $1/r^2$ surface density profile. The initially imposed warp has an amplitude of $\Delta\theta_{\max} = 58°$.
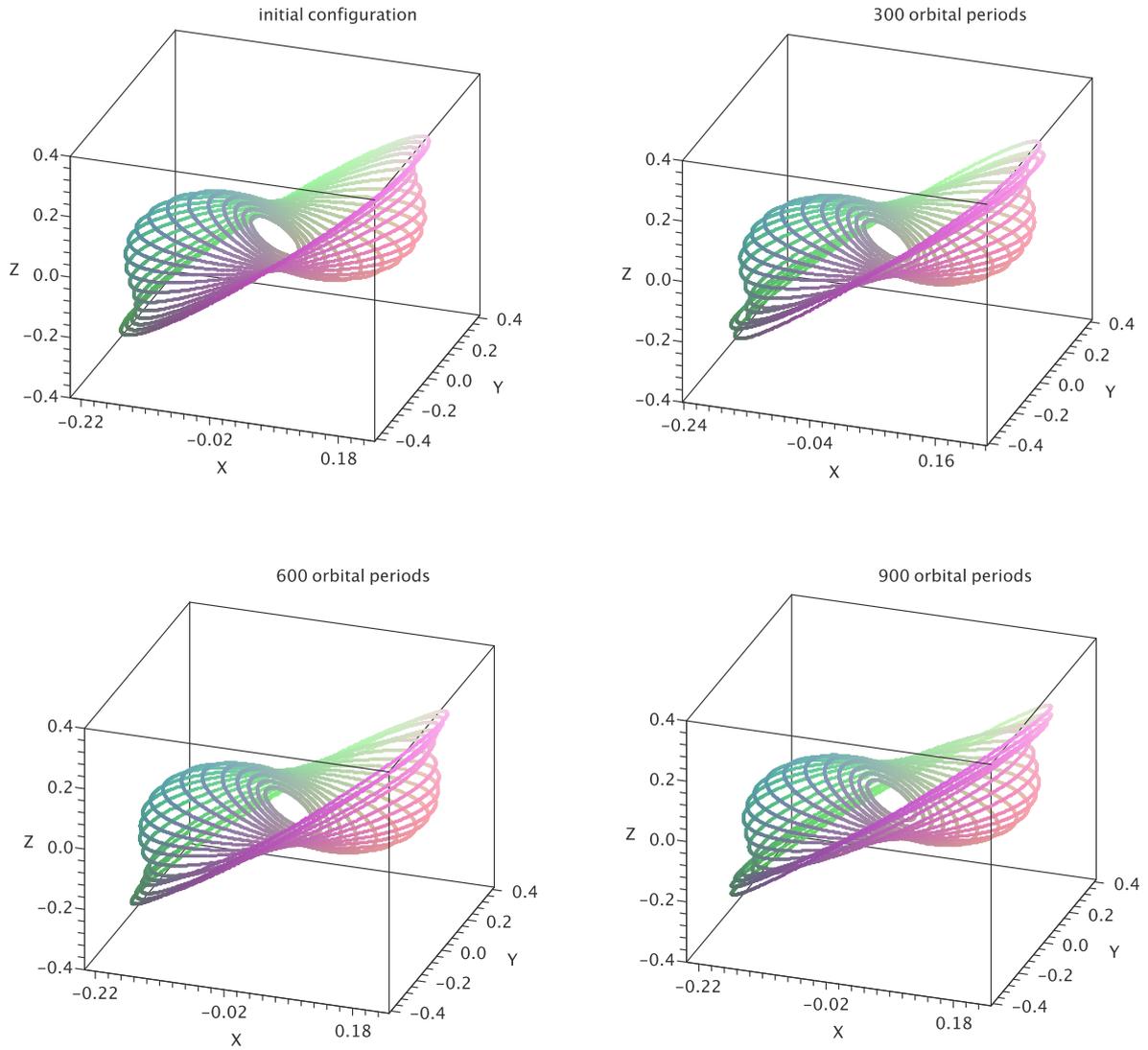
Figure 3.6: 3d views of the M2 disk at different stages of its evolution. The disk has a mass of $M_d/M_{bh} = 0.001$, and a $1/r^2$ surface density profile. The initially imposed warp has an amplitude of $\Delta\theta_{\max} = 218°$.

Figure 3.7: 3d views of the M3 disk at different stages of its evolution. The disk has a mass of $M_d/M_{bh} = 0.001$, and a constant surface density profile. The initially imposed warp has an amplitude of $\Delta\theta_{\max} = 110°$.

of the disk. This initial warp shape is accounted for in the time integration such that the term $\partial V_m(\alpha_{ij})/\partial \phi_{ij}$ is not zero at the start of the run. The evolution of the disk is depicted in Figure 3.8. We observe in this case again that the disk doesn't show a substantial amount of variation in its shape. Examples discussed so far show that regardless of the initial warp shape, and surface density profile, the disks for the adopted total mass remain almost un-altered during their evolution. As we have seen in Chapter 2, the precession frequency of self gravitating warped disks depends on the mass of the disk in proportion the black hole mass. For the same warp shape, more massive disks precess faster, so one might expect see to changes in the disk structure much faster for such disks. Hence in the following, we discuss a few examples where more massive warped disks have been considered.

In model M5, we consider a disk with a mass fraction of $M_d/M_{bh} = 0.003$. The initial warp shape is such that it spans a range of $\Delta\theta_{\max} = 58°$ in inclination, and the azimuthal angles form a spiral. These initial conditions are chosen to mimic a Bardeen Petterson warp-ing origin although the shape of the warp is similar to that in model M1. The steps of the evolution are show in Figure 3.9. Compared to the lower mass examples, the evolution of this disk is becoming more apparent. At the end of the simulation, the flattening of both the inner and outer parts of the disk can be observed.

Yet a higher disk mass is adopted in M6 where $M_d/M_{bh} = 0.006$. Initially, the disk is given a differential precession rate. The evolutionary steps are shown in Figure 3.10. We see in this example that as the disk evolves, the middle rings start to separate from each other in inclination giving the disk a "broken" shape. In Figure 3.11 we show how the inclination of the rings change in time. Any vertical cut along the curves corresponds to the ring inclina-tions at that particular time. The negative inclinations are of the inner rings, while the outer rings are at positive inclinations. At the end of the simulation at about 6×10^5 yr, the outer parts of the disk form a disk-like structure with a warp of about $25°$, while the inner parts cluster more closely to each other leaving behind a warped disk with an amplitude of $\sim 10°$. The separation between the two increases slowly in time and reaches $30°$ at the end of the simulation.

Simulations so far discussed shows that the main parameter controlling the evolution of the disk is its mass. Although slight changes in the evolutionary steps can be expected for varying initial conditions, the behavior is similar in all these models. To strengthen this idea, we next discuss the highest mass models we have in our simulations.

M7 is the time evolution of a disk with a mass fraction of $M_d/M_{bh} = 0.01$. The initial warp shape and surface density profile imposed to the model are similar to M6. The evolution
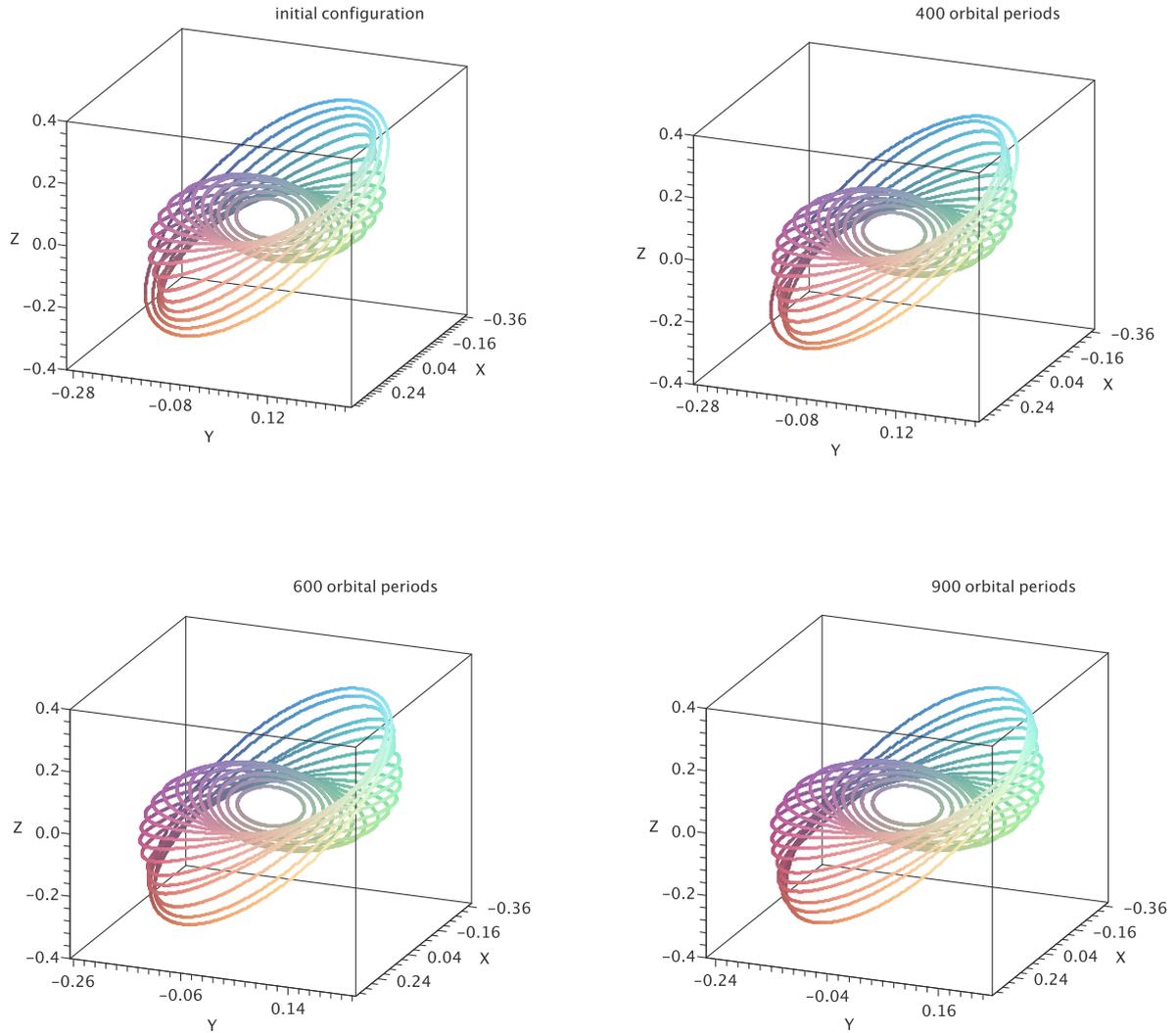
Figure 3.8: 3d views of the M4 disk at different stages of its evolution. The disk has a mass of $M_d/M_{bh} = 0.001$, and a constant surface density profile. The initially imposed warp has an amplitude of $\Delta\theta_{\max} = 110°$.
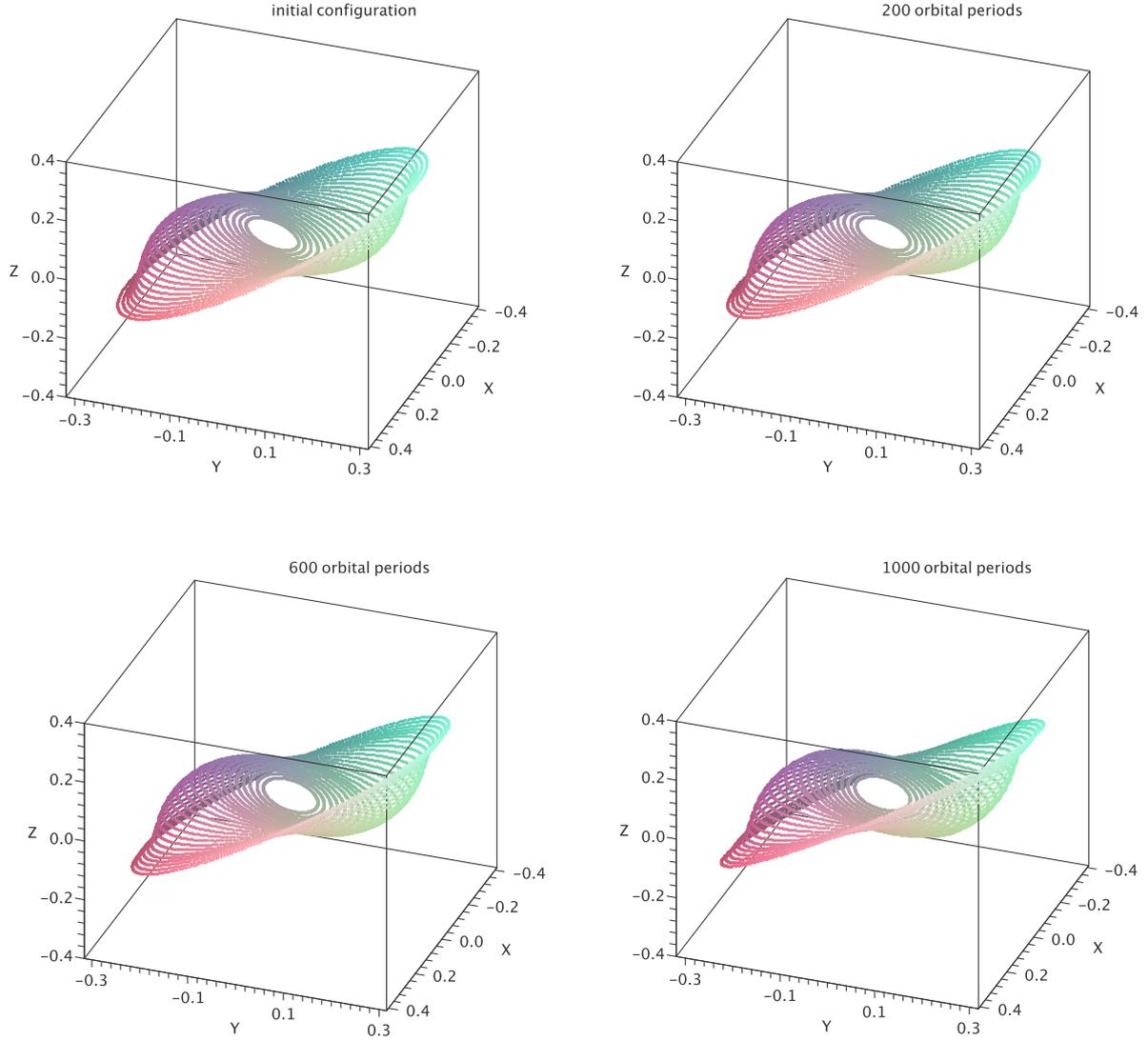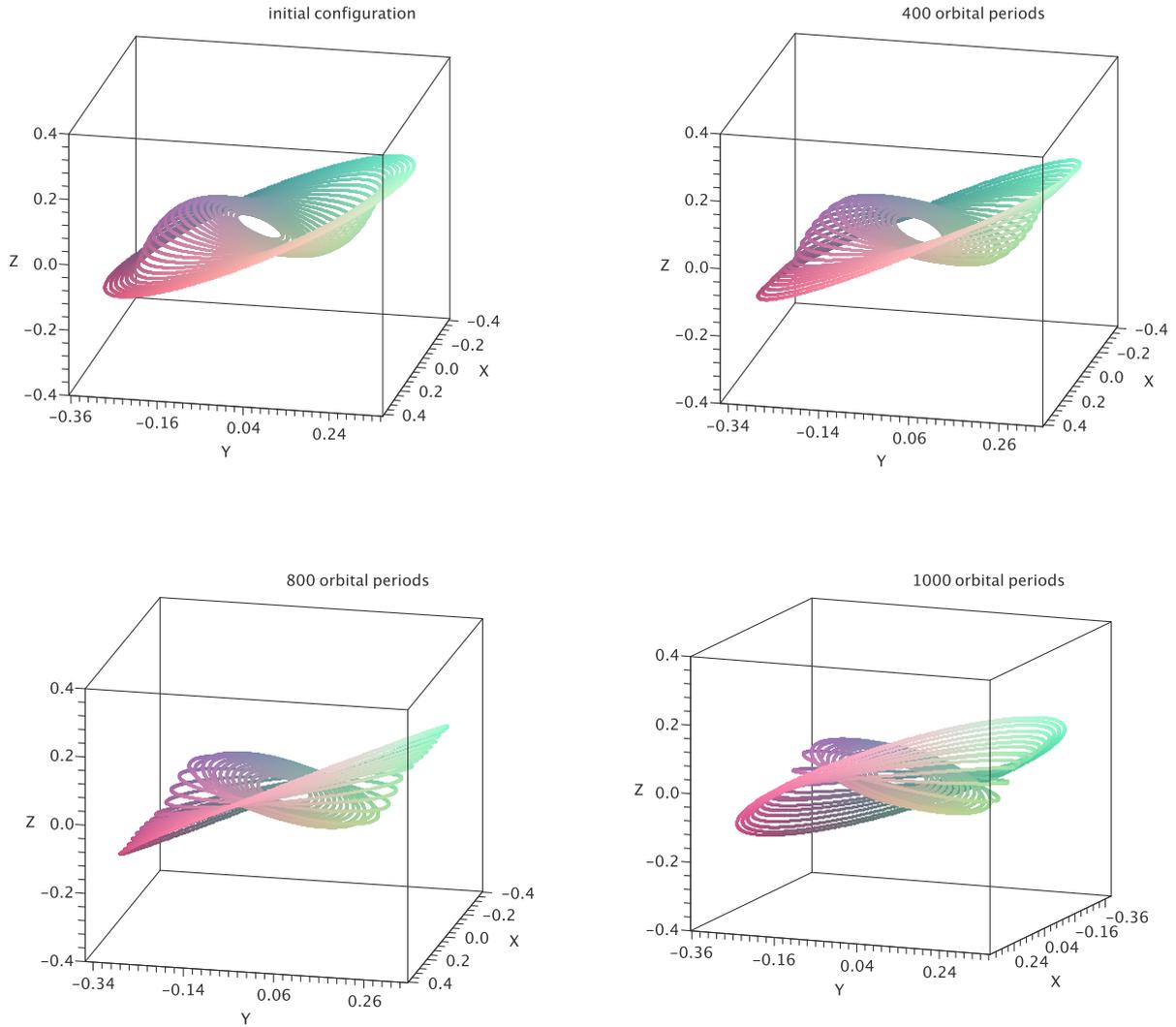
Figure 3.9: 3d views of the M5 disk at different stages of its evolution. The disk has a mass of $M_d/M_{bh} = 0.003$, and a $1/r^2$ surface density profile. The initially imposed warp has an amplitude of $\Delta\theta_{\max} = \sim 58°$.
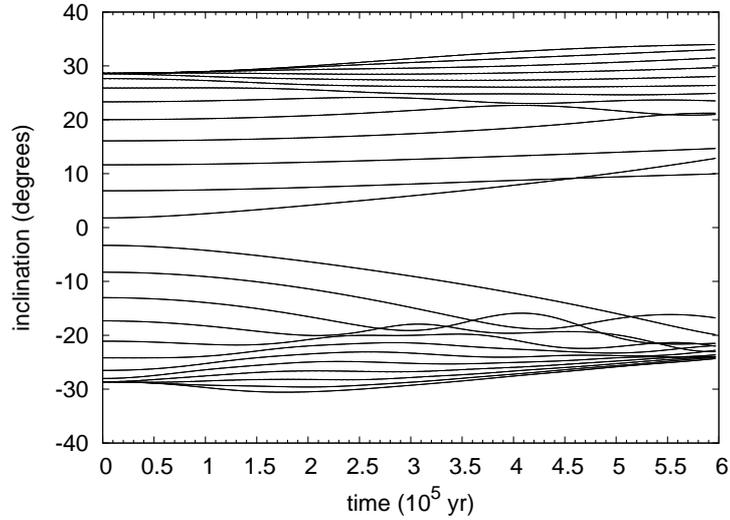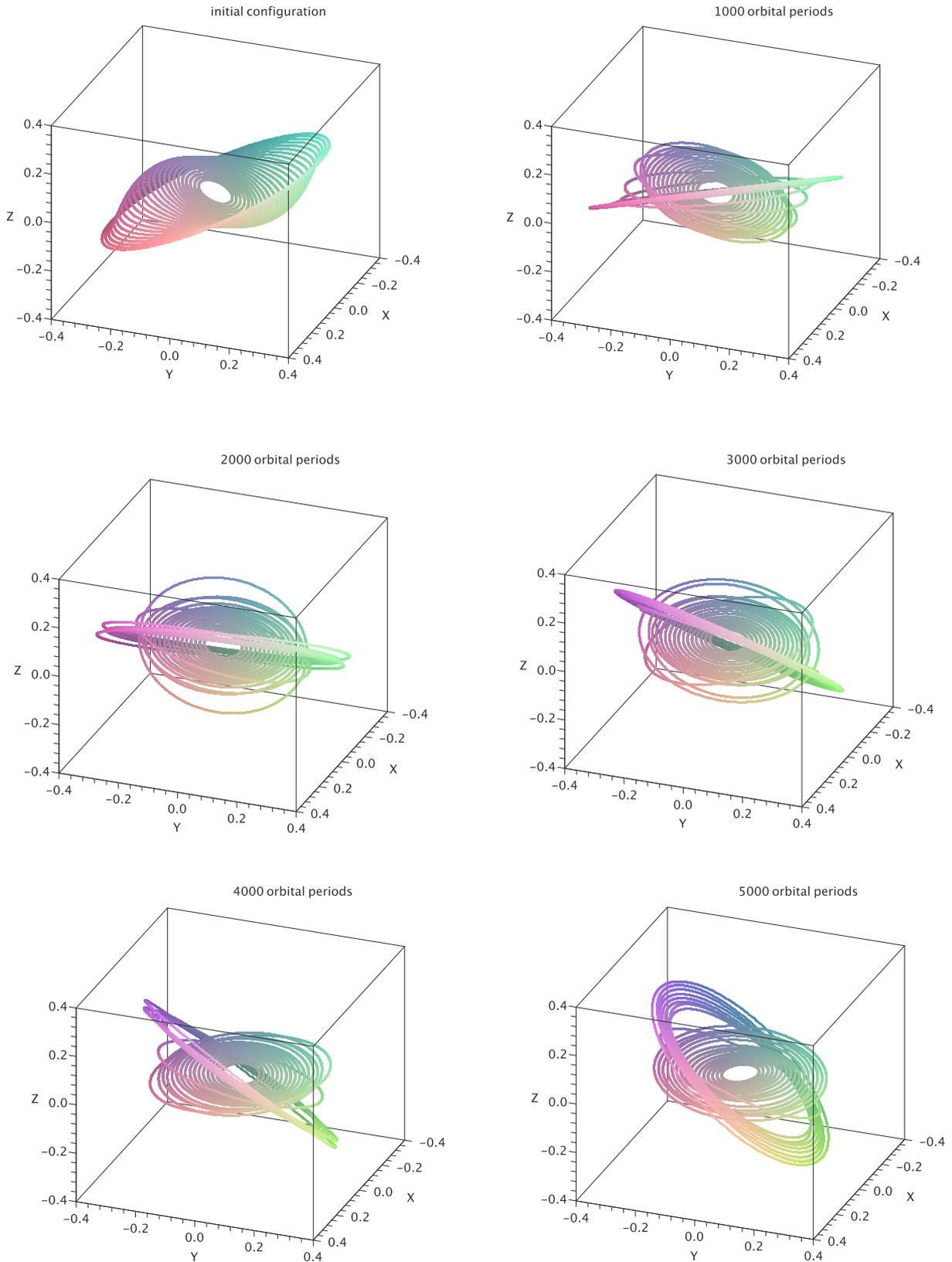
Figure 3.10: 3d views of the M6 disk at different stages of its evolution. The disk has a mass of $M_d/M_{bh} = 0.006$, and a $1/r^2$ surface density profile. The initially imposed warp has an amplitude of $\sim 58°$.

Figure 3.11: The change of ring inclinations in time for model M6.

of the disk is followed for 5800 orbital periods. Figure 3.12 shows the evolution in steps of 1000 orbital periods. We see that at already 1000 orbital periods, the disk can be recognized as two disks broken out of a single one.

In the literature simulations aiming to explain the orbital configuration of the GC stellar disks often start with initial conditions such that there are already two mutually inclined disks/rings in place (Nayakshin et al., 2006; Löckmann & Baumgardt, 2009). The evolution of these disks is then followed depending on the ingredients of the model, and it is often found that differential precession destroys the coherence of the two disks in about a million years. In these simulations, self-gravity of the disk is mostly neglected, or accounted for in the simplified linear torques regime. To compare our models to the previous studies, we evolved our model M7 for nearly 3.5×10^6 yr. The comparison to previous studies becomes more relevant after our single disk breaks into two disks, i.e. after 1000 orbital periods. We see that even though the initial precessing disk breaks into two pieces, the broken disks continue precessing without further deformation. Figure 3.13 shows for this model the evolution of the ring inclinations. After about 1×10^6 yr, the rings are arranged such that inner and outer ones form two relatively flat disks. The inner disk at negative inclinations has on average a warp with about $10°$, while the outer one is warped by only a few degrees. The mutual inclination between the two disk is about $55°$ at the end of the simulation. In Figure 3.14 we show how the azimuthal angles evolve for the same model. Again the azimuth for each ring corresponds to vertical cuts through the plots.

The last example we discuss is again for a disk with a mass fraction of $M_d/M_{bh} = 0.01$.

Figure 3.12: 3d views of the M7 disk at different stages of its evolution. The disk has a mass of $M_d/M_{bh} = 0.01$, and a $1/r^2$ surface density profile. The initially imposed warp has an amplitude of $\Delta\theta_{\max} = 58°$.
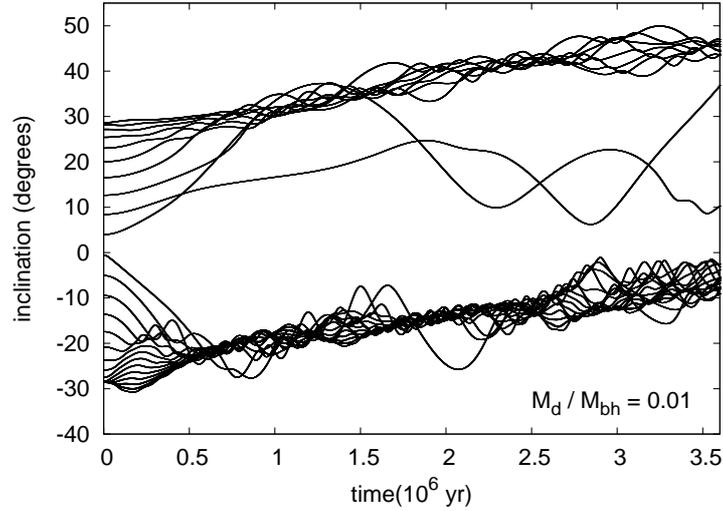
Figure 3.13: The change of ring inclinations in time for model M7.

This is our model M8. In comparison to M7, the disk is initially given a differential precession frequency. We aim to explore whether for massive disks this initial condition would lead to a dissolving disk structure. In Figure 3.15 we show the evolutionary steps in warp shape for this model. In comparison to model M7, model M8 shows only a very slight difference in the shape of the outer disk after 5000 orbital periods. The outer disk of M8 is warped by a few degrees more than that of M7, but apart from this difference, the evolution of both disks is very similar. Hence we can conclude that also for massive disks the initial conditions prior to self-gravitating evolution does not change the overall behavior.

Simulations we have presented suggest that an initially warped single disk of stars at the Galactic Center is prone to breaking into two pieces if the mass of the disk exceeds $0.001M_{bh}$. The time when the disk can be recognized as two separate disks depends on the total mass of the disk. Since the disk determines the global precession frequency of the disk, we can expect to see a correlation between the mutual inclination of the broken disks and the precession frequency, and hence precession time scale for a given model. In Figure 3.16 we see indeed that there is such a correlation. The points in the plot correspond to maximum separation angles of the models we have discussed at different stages of the evolution. The precession time scale shown on the horizontal axis is calculated as follows: for each model the mean
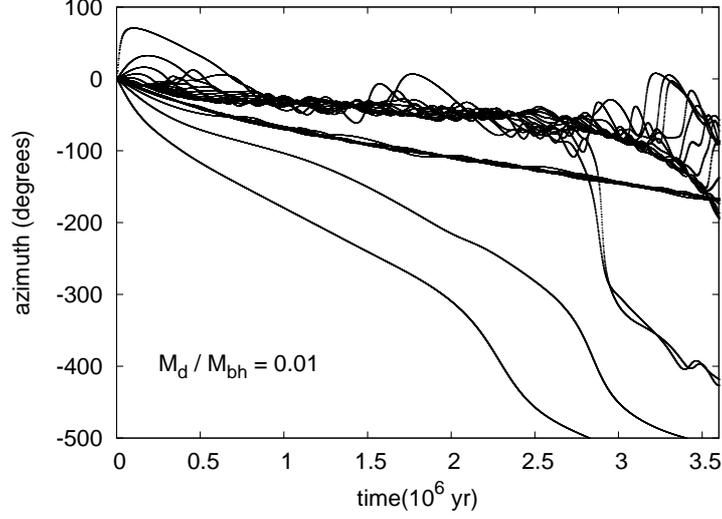
Figure 3.14: Time evolution of azimuth for model M7.

precession time scale is calculated at the end of the run such that:

$$\tau_{\mathrm{prec}} = \frac{2\pi}{\dot{\phi}_{\mathrm{mean}}} = \frac{2\pi n}{\displaystyle\sum_i \dot{\phi}_i} \tag{3.26}$$

where $\dot{\phi}_i$ are the precession frequencies of the rings attained at the end of the particular integration. In determining the maximum separation between the broken disks, we read in the difference in inclinations where the separation starts. The points lying at the bottom left corner are those of the small mass models, where the horizontal branch of points to the right correspond to high mass models. We see that when the gravity torques are low, i.e. for small mass, the maximum separation in the broken disk increases linearly in precession time, until about 35 precessions. For models corresponding to higher precession rates, the separation angle saturates at about 45 degrees, and the two broken disks continue precessing without further deformation with their own mean rates.

3.5   Comparison With the Observations

In this section, we would like to make a comparison of our time evolution models and the observations of the Galactic Center disks. In doing so, we will mostly make use of the results of Bartko et al. (2009).

After application of proper selection criteria, Bartko et al. (2009) sample includes a to-
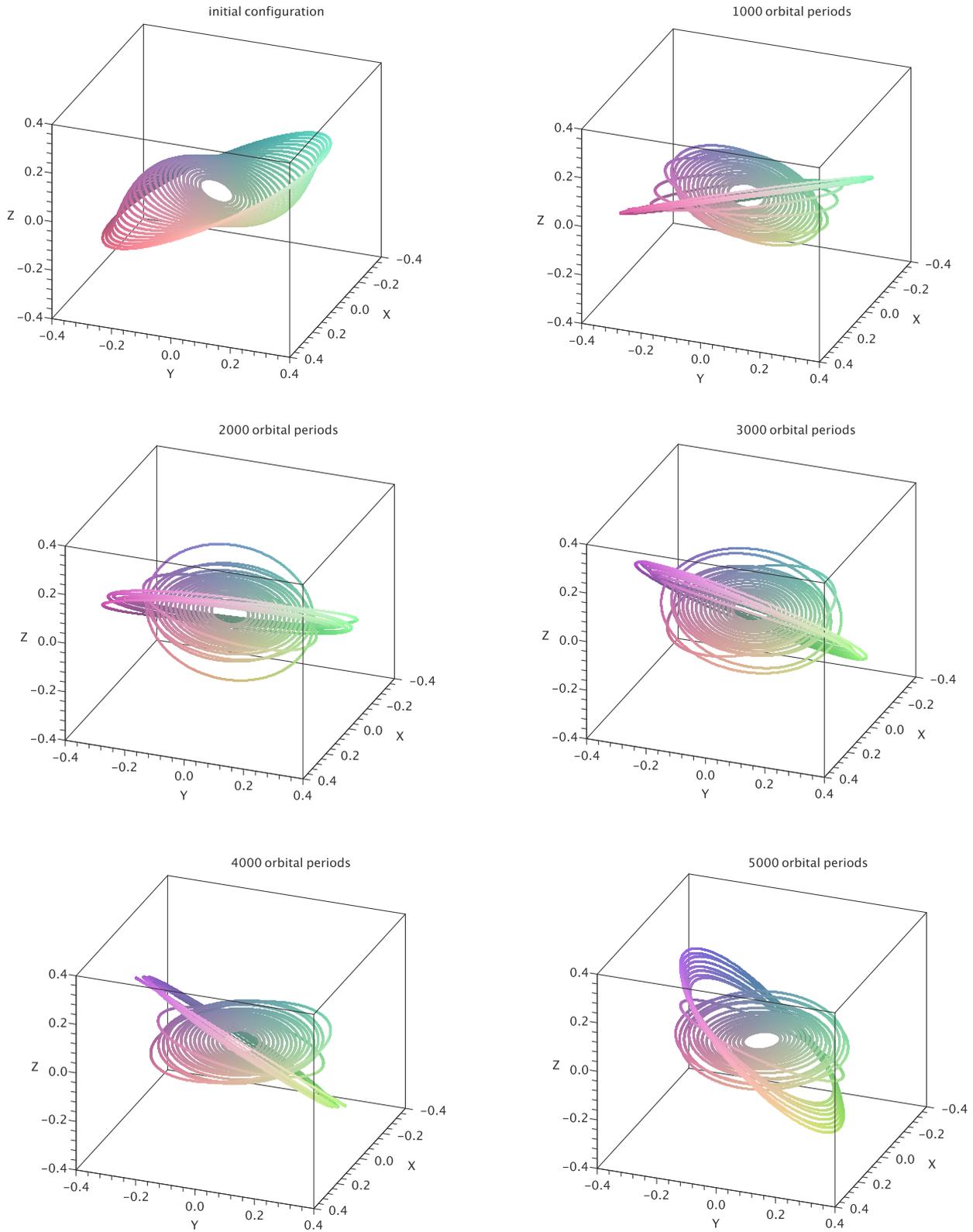
Figure 3.15: 3d views of the M8 disk at different stages of its evolution. The disk has a mass of $M_d/M_{bh} = 0.01$, and a $1/r^2$ surface density profile. The initially imposed warp has an amplitude of $\Delta\theta_{\max} = 58°$.
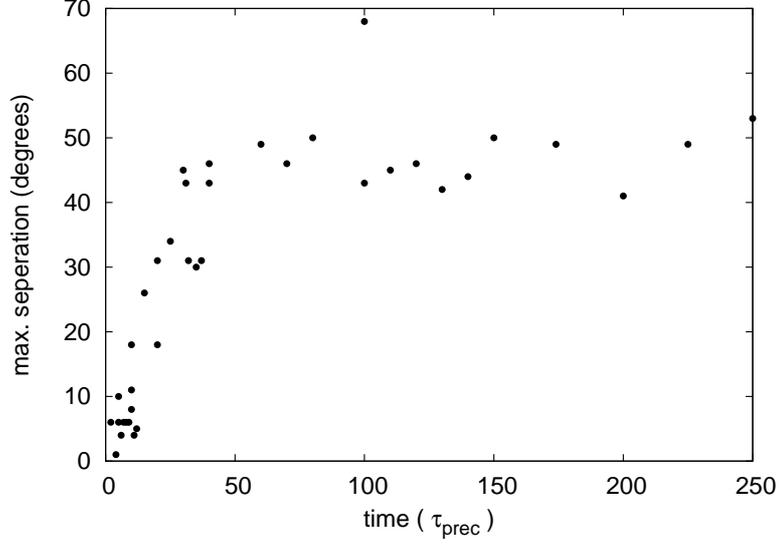
Figure 3.16: Maximum separation of the disk versus mean precession time at the end of each run.

tal of 90 stars on clockwise and counterclockwise rotating orbits. Out of these 90, 27 are new identifications, and the rest have reduced proper motion uncertainties. These stars have measured x, y, and z space positions (with z coordinate being the less well defined), and the respective space velocities v_x, v_y, and v_z.

The number density of stars in the disks, $\Sigma_{\mathrm{nr}}(r)$, scales as $1/r^2$ (Bartko et al., 2009; Paumard et al., 2006). Here r is the 3-dimensional distance to SgrA*, corresponding to the radius r of our rings. The total number of stars on a ring is then $2\pi r \Delta r \Sigma_{\mathrm{nr}}(r)$. If we assume that the total number of stars in the disk is N_t we can write:

$$\sum_{1}^{n} 2\pi r \Delta r \Sigma_{nr}(r) = N_t, \tag{3.27}$$

where n is the number of rings making up the disk. We write $\Sigma_{\mathrm{nr}}(r) = \Sigma_0/r^2$. The normalization Σ_0, i.e the number of stars on the innermost ring, is then obtained by writing:

$$\Sigma_0 = \frac{N_t}{2\pi \Delta r \sum_{1}^{n} \frac{1}{r}}. \tag{3.28}$$

Figure 3.17 shows the expected number of stars on each ring when $N_t = 1000$ for a disk of 25 rings.
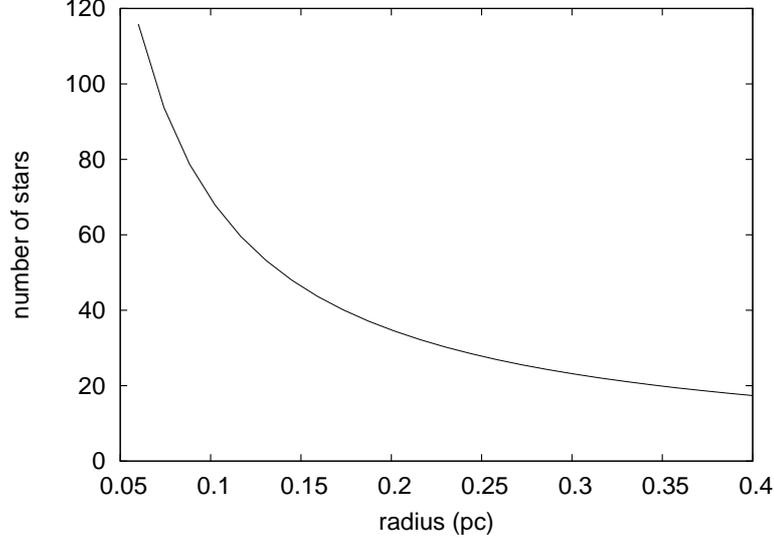
Figure 3.17: Radial distribution of 1000 stars on a disk consisting of 25 rings.

The coordinates of a star on a ring is given by:

$$
\begin{aligned}
x &= \cos\phi\cos\psi - \cos\theta\sin\phi\sin\psi, \\
y &= \sin\phi\cos\psi + \cos\theta\cos\phi\sin\psi, \\
z &= \sin\theta\sin\psi.
\end{aligned}
\tag{3.29}
$$

Here, θ is the inclination of the ring to the plane perpendicular to the total angular momentum direction, ϕ is the azimuthal angle, and ψ is the position of the star on its ring. We distribute the stars randomly in ψ on the rings. Figure 3.18 shows, for four of our models, the random distribution of a total of 1000 stars on the disks. The models are M5 (top left), M6 (top right), M7 (bottom left), and M4 (bottom right). Model M7 is depicted at 5000 orbital periods of its evolution where the other models are shown at their 1000 orbital periods stage.

As can be seen from Figure 3.18 the model M5, for a disk of mass $M_d/M_{\mathrm{bh}} = 0.001$, precesses as a single disk without deformation. Its initially imposed warping angle is conserved through its evolution. The model disk M6 is a slightly more massive one with $M_d/M_{\mathrm{bh}} = 0.006$, and it has already started to break. The model disk M7 is one of the most massive examples we considered in our simulations having $M_d/M_{\mathrm{bh}} = 0.01$, and after 5000 orbital periods, it settled down to a well-defined two-disk system. Finally, M4 is again for a light non-breaking disk with $M_d/M_{\mathrm{bh}} = 0.001$, but with an initial warp amplitude much higher than that of M5.
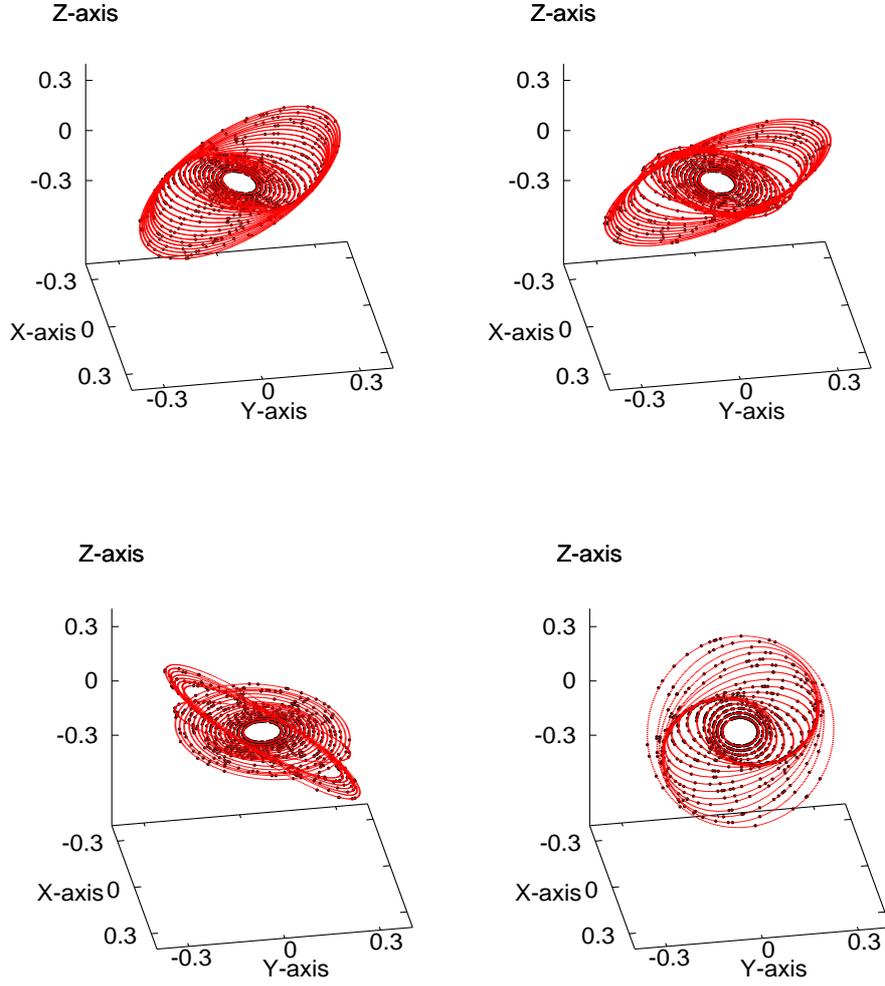
Figure 3.18: Random distribution of stars on model disks M5 (top left), M6 (top right), M7 (bottom left), and M4 (bottom right).

In order to construct the phase space distributions of the stars populating the disks, we write the components of the stellar velocities:

$$
\begin{aligned}
v_x &= r(\dot{\theta}\sin\theta\sin\psi\sin\phi - \dot{\psi}\sin\psi\cos\phi - \dot{\phi}\sin\phi\cos\psi - \dot{\phi}\cos\theta\cos\phi\sin\psi, \\
&\quad - \dot{\psi}\cos\theta\sin\phi\cos\psi) \\
v_y &= r(\dot{\phi}\cos\phi\cos\psi - \dot{\phi}\cos\theta\sin\phi\sin\psi + \dot{\psi}\cos\theta\cos\phi\cos\psi \\
&\quad - \dot{\theta}\sin\theta\sin\psi\cos\phi - \dot{\psi}\sin\psi\sin\phi), \\
v_z &= r(\dot{\theta}\sin\psi\cos\theta + \dot{\psi}\sin\theta\cos\psi). \tag{3.30}
\end{aligned}
$$

Since we know the values of $(\dot{\phi}, \dot{\theta}, \dot{\psi}, \phi, \theta)$ from our time integration, and we dice the ψ coordinate, we can construct the phase space distribution of stars at each instant of time using equations (3.29) and (3.30) .

A comparison of the models to the observed disks can be made by comparing the projections of the angular momentum directions of the two. In the following we show examples of such comparisons.

The first set of comparisons considers the cylindrical equal-area projections of the models. Figures 3.19 and 3.20 show for models M4 and M7 respectively the projections of the sky distributions of the average density of the reconstructed angular momenta obtained with the Bartko et al. (2009) analysis. The x-axes are the ϕ angles, and the y-axes are the values of $\cos\theta$ in these plots. The color peak points to the angular momentum direction of the CW disk, and the black circle shows the position of the observed disk on the plots. We see that
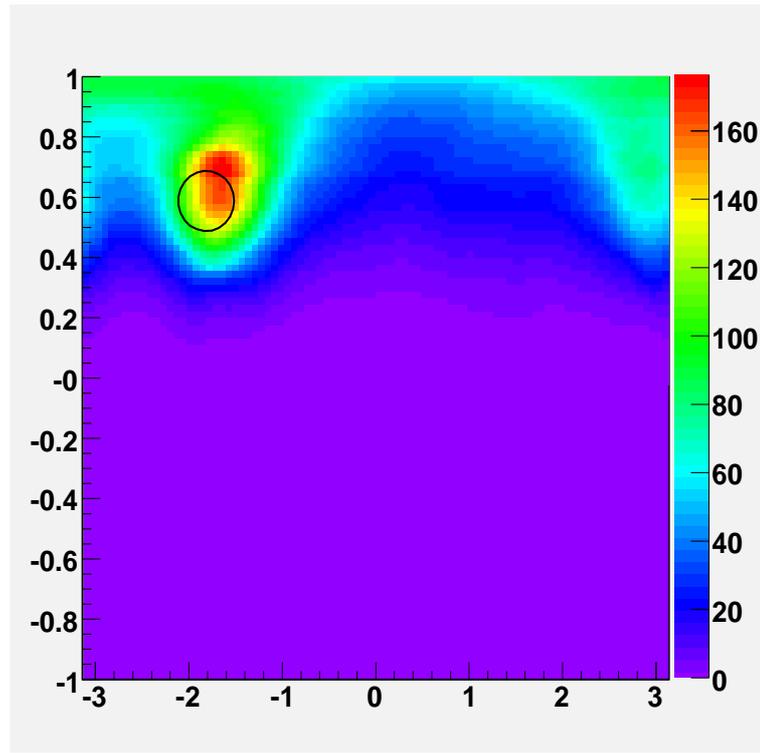
Figure 3.19: Sky map for model M4. Provided by Hendrik Bartko.

model M4 produces a small amplitude warp compared to the data, and model M7 produces a too little twist. Hence we can say that these models are not likely to explain the orbital configuration of the observed disks.

Another useful way of comparing the models is to construct the components of angular
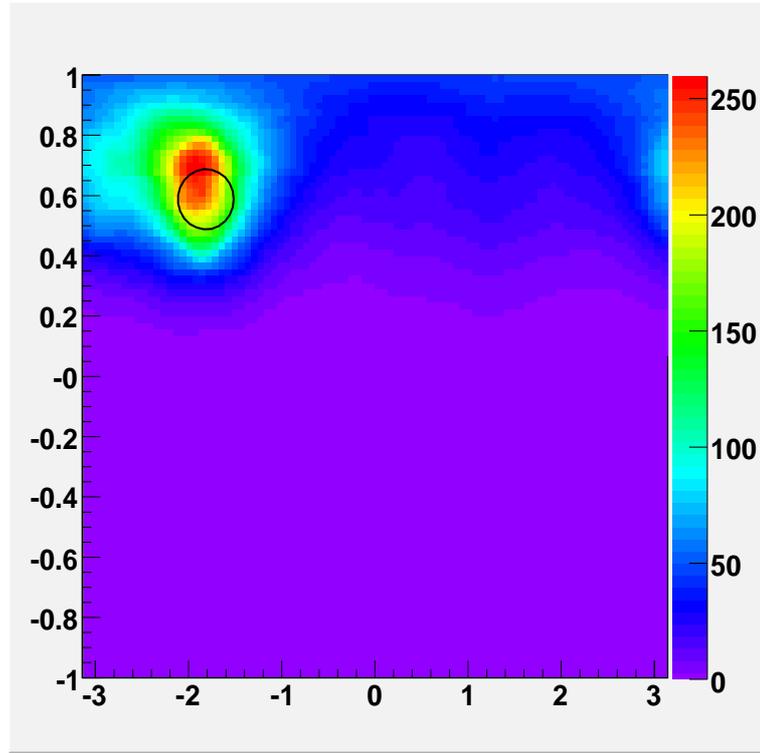
Figure 3.20: Sky map for model M7. Provided by Hendrik Bartko.

momenta and see how they change with projected radius. These are shown in figures 3.21, and 3.22 for models M5, and M6, respectively. The figures on the left correspond to the change of the disk inclination with projected distance from the center, while the figures on the right show the degree of the twist, i.e. varying line-of-nodes. The blue points represent the data, while the red ones represent the models. We see a good agreement between our model M5 and the observations of the CW disk in that the inclination changes gradually between the inner and the outer edges of the disk, and that the amplitude of the warp is successfully produced.

In our simulations we saw that the initially imposed global degree of warping is preserved during the disk evolution. Even if massive disks break into two pieces with large separation angles, the difference in inclination between the innermost and outermost radii remain almost unchanged. The observational analysis presented in Bartko et al. (2009) can discriminate between the broken and unbroken disks as can be seen from the left plots in figures 3.21 and 3.22. Since the radial change of the inclination of the observed disks is a smooth one, we can conclude that the massive, breaking disks can be excluded to be representative of the observations.
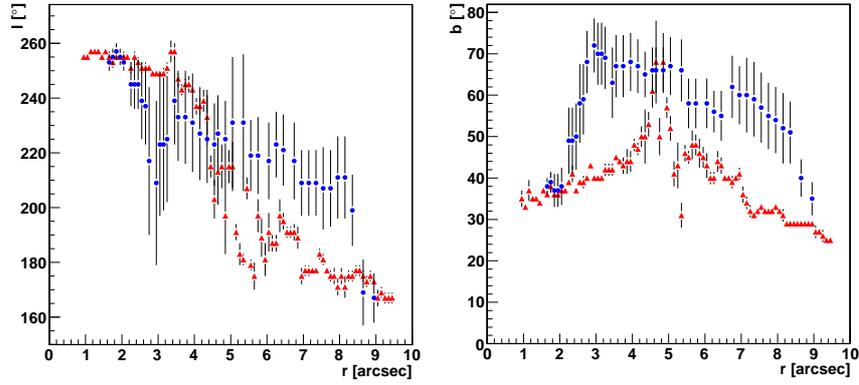
Figure 3.21: Local angular momentum direction for model M5. The x-axis is the average projected distance from the center in arcseconds, and the y-axis is the inclination (left), and the twist (right) of the disk. The figure is provided by Hendrik Bartko.
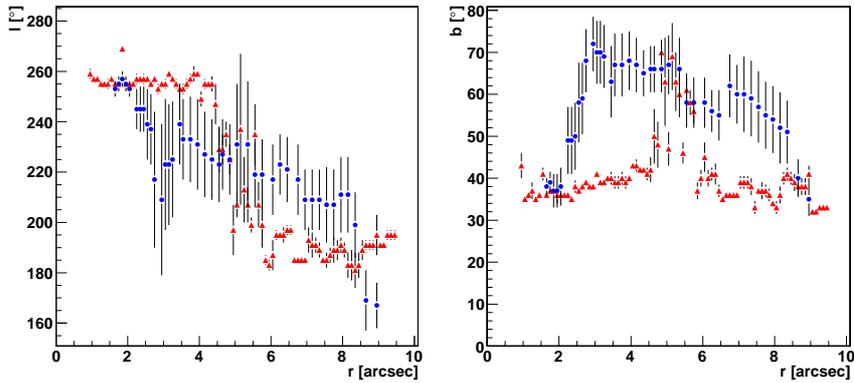

Figure 3.22: Local angular momentum direction for model M6. The x-axis is the average projected distance from the center in arcseconds, and the y-axis is the inclination (left), and the twist (right) of the disk. The figure is provided by Hendrik Bartko.

On the other hand, none of our breaking disk configurations lead to an extra counter-rotating disk when projected onto the plane of the sky. Such a discrete structure would appear at negative $\cos\theta$ values in figures 3.19 and 3.20 [see Figure 10 of Bartko et al. (2009)]. Thus we can can say that the CWW disk observed at the GC probably has a different origin than the CW one.

3.6 Discussion

In this chapter we have proposed a new scenario for the formation of inclined stellar disks at the Galactic Center. We assumed the past existence of an accretion disk around SgA*

and we showed that the disk might have been warped by radiation pressure or by Bardeen Petterson effect. For the parameters making the warping mechanisms plausible, we carried out simulations following the warped stellar disk in time taking into account the effects of the disk self-gravity.

In our simulations, we used a simple circular ring model where we neglected the possible effects of the orbital eccentricities. In a recent publication Madigan et al. (2009) have shown that an initially eccentric disk embedded in a stellar cusp around a massive black hole is subject to an instability with a growth time scale of about a precession time. Neglecting the effects of the disk self-gravity they simulated eccentric disks with parameters relevant to the GC environment. Their results suggest that the instability becomes inefficient for disks which are inclined by more than $\sim 10°$. Still, it is reasonable to expect that if the torques from the disk self-gravity are included in such calculations, the eccentricity evolution of the disk proceeds in a different way, especially for the high disk mass fractions.

To be able to scan a large set of parameters, i.e. $M_d/M_{bh}, \theta_{\text{init}}, \phi_{\text{init}}, \dot{\phi}_{\text{init}}, \epsilon_{\text{SF}}$, we integrated our model disks up to 1000 orbital periods, which is shorter than the age of the system. For the non-breaking disks, we saw that the evolution was slow, and even integrating the system for longer would not lead to a substantial difference where the disk would continue precessing as a single disk. Only in a few cases where we observed a very pronounced breaking up of a disk, we followed the time evolution of the disks longer. Recently, Löckmann & Baumgardt (2009) addressed the issue of interaction of two mutually inclined disks in application to the Galactic Center. Their simulations start with two already split up disks in place, and the gravitational interaction of the two disks are followed for ~ 5 Myr. They find that after ~ 5 Myr the outer disk gets disrupted due to differential precession. Our simulations show that even for very high disk mass fractions of order $0.01 M_{bh}$, the disk would need at least a million year to break into two separate disks. Hence, the simulations considering already in-place two disks should be interpreted at earlier times, otherwise the integration times will exceed the inferred age of the system.

3.7 Conclusions

In this chapter we have proposed a new scenario for the formation of the warped stellar disks of stars at the Galactic Center. Our scenario differs from previous works in that star formation is considered to take place after disk warping. Assuming a radiation warping, or Bardeen-Petterson warping origin, we carried out simulations of self-gravitating warped disks.

We have simulated disks with different surface density profiles, initial inclinations, and azimuthal structure. The initial conditions imposed by different warping mechanisms seem not to play a significant role in our simulations. We should note however that self-consistent modeling of the warping processes and thereafter star formation would be required to justify this result fully. This calls for accounting for the self gravity torques in the standard viscous warped disk evolution equations.

We saw that the evolution of the disk is mainly controlled by the disk mass. We observed that the disks with $M_d/M_{bh} > 0.001$ break into two pieces each of which can be characterized as mildly warped precessing disks. The time scale by which this break up occurs decreases with increasing disk mass. The degree of mutual separation increases linearly with precession time until about 35 precession times, and then it stays constant at around $45°$.

The comparison of the models with the observations of the Galactic Center disks show that the clockwise rotating disk can be explained by a single precessing disk, with a mass fraction of order $0.001 M_{bh}$.

Chapter 4

Summary and Outlook

The increasing power of astronomical observations has provided evidence for the existence of warped disks in the parsec scale vicinity of nuclear black holes. These disks are often traced by maser emission, or for the unique case of the Galactic Center, by individual stellar orbits. Many theories have been suggested as the cause of warps in nuclear disks. Among them, radiation instability (Pringle, 1996), and the Bardeen-Petterson Effect (Bardeen & Petterson, 1975) are the most well studied ones. Other possible warping mechanisms include gravitational interaction of a disk with a companion object (Papaloizou et al., 1998), or with surrounding stars (Bregman & Alexander, 2009).

The above mentioned works either neglect the self-gravity of the disk, or make use of the simplified linearized torques. However, both the observations of the maser nuclei, and the Galactic Center suggest that nuclear disks might be as massive as $\sim 10\%$ of the black hole, and might be highly warped. Therefore, the key aspect of this thesis has been to model nonlinearly warped self-gravitating disks around massive black holes in galactic centers. In the following we will summarize the major outcomes of this PhD study, and will give a brief outlook.

4.1 Summary

4.1.1 Self-Gravitating Nuclear Warped Disks

In Chapter (2) an equilibrium model was developed for steadily precessing purely self-gravitating warped disks around supermassive black holes. The major advance of the model is the consideration of the non-linear self-gravity torques acting on the disk elements.

99

Using the steady state equations of motion, a scaling relation was derived relating the global precession frequency (normalized to a reference rotational frequency) to the disk mass fraction. Hence, a change in distance to the central hole, and/or the disk mass might be compensated to lead to the same equilibrium warp shape when the precession frequency is properly scaled. The relation derived is simple, and can be applied to a variety of systems where the dominant non-Keplerian force is the disk self-gravity. The accuracy of the scaling relation was tested for different combinations of the disk mass, radial extent, and precession frequency, and it was found that the model is accurate to $\sim 1°$.

Equilibrium configurations of low-to-high mass disks were computed assuming various surface density profiles, radial extents, and precession frequencies. It was found that the degree of warping increases with increasing disk mass dramatically when the other parameters are kept unaltered. A striking result emerging from these computations is that for a range of reasonable parameters highly warped equilibrium configurations where the disk obscures the central object completely might be constructed.

In order to make a comparison to the previous studies and to highlight the differences, the linear theory of self-gravitating warped disks has been revisited. The main predictions of the linear theory is reproduced, and used as an initial guess for nonlinear calculations. It is shown that apart from differences in the equilibrium shapes, the main distinction is the allowed range of parameters for equilibria. In linear theory, a disk with a certain mass profile, and radial extent can support only a single $(m, n) = (1, 1)$ mode with a prescribed precession frequency, and a corresponding fixed (but scalable) warp shape. On the other hand in the non-linear regime, the same disk can have varying warp shapes for varying precession frequencies.

Stability of such highly warped steadily precessing disks was studied using perturbation theory, and for a few cases was checked by time integration of the equations of motion. It was found that stable equilibria exist only for a limited range of r_{out}/r_{in} ratios, typically $2 - 4$. For disks with radial extents in this range, the mass fraction for stable equilibria can have values between $\sim 10^{-3} - 10^{-1}$, where the actual limits depend on the details of the model.

4.1.2   The Galactic Center Stellar Disks

In Chapter (3) a new scenario for the formation mutually inclined warped disks was presented. It was assumed that the observed warp in the stellar disk of the Galactic Center was excited by either radiation pressure, or by Bardeen-Petterson Effect before star formation took place. For

each of these warping mechanisms, the relevant radial and time scales have been computed to test their plausibility. It was shown that for the radiation instability to be viable, the past luminosity of the Galactic Center region had be orders of magnitude higher than its current value.

Adopting initial values imposed by these mechanisms, the time evolution of a warped self-gravitating disk of stars was followed. Various models have been compiled which differ from each other in the assumed origin, i.e. initial warp shape, total disk mass and surface density profile. It was found that the time evolution of the disk is very much sensitive to the disk mass, but not to the assumed initial conditions.

An interesting outcome of these calculations is that disks with mass fractions > 0.001 split into two separate disks which precess with their own mean rates, while disks with smaller mass fractions precess without a change in their initially imposed warping angles.

The splitting of the disk just mentioned occurs on a time scale which depends on the disk mass. Since more massive disks precess with faster rates, such disks are the ones which break up at earlier times of their evolution. It is found that the degree of mutual separation between the two disks increases linearly by time until about 35 precessions, and after that it saturates at about $50°$.

A comparison of these models to the observations of the Galactic Center disks was made. It was found that the clockwise rotating disk can be explained by a single precessing disk, with a mass fraction of order $0.001 M_{bh}$.

4.2 Outlook

There are several possible improvements to the self-gravitating warped nuclear disk models discussed in this thesis. In the following I mention some of them, and list some of the possible applications.

4.2.1 Theoretical Improvements

- *Self-Gravitating Viscous Warped Disks*

  The study of warps in the nuclear disks often makes use of the standard accretion disk formalism as briefly discussed in the introduction of this thesis. This comes about because the warps are believed to be excited as a result of a competition between the vertical viscosity in the disk, and the outward net forcing due to an external source.

The viscous evolution of the disk is mostly studied based on the local conservation equations as put in a suitable form by Pringle (1992). In this scheme various warping mechanisms are accounted for by inserting the relevant torques to the momentum conservation equation. Addition of the self-gravity torques to the momentum equation would be a very natural extension of the pure self-gravity model presented here. Preliminary calculations where the solution of the continuity equation is obtained for viscous self-gravitating warped disks suggest that many interesting outcomes can be expected with this improvement.

- *Self-consistent Modeling of Warping Mechanisms and Star Formation*

In chapter (3) studying the time evolution of the warped stellar disk at the Galactic Center, approximate initial conditions were adopted making use of the existing results in the literature. In doing so, it was assumed that self-gravity provides the dominant torques. It would be interesting to extend the models such that ceasing of the radiation torques is computed in a self-consistent way. This would require the viscous evolution equations to be implemented in the time integration scheme. When done so, the interplay between warping and star formation in galaxy centers can be studied in a more reliable manner.

4.2.2   Possible Applications

- *Interaction of the Galactic Center Disk with the Circumnuclar Disk (CND)*

In a recent publication, Subr et al. (2008) have proposed the interaction of the Galactic Center stellar disks with the surrounding CND as the cause of the observed orbital distribution of stars. While the CND and the stellar disks have comparable, and non-negligible mass, self-gravity of the disks were neglected. A very straightforward application of the models presented in chapter (3) could be to implement a massive disk inclined to the stellar disk and account for the effects of the CND.

- *Application To Maser Nuclei - The Case of Circinus*

One of the best examples of a warped nuclear disk lies in the center of Circinus Galaxy (Greenhill et al., 2003). The maser activity observed in the disk constrains the mass, i.e. surface density, of the disk to assume a large value with an upper limit of $\sim 0.2 M_{bh}$. The degree of warping in the disk reaches to about $\sim 30°$. With these parameters,

Circinus maser disk would be a good candidate to apply our self-gravitating nonlinear warp model.

APPENDIX A

COMPONENTS OF ANGULAR MOMENTUM FOR RING i

In this section we give the derivation for the components of angular momentum for ring i in the (x, y, z) axes (equations (2.15), (2.16), and (2.17)). The components of angular momentum, l, in the space axis are written via the transformation (Goldstein et al., 2002):

$$l = AI\omega'. \tag{A.1}$$

Here I is the inertia tensor written as:

$$I = \begin{bmatrix} mr^2/2 & 0 & 0 \\ 0 & mr^2/2 & 0 \\ 0 & 0 & mr^2 \end{bmatrix} \tag{A.2}$$

A is a (3×3) transformation matrix with elements:

$$
\begin{aligned}
a_{11} &= \cos\psi\cos\phi - \cos\theta\sin\phi\sin\psi, \\
a_{12} &= -\sin\psi\cos\phi - \cos\theta\sin\phi\cos\psi, \\
a_{13} &= \sin\theta\sin\phi, \\
a_{21} &= \cos\psi\sin\phi + \cos\theta\cos\phi\sin\psi, \\
a_{22} &= -\sin\psi\sin\phi + \cos\theta\cos\phi\cos\psi, \\
a_{23} &= -\sin\theta\cos\phi,
\end{aligned}
$$

$$
\begin{aligned}
a_{31} &= \sin\psi\sin\theta, \\
a_{32} &= \cos\psi\sin\theta, \\
a_{33} &= \cos\theta
\end{aligned}
\tag{A.3}
$$

and ω' is the angular velocity with respect to body axis, and are written as:

$$
\begin{aligned}
\omega'_x &= \dot{\phi}\sin\theta\sin\psi + \dot{\theta}\cos\psi \tag{A.4} \\
\omega'_y &= \dot{\phi}\sin\theta\cos\psi - \dot{\theta}\sin\psi \tag{A.5} \\
\omega'_z &= \dot{\phi}\cos\theta + \dot{\psi} \tag{A.6}
\end{aligned}
$$

Combining these, the components of the angular momentum for a single ring are obtained as:

$$
l_x = p_\theta\cos\phi + \frac{\sin\phi(p_\psi - p_\phi\cos\theta)}{\sin\theta},
\tag{A.7}
$$

$$
l_y = p_\theta\sin\phi - \frac{\cos\phi(p_\psi - p_\phi\cos\theta)}{\sin\theta},
\tag{A.8}
$$

$$
l_z = p_\phi.
\tag{A.9}
$$

Appendix B

Elements of the Stability Matrix

In section (2.2.7), stability of steadily precessing equilibria was studied using perturbation theory. The explicit forms of the kinetic terms entering the stability matrix are written as:

$$\frac{\partial^2 T_i}{\partial p_{\theta_i}^2} = \frac{2}{m_i r_i^2} \tag{B.1}$$

$$\frac{\partial^2 T_i}{\partial \theta_i \partial p_{\phi_i}} = \frac{2(p_{\phi_i} - \cos\theta_i p_{\psi_i})}{(m_i r_i^2 \sin\theta_i^2)} \tag{B.2}$$

$$\frac{\partial^2 T_i}{\partial p_{\phi_i}^2} = \frac{2}{m_i r_i^2 \sin^2\theta_i} \tag{B.3}$$

$$\frac{\partial^2 T_i}{\partial \theta_i^2} = \frac{2(p_{\phi_i} - p_{\psi_i}\cos\theta_i)(p_{\psi_i}\cos^3\theta_i + 2p_{\phi_i}\cos^2\theta_i - 4p_{\psi_i}\cos\theta_i + p_{\phi_i})}{m_i r_i^2 \sin^4\theta_i} \tag{B.4}$$

APPENDIX C

CALCULATION OF THE RADIATION TORQUE

In Chapter 3, the radiation torque acting on the supposed Galactic Center gaseous disk was compared to the gravitational torque. Here, we give a more detailed calculation of the radiation torque.

The torque on a ring due to radiation pressure is written as $\tau_r = 2\pi \mathbf{T_\Gamma} r dr$, where $\mathbf{T_\Gamma}$ is the radiation torque density given by Ogilvie & Dubus (2001):

$$\mathbf{T_\Gamma} = -\frac{L}{12\pi c} f(|\psi|) \mathbf{l} \times \frac{\partial \mathbf{l}}{\partial r}, \tag{C.1}$$

where, $f(|\psi|)$ is a term which limits the effectiveness of the radiation torque for highly inclined warps, and it has the Taylor series:

$$f(x) = 1 - \frac{3}{8}x^2 + \frac{15}{64}x^4 - \frac{175}{1024}x^6 + O(x^8). \tag{C.2}$$

$\mathbf{l}$ is the unit vector and in our notation written as:

$$l_x = \sin\theta \sin\phi, \ \ l_y = -\sin\theta \cos\phi \ \ l_z = \cos\theta. \tag{C.3}$$

The radial derivatives of the unit vector l then have the components:

$$\frac{\partial l_x}{\partial r} = \cos\theta\sin\phi\frac{\partial\theta}{\partial r} + \sin\theta\cos\phi\frac{\partial\phi}{\partial r} \tag{C.4}$$

$$\frac{\partial l_y}{\partial r} = -\cos\theta\cos\phi\frac{\partial\theta}{\partial\theta} + \sin\theta\sin\phi\frac{\partial\phi}{\partial r} \tag{C.5}$$

$$\frac{\partial l_z}{\partial r} = -\sin\theta\frac{\partial\theta}{\partial r}. \tag{C.6}$$

In this case:

$$\mathbf{l} \times \frac{\partial\mathbf{l}}{\partial r} = \left[\cos\phi\frac{\partial\theta}{\partial r} - \cos\theta\sin\theta\sin\phi\frac{\partial\phi}{\partial r}\right]\hat{e}_x + \tag{C.7}$$

$$\left[\cos\theta\sin\theta\cos\phi\frac{\partial\phi}{\partial r} + \sin\phi\frac{\partial\theta}{\partial r}\right]\hat{e}_y +$$

$$\left[\sin^2\theta\frac{\partial\phi}{\partial r}\right]\hat{e}_z,$$

and its magnitude to be cast into equation (C.1) is:

$$\left|\mathbf{l} \times \frac{\partial\mathbf{l}}{\partial r}\right| = \sqrt{\left(\frac{\partial\phi}{\partial r}\right)^2\sin^2\theta + \left(\frac{\partial\theta}{\partial r}\right)^2}. \tag{C.8}$$

APPENDIX D

CONSTANTS

Physical Constant

Gravitational constant	$G = 6.67 \times 10^{-8}$ cm^3 s^{-2} g^{-1}
Thomson cross section	$\sigma_T = (8\pi/3)(e^2/m_e c^2)^2$ (cm^2)
Speed of light	$c = 2.98 \times 10^{10}$ cm s^{-1}
Proton mass	$m_p = 1.673 \times 10^{-24}$ g

Astrophysical Unit

Astronomical unit	$AU = 1.496 \times 10^{13}$ cm
Parsec	$pc = 3.09 \times 10^{18}$ cm
Solar mass	$M_\odot = 1.99 \times 10^{33}$ g
Solar radius	$R_\odot = 6.96 \times 10^{10}$ cm

APPENDIX E

ABBREVIATIONS AND SYMBOLS

Abbrevation	Meaning
AGN	Active Galactic Nucleus
BLR	Broad Line Region
CCW	Counter clockwise
CW	Clockwise
GC	Galactic Center
LONs	Line of Nodes
LOS	Line of Sight
NGC	New General Catalogue
SMBH	Supermassive Black Hole

Symbol	
L_{Edd}	Eddington Luminosity
$M_\odot$	Solar mass
$R_\odot$	Solar radius
pc	parsec

BIBLIOGRAPHY

Alexander, R. D., Armitage, P. J., Cuadra, J., & Begelman, M. C. 2008, ApJ, 674, 927

Alexander, T. 2006, Journal of Physics Conference Series, 54, 243

Antonucci, R. R. J. & Miller, J. S. 1985, ApJ, 297, 621

Armitage, P. J. & Natarajan, P. 1999, ApJ, 525, 909

Arnaboldi, M. & Sparke, L. S. 1994, AJ, 107, 958

Baganoff, F. K., Maeda, Y., Morris, M., Bautz, M. W., Brandt, W. N., Cui, W., Doty, J. P., Feigelson, E. D., Garmire, G. P., Pravdo, S. H., Ricker, G. R., & Townsley, L. K. 2003, ApJ, 591, 891

Balbus, S. A. & Hawley, J. F. 1991, ApJ, 376, 214

Balick, B. & Brown, R. L. 1974, ApJ, 194, 265

Bardeen, J. M. & Petterson, J. A. 1975, ApJ, 195, L65+

Bartko, H., Martins, F., Fritz, T. K., Genzel, R., Levin, Y., Perets, H. B., Paumard, T., Nayakshin, S., Gerhard, O., Alexander, T., Dodds-Eden, K., Eisenhauer, F., Gillessen, S., Mascetti, L., Ott, T., Perrin, G., Pfuhl, O., Reid, M. J., Rouan, D., Sternberg, A., & Trippe, S. 2009, ApJ, 697, 1741

Becklin, E. E., Gatley, I., & Werner, M. W. 1982, ApJ, 258, 135

Binney, J., Jiang, I.-G., & Dutta, S. 1998, MNRAS, 297, 1237

Binney, J. & Tremaine, S. 1987, Galactic dynamics (Princeton, NJ, Princeton University Press, 1987, 747 p.)

115

Böker, T., Falcón-Barroso, J., Schinnerer, E., Knapen, J. H., & Ryder, S. 2008, AJ, 135, 479

Bonnell, I. A. & Rice, W. K. M. 2008, Science, 321, 1060

Borderies, N., Goldreich, P., & Tremaine, S. 1983, AJ, 88, 226

Bregman, M. & Alexander, T. 2009, ArXiv e-prints

Caproni, A., Abraham, Z., Livio, M., & Mosquera Cuesta, H. J. 2007, MNRAS, 379, 135

Caproni, A., Abraham, Z., & Mosquera Cuesta, H. J. 2006a, ApJ, 638, 120

Caproni, A., Livio, M., Abraham, Z., & Mosquera Cuesta, H. J. 2006b, ApJ, 653, 112

Carollo, C. M., Stiavelli, M., & Mack, J. 1998, AJ, 116, 68

Claussen, M. J., Heiligman, G. M., & Lo, K. Y. 1984, Nature, 310, 298

Coil, A. L. & Ho, P. T. P. 1999, ApJ, 513, 752

—. 2000, ApJ, 533, 245

Coker, R. F., Christopher, M. H., Stolovy, S. R., & Scoville, N. Z. 2003, Astronomische Nachrichten Supplement, 324, 629

Cuadra, J., Armitage, P. J., & Alexander, R. D. 2008, ArXiv e-prints, 804

Eckart, A. & Genzel, R. 1996, Nature, 383, 415

Eisenhauer, F., Genzel, R., Alexander, T., Abuter, R., Paumard, T., Ott, T., Gilbert, A., Gillessen, S., Horrobin, M., Trippe, S., Bonnet, H., Dumas, C., Hubin, N., Kaufer, A., Kissler-Patig, M., Monnet, G., Ströbele, S., Szeifert, T., Eckart, A., Schödel, R., & Zucker, S. 2005, ApJ, 628, 246

Eisenhauer, F., Schödel, R., Genzel, R., Ott, T., Tecza, M., Abuter, R., Eckart, A., & Alexander, T. 2003, ApJ, 597, L121

Ferrarese, L. & Ford, H. 2005, Space Science Reviews, 116, 523

Ferrarese, L. & Merritt, D. 2000, ApJ, 539, L9

Frank, J., King, A., & Raine, D. J. 2002, Accretion Power in Astrophysics: Third Edition (Accretion Power in Astrophysics, by Juhan Frank and Andrew King and Derek Raine, pp. 398. ISBN 0521620538. Cambridge, UK: Cambridge University Press, February 2002.)

Fujii, M., Iwasawa, M., Funato, Y., & Makino, J. 2007, ArXiv e-prints, 708

Gallimore, J. F., Baum, S. A., & O'Dea, C. P. 2004, ApJ, 613, 794

Gammie, C. F. 2001, ApJ, 553, 174

Gardner, F. F. & Whiteoak, J. B. 1982, MNRAS, 201, 13P

Gatley, I., Jones, T. J., Hyland, A. R., Wade, R., Geballe, T. R., & Krisciunas, K. 1986, MNRAS, 222, 299

Gebhardt, K., Bender, R., Bower, G., Dressler, A., Faber, S. M., Filippenko, A. V., Green, R., Grillmair, C., Ho, L. C., Kormendy, J., Lauer, T. R., Magorrian, J., Pinkney, J., Richstone, D., & Tremaine, S. 2000, ApJ, 539, L13

Genzel, R., Crawford, M. K., Townes, C. H., & Watson, D. M. 1985, ApJ, 297, 766

Genzel, R., Pichon, C., Eckart, A., Gerhard, O. E., & Ott, T. 2000, MNRAS, 317, 348

Genzel, R., Schödel, R., Ott, T., Eisenhauer, F., Hofmann, R., Lehnert, M., Eckart, A., Alexander, T., Sternberg, A., Lenzen, R., Clénet, Y., Lacombe, F., Rouan, D., Renzini, A., & Tacconi-Garman, L. E. 2003, ApJ, 594, 812

Gerend, D. & Boynton, P. E. 1976, ApJ, 209, 562

Gerhard, O. 2001, ApJ, 546, L39

Ghez, A. M., Duchêne, G., Matthews, K., Hornstein, S. D., Tanner, A., Larkin, J., Morris, M., Becklin, E. E., Salim, S., Kremenek, T., Thompson, D., Soifer, B. T., Neugebauer, G., & McLean, I. 2003, ApJ, 586, L127

Ghez, A. M., Salim, S., Hornstein, S. D., Tanner, A., Lu, J. R., Morris, M., Becklin, E. E., & Duchêne, G. 2005, ApJ, 620, 744

Giacconi, R., Gursky, H., Kellogg, E., Levinson, R., Schreier, E., & Tananbaum, H. 1973, ApJ, 184, 227

Gillessen, S., Eisenhauer, F., Trippe, S., Alexander, T., Genzel, R., Martins, F., & Ott, T. 2009, ApJ, 692, 1075

Goldreich, P. 1966, Reviews of Geophysics, 4, 411

Goldreich, P. & Tremaine, S. 1979, AJ, 84, 1638

Goldstein, H., Poole, C., & Safko, J. 2002, Classical mechanics (Classical mechanics (3rd ed.) by H. Goldstein, C. Poolo, and J. Safko. San Francisco: Addison-Wesley, 2002.)

Goodman, J. 2003, MNRAS, 339, 937

Greenhill, L. J., Booth, R. S., Ellingsen, S. P., Herrnstein, J. R., Jauncey, D. L., McCulloch, P. M., Moran, J. M., Norris, R. P., Reynolds, J. E., & Tzioumis, A. K. 2003, ApJ, 590, 162

Greenhill, L. J. & Gwinn, C. R. 1997, Astrophysics and Space Science, 248, 261

Guesten, R., Genzel, R., Wright, M. C. H., Jaffe, D. T., Stutzki, J., & Harris, A. I. 1987, ApJ, 318, 124

Gürkan, M. A. & Hopman, C. 2007, MNRAS, 379, 1083

Gürkan, M. A. & Rasio, F. A. 2005, ApJ, 628, 236

Hansen, B. M. S. & Milosavljević, M. 2003, ApJ, 593, L77

Herrnstein, J. R., Greenhill, L. J., & Moran, J. M. 1996, ApJ, 468, L17+

Herrnstein, J. R., Moran, J. M., Greenhill, L. J., Diamond, P. J., Inoue, M., Nakai, N., Miyoshi, M., Henkel, C., & Riess, A. 1999, Nature, 400, 539

Herrnstein, J. R., Moran, J. M., Greenhill, L. J., & Trotter, A. S. 2005, ApJ, 629, 719

Hicks, E. K. S., Davies, R. I., Malkan, M. A., Genzel, R., Tacconi, L. J., Sánchez, F. M., & Sternberg, A. 2009, ApJ, 696, 448

Hobbs, A. & Nayakshin, S. 2009, MNRAS, 394, 191

Hofner, P. & Sparke, L. S. 1994, ApJ, 428, 466

Hopman, C. & Alexander, T. 2006, Journal of Physics Conference Series, 54, 321

Hunter, C. & Toomre, A. 1969, ApJ, 155, 747

Innanen, K. A., Kamper, K. W., van den Bergh, S., & Papp, K. A. 1982, ApJ, 254, 515

Jackson, J. M., Geis, N., Genzel, R., Harris, A. I., Madden, S., Poglitsch, A., Stacey, G. J., & Townes, C. H. 1993, ApJ, 402, 173

Jiang, I.-G. & Binney, J. 1999, MNRAS, 303, L7

King, A. R., Lubow, S. H., Ogilvie, G. I., & Pringle, J. E. 2005, MNRAS, 363, 49

Kolykhalov, P. I. & Syunyaev, R. A. 1980, Soviet Astronomy Letters, 6, 357

Kondratko, P. T. 2007, PhD thesis, Harvard University

Kormendy, J. & Richstone, D. 1995, ARA&A, 33, 581

Krabbe, A., Genzel, R., Eckart, A., Najarro, F., Lutz, D., Cameron, M., Kroker, H., Tacconi-Garman, L. E., Thatte, N., Weitzel, L., Drapatz, S., Geballe, T., Sternberg, A., & Kudritzki, R. 1995, ApJ, 447, L95+

Kuijken, K. 1991, ApJ, 376, 467

Kumar, S. & Pringle, J. E. 1985, MNRAS, 213, 435

Lai, D. 1999, ApJ, 524, 1030

—. 2003, ApJ, 591, L119

Lense, J. & Thirring, H. 1918, Physikalische Zeitschrift, 19, 156

Levin, Y. & Beloborodov, A. M. 2003, ApJ, 590, L33

Lo, K. Y. & Claussen, M. J. 1983, Nature, 306, 647

Löckmann, U. & Baumgardt, H. 2009, MNRAS, 276

Lodato, G. 2008, New Astronomy Review, 52, 21

Lodato, G. & Pringle, J. E. 2006, MNRAS, 368, 1196

—. 2007, MNRAS, 381, 1287

Lodato, G. & Rice, W. K. M. 2004, MNRAS, 351, 630

—. 2005, MNRAS, 358, 1489

Lu, J. R., Ghez, A. M., Hornstein, S. D., Morris, M., Matthews, K., Thompson, D. J., & Becklin, E. E. 2006, Journal of Physics Conference Series, 54, 279

Lu, J. R., Ghez, A. M., Hornstein, S. D., Morris, M. R., Becklin, E. E., & Matthews, K. 2009, ApJ, 690, 1463

Lynden-Bell, D. & Pringle, J. E. 1974, MNRAS, 168, 603

Madigan, A.-M., Levin, Y., & Hopman, C. 2009, ApJ, 697, L44

Magorrian, J., Tremaine, S., Richstone, D., Bender, R., Bower, G., Dressler, A., Faber, S. M., Gebhardt, K., Green, R., Grillmair, C., Kormendy, J., & Lauer, T. 1998, AJ, 115, 2285

Maloney, P. R., Begelman, M. C., & Pringle, J. E. 1996, ApJ, 472, 582

Mapelli, M., Hayfield, T., Mayer, L., & Wadsley, J. 2008, ArXiv e-prints, 805

Martin, R. G. 2008, MNRAS, 387, 830

Martins, F., Gillessen, S., Eisenhauer, F., Genzel, R., Ott, T., & Trippe, S. 2008, ApJ, 672, L119

McGary, R. S., Coil, A. L., & Ho, P. T. P. 2001, ApJ, 559, 326

Merritt, D. 2006, Reports of Progress in Physics, 69, 2513

Milosavljević, M. & Loeb, A. 2004, ApJ, 604, L45

Miyoshi, M., Moran, J., Herrnstein, J., Greenhill, L., Nakai, N., Diamond, P., & Inoue, M. 1995, Nature, 373, 127

Morris, M. 1993, ApJ, 408, 496

Narayan, R. 2002, in Lighthouses of the Universe: The Most Luminous Celestial Objects and Their Use for Cosmology, ed. M. Gilfanov, R. Sunyeav, & E. Churazov, 405–+

Natarajan, P. & Armitage, P. J. 1999, MNRAS, 309, 961

Nayakshin, S. 2005, MNRAS, 359, 545

Nayakshin, S. & Cuadra, J. 2005, A&A, 437, 437

Nayakshin, S., Cuadra, J., & Springel, V. 2007, MNRAS, 379, 21

Nayakshin, S., Dehnen, W., Cuadra, J., & Genzel, R. 2006, MNRAS, 366, 1410

Nelson, R. W. & Tremaine, S. 1995, MNRAS, 275, 897

Nenkova, M., Ivezić, Ž., & Elitzur, M. 2002, ApJ, 570, L9

Ogilvie, G. I. 1999, MNRAS, 304, 557

Ogilvie, G. I. & Dubus, G. 2001, MNRAS, 320, 485

Papaloizou, J. C. B. & Lin, D. N. C. 1995, ARA&A, 33, 505

Papaloizou, J. C. B. & Pringle, J. E. 1983, MNRAS, 202, 1181

Papaloizou, J. C. B., Terquem, C., & Lin, D. N. C. 1998, ApJ, 497, 212

Paumard, T., Genzel, R., Martins, F., Nayakshin, S., Beloborodov, A. M., Levin, Y., Trippe, S., Eisenhauer, F., Ott, T., Gillessen, S., Abuter, R., Cuadra, J., Alexander, T., & Sternberg, A. 2006, ApJ, 643, 1011

Petterson, J. A. 1977, ApJ, 216, 827

Pfeiffer, H. P. & Lai, D. 2004, ApJ, 604, 766

Phinney, E. S. 1989, in NATO ASIC Proc. 290: Theory of Accretion Disks, ed. F. Meyer, 457–+

Pringle, J. E. 1981, ARA&A, 19, 137

—. 1992, MNRAS, 258, 811

—. 1996, MNRAS, 281, 357

—. 1997, MNRAS, 292, 136

Rauch, K. P. & Tremaine, S. 1996, New Astronomy, 1, 149

Reshetnikov, V., Battaner, E., Combes, F., & Jiménez-Vicente, J. 2002, A&A, 382, 513

Sanders, R. H. 1998, MNRAS, 294, 35

Schandl, S. & Meyer, F. 1994, A&A, 289, 149

Scheuer, P. A. G. & Feiler, R. 1996, MNRAS, 282, 291

Schinnerer, E., Böker, T., Emsellem, E., & Lisenfeld, U. 2006, ApJ, 649, 181

Schödel, R., Eckart, A., Alexander, T., Merritt, D., Genzel, R., Sternberg, A., Meyer, L., Kul, F., Moultaka, J., Ott, T., & Straubmeier, C. 2007, A&A, 469, 125

Schödel, R., Ott, T., Genzel, R., Hofmann, R., Lehnert, M., Eckart, A., Mouawad, N., Alexander, T., Reid, M. J., Lenzen, R., Hartung, M., Lacombe, F., Rouan, D., Gendron, E., Rousset, G., Lagrange, A.-M., Brandner, W., Ageorges, N., Lidman, C., Moorwood, A. F. M., Spyromilio, J., Hubin, N., & Menten, K. M. 2002, Nature, 419, 694

Shafee, R., Narayan, R., & McClintock, J. E. 2008, ApJ, 676, 549

Shakura, N. I. & Syunyaev, R. A. 1973, A&A, 24, 337

Sparke, L. S. 1984, ApJ, 280, 117

—. 1986, MNRAS, 219, 657

Sparke, L. S. & Casertano, S. 1988, MNRAS, 234, 873

Subr, L., Schovancova, J., & Kroupa, P. 2008, ArXiv e-prints

Tadhunter, C. 2007, lecture Notes

Tananbaum, H., Gursky, H., Kellogg, E. M., Levinson, R., Schreier, E., & Giacconi, R. 1972, ApJ, 174, L143+

Tisseur, F. & Meerbergen, K. 2001, SIAM Rev., 43, 235

Toomre, A. 1983, in IAU Symposium, Vol. 100, Internal Kinematics and Dynamics of Galaxies, ed. E. Athanassoula, 177–185

Torkelsson, U., Ogilvie, G. I., Brandenburg, A., Pringle, J. E., Nordlund, Å., & Stein, R. F. 2000, MNRAS, 318, 47

Touma, J. R. 2002, MNRAS, 333, 583

Tremaine, S., Gebhardt, K., Bender, R., Bower, G., Dressler, A., Faber, S. M., Filippenko, A. V., Green, R., Grillmair, C., Ho, L. C., Kormendy, J., Lauer, T. R., Magorrian, J., Pinkney, J., & Richstone, D. 2002, ApJ, 574, 740

Trippe, S., Gillessen, S., Gerhard, O. E., Martins, F., Eisenhauer, F., Ott, T., Maness, H. L., Dodds-Eden, K., & Genzel, R. 2008, submitted to A&A

van der Kruit, P. C. 1979, A&AS, 38, 15

Vollmer, B. & Duschl, W. J. 2000, New Astronomy, 4, 581

—. 2001a, A&A, 367, 72

—. 2001b, A&A, 377, 1016

—. 2002, A&A, 388, 128

Wardle, M. & Yusef-Zadeh, F. 2008, ArXiv e-prints, 805

Wijers, R. A. M. J. & Pringle, J. E. 1999, MNRAS, 308, 207

WMCP. 2009, Water Maser Cosmology Project, Website, available online at http://www.cfa.harvard.edu/wmcp/data/data.html

Wu, S.-M., Wang, T.-G., & Dong, X.-B. 2008, ArXiv e-prints, 807

Zier, C. & Biermann, P. L. 2002, A&A, 396, 91

List of Figures

List of Tables

ACKNOWLEDGEMENTS

Foremost, I thank my supervisor Prof. Dr. Ortwin Gerhard for letting me work on this interesting project. Without his assistance and motivation I would not be able to reach to this page of the thesis.

Dr. Magda Arnaboldi provided her code which made this PhD study possible. She has been very motivating and positive which helped me many times . I would like to thank to her for all her support.

I would like to thank Prof. Dr. Reinhard Genzel for accepting to be my co-supervisor, and also for his kind effort in preparing the final report in a limited time.

I thank Dr. Hendrik Bartko for his kind collaboration on the GC project. The figures comparing our models to the observations of the MPE GC group are prepared by him using his technique.

Dr. Jens Thomas wrote the German abstract of the thesis. I thank him for taking the time.

The Basel period of this PhD wouldn't be as easy without the friendships of Caroline Girard, Güliz Çakmak, Hasan Çakmak and Nuri Solak. Thank you all! I hope our ways will cross somewhere again.

The members of the "Doesn't Matter" are all acknowledged for the tuned Tuesdays. Flavio De Lorenzi, Lodovico Coccato and Stefano Mineo turned my upset face to a smile many times. I thank them all.

Aybüke Küpçü Yoldaş and Abdullah Yoldaş have been more than friends to me during the years I spent in Garching. I will miss a lot our 'save the world' discussions. Thank you both for everything, also for carefully reading my thesis.

Beni senelerce okutan, büyüten anneciğime, babacığıma, ve İstanbul'a her gidişimi ayrı bir eğlenceye çeviren Pınışıma, Gökhan enteme ve Çağan yavruya teşekkürler.

Finally I thank my "biricik" for all his support during all my studies. No words can describe it well, but without his encouragement I would not succeed.

Cirrucilum Vitae

Name: Ayşe ULUBAY-SIDDIKİ

Personal Details:

Date of Birth: 21.06.1977

Place of Birth: İstanbul, Turkey

Citizenship: Turkish

Gender: Female

Marital Status: Married

Education

Max Planck Institute for Extraterrestrial Physics, Garching, Germany,

Ph.D. Candidate, Astronomy, (expected graduation date: Summer 2009)

- Dissertation Topic: "Self-Gravitating Warped Disks Around Supermassive Black Holes in Galactic Nuclei"

- Supervisor: Prof. Dr. Ortwin Gerhard

University of Basel, Astronomical Institute, Basel Switzerland,

Ph.D. Candidate, Astronomy, January 2004-December 2005

- Dissertation Topic: "Self-Gravitating Warped Disks Around Supermassive Black Holes in Galactic Nuclei"

- Supervisor: Prof. Dr. Ortwin Gerhard

University of Stuttgart, Department of Mathematics and Physics, Stuttgart, Germany,

M.Sc., Physics, January 2004

- Master of Science Thesis: "Monte Carlo Simulations for the Radiative Transfer in the Magnetospheres of Strongly Magnetized Compact Cosmic X-and Gamma-Ray Sources"

- Supervisor: Prof. Dr. Günter Wunner

Ege University, Department of Astronomy and Space Sciences, Izmir, Turkey
B.Sc., Astronomy, November 1999

- B.Sc. Thesis: "Inner Structure of Neutron Stars and Neutron Star Models"

- Supervisor: Prof. Dr. Mutlu Yıldız

Atafen Science High school, 1992-1995, Kocaeli, Turkey
Kocaeli College, 1988-1992
Nuh Çimento Elementary School, 1983-1988, Hereke/Kocaeli, Turkey

Publications:
Refereed Publications

- 'Self-Gravitating Warped Disks Aroud Supermassive Black Holes', MNRAS, in press

- 'Self-Gravitating Warped Disks Around Black Holes', PoS(MQW7)084

- 'On the Origin of Warped Stellar Disks at the Galactic Center', MNRAS, in preperation

Proceedings

- "Gökada Merkezindeki Yıldız Diskleri İcin Eğrilikli Disk Orijin Senaryosu - Warped Disk Origin for the Inclined Stellar Disks at the Galactic Center", Proceedings of the XV. National Astronomy Meeting of Turkey - Volume 1, 21-29 (2008)

- "Self-Gravitating Warped Disks Aroud Nuclear Black Holes", IAU Proceedings - 2007 IAUS, 238, 467U

- "Süper Kütleli Karadelikler Etrafinda Eğrilikli Diskler - Warped Disks Around Supermassive Black Holes", Proceedings of the XV. National Astronomy Meeting of Turkey - Volume 2, 699-708 (2007)